Master's thesis

NTNU
Norwegian University of Science and Technology
Faculty of Information Technology and Electrical Engineering
Department of Engineering Cybernetics

Johan Fredrik Skaali Frich

A Nonlinear Model Predictive Controller for flexible satellite attitude control

Master's thesis in Cybernetics and Robotics
Supervisor: Prof. Sebastien Gros, NTNU
Co-supervisor: Jesús Ramírez, SENER Aeroespacial
June 2023

NTNU
Norwegian University of
Science and Technology

Johan Fredrik Skaali Frich

A Nonlinear Model Predictive Controller for flexible satellite attitude control

Master's thesis in Cybernetics and Robotics
Supervisor: Prof. Sebastien Gros, NTNU
Co-supervisor: Jesús Ramírez, SENER Aeroespacial
June 2023

Norwegian University of Science and Technology
Faculty of Information Technology and Electrical Engineering
Department of Engineering Cybernetics

NTNU
Norwegian University of
Science and Technology

Contents

Figures

Tables

Acronyms

AMM Assumed Modes Method.

CMG Control Moment Gyroscope.

ECSS European Cooperation for Space Standardization.

EKF Extended Kalman Filter.

EKF1 Extended Kalman Filter 1, Table 5.5.

EKF2 Extended Kalman Filter 2, Table 5.6.

EKF3 Extended Kalman Filter 3, Table 5.6.

EO Earth Observation.

FEM Finite Element Method.

IP Interior Point.

IPOPT Interior Point Optimizer.

KKT Karush–Kuhn–Tucker.

LEO Low Earth Orbit.

LOS Line-Of-Sight.

LQ Linear-Quadratic.

MC Monte Carlo.

MPC Model Predictive Control.

MSE Mean Squared Error.

NLP Nonlinear Program.

NMPC Nonlinear Model Predictive Control.

NMPC1 Nonlinear Model Predictive Controller 1, Eq. (4.11).

NMPC2 Nonlinear Model Predictive Controller 2, Eq. (4.14).

NMPC3 Nonlinear Model Predictive Controller 3, Eq. (4.15).

NMPC4 Nonlinear Model Predictive Controller 4, Eq. (4.18).

OCP Optimal Control Problem.

ODE Ordinary Differential Equation.

PD Proportional-Derivative.

PDE Partial Differential Equation.

PM1 Prediction Model 1, Eq. (4.3).

PM2 Prediction Model 2, Eq. (4.5).

PM3 Prediction Model 3, Eq. (4.6).

PSD Power Spectral Density.

PWM Pulse Width Modulator.

RK Runge-Kutta.

RW Reaction Wheel.

SMC Sliding Mode Control.

SQP Sequential Quadratic Programming.

Abstract

Improved agility for Earth Observation satellites reduces the time spent on maneuvers, increasing the time available for observations. The aim of this thesis is to study the feasibility of utilizing Nonlinear Model Predictive Control (NMPC) for agile rest-to-rest satellite slews with consideration of flexible dynamics. Concerns related to the choice of Reaction Wheels (RWs) as actuators are also considered, including desaturation while slewing and avoidance of RW speeds that excite appendage vibrations. The performance of the control scheme is evaluated with regard to its ability to perform agile slews without exciting long-lasting vibrations and, to some extent, computational complexity. The flexible dynamics of the satellite are modeled using the Assumed Modes Method with Lagrange's equations. As NMPC prediction model, we utilize a single virtual state harmonic oscillator and corresponding Extended Kalman Filter. The thesis shows that the implemented control scheme performs well if it is appropriately tailored to the flexible dynamics at hand. The Nonlinear Model Predictive Control (NMPC) control scheme has the potential to increase the agility of flexible satellites.

Preface

This thesis is submitted as partial fulfillment of the Master of Science degree in Cybernetics and Robotics at the Norwegian University for Science and Technology. I would like to sincerely thank Prof. Sebastien Gros and Jesús Ramírez from SENER Aeroespacial for their advice and guidance throughout this year.

This thesis is a continuation of the TTK4550 specialization project completed in the fall of 2022 [1]. The specialization project developed most of the background theory, as well as a rudimentary controller scheme. Therefore, certain sections of this thesis are adapted from the corresponding sections in the specialization project. In particular, parts of Section 2.6, Section 3.1.1, and Section 3.1.2 have not been substantially altered.

Chapter 1

Introduction

1.1 Motivation

According to the 2021 European Union Agency for the Space Programme Market Report, Earth Observation (EO) data and service revenues are set to double from €2.8B to €5.5B within the coming decade [2]. This growing market is driving advancements in the design of EO satellites in order to improve both operational efficiency and data quality [3].

Recent advances in material science allow for satellite designs to trade off the rigidity of structures such as solar panels and antennas for a significantly decreased mass [4]. Advantages to this trade-off include lower energy consumption and reduced launch costs [5]. This trend poses a challenge for EO satellites as exciting vibrations in flexible structures can be detrimental to pointing accuracy. The simplest solution to this problem is to maneuver, or slew, the satellite slowly to avoid exciting vibration. But since long slew times generally reduce observational uptime, there is instead demand for a certain level of *agility* [4]. The ambition of this thesis is to contribute to the ongoing research conducted by SENER Aeroespacial on the potential of optimal control techniques to enhance EO satellite agility.

1.2 Related work

The spacecraft attitude control problem has been extensively studied. Solutions have historically involved control techniques such as Proportional-Derivative (PD), Linear-Quadratic (LQ), Lyapunov design, $\mathbf{H}_\infty$or Sliding Mode Control (SMC) [6]. This section provides a brief overview of attitude control solutions considering flexible dynamics and instances of optimization-based techniques such as Model Predictive Control (MPC) in attitude control.

$\mathbf{H}_\infty$control techniques involve formulating the control problem as an optimization problem over the space $\mathbf{H}_\infty$(all analytic and bounded functions in the right-half complex plane) and minimizing the $\mathbf{H}_\infty$norm [5]. The resulting controller is typically relatively robust and has satisfactory disturbance attenuation [7]. These qualities have made $\mathbf{H}_\infty$control a common control strategy in attitude control with flexible dynamics

[5, 8–10]. However, $\mathbf{H}_\infty$controllers are generally not considered to have fast convergence properties compared to other control schemes [11]. Other techniques have been applied, such as an adaptive PD + SMC approach in [12] and a nonlinear controller designed through the introduction of virtual constraints in [13]. Also somewhat related to the attitude control problem with flexible dynamics are efforts that attempt to directly damp vibrations in flexible structures, such as with piezoelectrics in [14, 15] and with shakers in [16].

Embedded and real-time optimization-based control offer an alternative to more traditional techniques and are ever-growing in popularity thanks to advances in computational technology [17]. By optimally exploiting satellite torque resources, optimization-based control techniques could be vital in achieving improved satellite agility [18]. Furthermore, the nature of optimization-based control, minimizing a pre-defined *cost function*, provides a flexible control scheme that can satisfy multiple objectives and system constraints [19].

Perhaps the most well-known real-time optimization scheme is MPC, in which the control input is determined by solving a numerical optimization problem at regular sampling intervals. In Nonlinear Model Predictive Control (NMPC), an optimization problem based on nonlinear system dynamics or constraints is generally more computationally demanding. In recent literature, there are many examples of MPC in attitude control for linear, linearized, and nonlinear attitude dynamics.

An early instance of NMPC applied to attitude control is that of [20], using a function-space NMPC approach in which the optimization solution is not recomputed at every sampling instant. In [21] and [22] a NMPC on the $SO(3)$ manifold is developed to avoid issues stemming from attitude representations with either singularities and double-coverings. Robust MPC was addressed in [23] and [24]. The latter utilizes Tube-Based MPC in which a "tube" of predicted system trajectories is considered to account for uncertainty. In [25], NMPC was utilized for attitude control while considering singularity avoidance of Control Moment Gyroscopes (CMGs). In [26–28] NMPC was applied to the problem of spacecraft rendezvous and docking, in which both translational and rotational motion must be considered.

In 2021 an article was published that compared a linear MPC scheme to the LQ Regulator for slews of flexible satellites about a single axis [29]. The study showed superior performance for the MPC scheme but does have certain limitations. The MPC was deployed with a sampling frequency much higher than that of the two modeled flexible modes that were both included in the MPC prediction model. Furthermore, the MPC was initialized using simulated modal amplitudes that are not directly measurable in a physical system. A 2022 study on linear MPC applied to attitude stabilization of a spacecraft with a large flexible rotating payload addresses these limitations to a larger extent introducing a significant mismatch between control and simulation model [30]. Due to the complex nature of the rotating flexible payload, the authors conclude the scheme to be unsatisfactory when faced with uncertain inertia parameters for the rotating structure. We note that this study did not specifically focus on slew maneuvers. Also worth noting are promising results obtained on NMPC for highly flexible aircraft [31, 32], which could provide an indication of the performance potential for slews of flexible satellites.

1.3 Scope and aim

Based on the overview of previous work in Section 1.2, there is room for exploring the attitude control problem for flexible satellites by means of NMPC. With the objective of improved agility, we will focus on demonstrating the viability of NMPC in performing agile slews. The proposed idea is to utilize NMPC for slewing up to a certain level of accuracy and subsequently transitioning to a more proven and conservative control scheme for final stabilization and observation (such as $\mathbf{H}_\infty$ in [5, 8–10], possibly including active vibration suppression as in [14–16]). Critical for this approach is the NMPC ensuring that the flexible dynamics are not significantly excited by the end of the slew. This prioritization was identified in conjunction with SENER Aeroespacial.

This thesis is limited to the design and demonstration of NMPC for agile slews. The emphasis on agile slews directs our focus to factors such as accurate simulation of flexible dynamics for larger displacements, actuator constraints and saturation, and internally produced disturbances such as imbalanced actuators. Conversely, the effects of external disturbances such as solar torques or aerodynamic drag are considered less important in this context.

The aim of this thesis is to study the feasibility of utilizing Nonlinear Model Predictive Control for agile rest-to-rest satellite slews with consideration of flexible dynamics. Concerns related to the choice of Reaction Wheels (RWs) as actuators are also considered, including desaturation while slewing and avoidance of RW speeds that excite appendage vibrations. The performance of the control scheme is evaluated with regard to its ability to perform agile slews without exciting long-lasting vibrations and, to some extent, computational complexity.

1.4 Contributions

The author has identified two main contributions to the field of attitude control in this thesis:

1. Key design considerations of a NMPC scheme for agile slewing of flexible satellites. Particularly regarding the choice of NMPC parameters, prediction model, and virtual state estimation.
2. Novel approaches to integrating Reaction Wheel management and desaturation into the NMPC scheme.

1.5 Thesis outline

Chapter 2 - Mathematical model presents the mathematical model of the satellite, which includes a nonlinear analytical model of the flexible dynamics based on Lagrange's equations.

Chapter 3 - Control scheme, theory presents relevant background theory on Nonlinear Model Predictive Control and the Extended Kalman Filter.

Chapter 4 - Controller design presents the particulars of the NMPC and EKF control scheme used for control of the model in Chapter 2.

Chapter 5 - Results and discussion presents and results of the thesis. Discussion of the results is done in the respective sections. The last section of this chapter presents prospects for future work.

Chapter 2

Mathematical model

In this chapter, we present the derivation of the mathematical model used for simulating the satellite with flexible dynamics. The assumptions and limitations of the model are, for the most part, listed in Section 2.5. Section 2.6 is in large part similar to the corresponding section in [1], with minor modifications for clarity. Section 2.8 presents the complete satellite model in a concise format.

2.1 Notation

$x \in \mathbb{R}$	Scalar
$\boldsymbol{x} \in \mathbb{R}^n$	Vector of dimension n
$\mathbf{X} \in \mathbb{R}^{m \times n}$	Matrix with m rows and n columns
$\boldsymbol{x}^\top$	The transpose of $\boldsymbol{x}$
$\mathbf{X}^{-1}$	The inverse of $\boldsymbol{X}$
$\|\boldsymbol{x}\|$	The 2-norm of $\boldsymbol{x}$
$\boldsymbol{x}^a$	$\boldsymbol{x}$ expressed in coordinate frame $(\cdot)^a$
$\frac{d}{dt}\boldsymbol{x}^a\big\|_b$	Time derivative of $\boldsymbol{x}^a$ in frame $(\cdot)^b$
$\dot{\boldsymbol{x}}^a$	Time derivative of $\boldsymbol{x}^a$ in frame $(\cdot)^a$
$\mathbf{R}_a^b$	Rotation matrix from frame $(\cdot)^a$ to frame $(\cdot)^b$
$\boldsymbol{\omega}_{ab}^c$	Angular velocity of frame $(\cdot)^b$ relative to frame $(\cdot)^a$, in frame $(\cdot)^c$
$\boldsymbol{x}^\times$	Skew-symmetric matrix corresponding to $\boldsymbol{x}$, see Eq. (2.9)
$\mathbf{I}_n$	The $(n \times n)$ identity matrix
$\det(\mathbf{X})$	Determinant of $\mathbf{X}$
$\text{null}(\mathbf{X})$	Null space of $\mathbf{X}$
$\text{col}_i(\mathbf{X})$	Column i of $\mathbf{X}$

Table 2.1: Mathematical notation used throughout this thesis

2.2 Reference frames

2.2.1 Inertial frame

The inertial frame, $(\cdot)^i$, is a right-handed frame with its origin at the center of the Earth. $\boldsymbol{x}^i$ points towards vernal equinox (the constellation Aries), and $\boldsymbol{z}^i$ points north. $\boldsymbol{y}^i = \boldsymbol{z}^i \times \boldsymbol{x}^i$ completes the right-handed frame. As its name implies, the inertial frame is assumed to be inertial, meaning it is not undergoing any acceleration.

2.2.2 Orbital frame

The orbital frame, $(\cdot)^i$, is a right-handed frame with its origin at the satellite's center of gravity. $\boldsymbol{x}^o$ points in the direction of the linear velocity of the satellite, while $\boldsymbol{z}^o$ points directly at the origin of the inertial frame. $\boldsymbol{y}^o$ completes the right-handed frame. The rotation matrix from the orbital frame to the inertial frame may be constructed as

$$\mathbf{R}_o^i = \begin{bmatrix} \boldsymbol{x}_o^i & \boldsymbol{y}_o^i & \boldsymbol{z}_o^i \end{bmatrix} \tag{2.1}$$

where

$$\boldsymbol{z}_o^i = -\frac{\boldsymbol{p}^i}{\|\boldsymbol{p}^i\|}, \quad \boldsymbol{x}_o^i = \frac{\boldsymbol{v}^i}{\|\boldsymbol{v}^i\|}, \quad \boldsymbol{y}_o^i = \boldsymbol{z}_o^i \times \boldsymbol{x}_o^i \tag{2.2}$$

$\boldsymbol{p}$ and $\boldsymbol{v}$ denote, respectively, the position and linear velocity of the satellite.

2.2.3 Body frame

The body frame, $(\cdot)^b$, is a right-handed frame that shares its origin with the orbital frame. The axes of the body frame are fixed to the body of the satellite. It is typically defined such that the corresponding inertia matrix is diagonal, or close to diagonal, in the body frame [33].

2.2.4 Reaction wheel array configuration in the body frame

The Reaction Wheel (RW) array utilized in this thesis consists of n_w RWs fixed within the body frame. Nominally, RWs only produce torque about their spin axes. The torque produced by a RW about its spin axis, τ_w^w, may be expressed in the body frame as τ_w^b through a constant rotation. By defining the $(3 \times n_w)$ torque distribution matrix, $\mathbf{L}_w^b$, with columns equal to the spin axes of the wheels in the body frame, we may write

$$\boldsymbol{\tau}_w^b = \mathbf{L}_w^b \boldsymbol{\tau}_w^w \tag{2.3}$$

where $\boldsymbol{\tau}_w^b$ is the torque applied by wheels in the body frame while $\boldsymbol{\tau}_w^w$ is a $(n_w \times 1)$ vector of wheel torques about their respective spin axes. We will, for clarity, refer to the superscript $(\cdot)^w$ as the wheel frame, even though it is not a right-handed reference frame. Introducing the wheel frame and $\mathbf{L}_w^b$ simplifies certain mathematical expressions throughout Chapter 2.

When considering imbalanced RWs, torque is no longer produced solely about the spin axes. Thus, the wheel frame, as defined above, is insufficient. This issue is dealt with in Section 2.7.3.

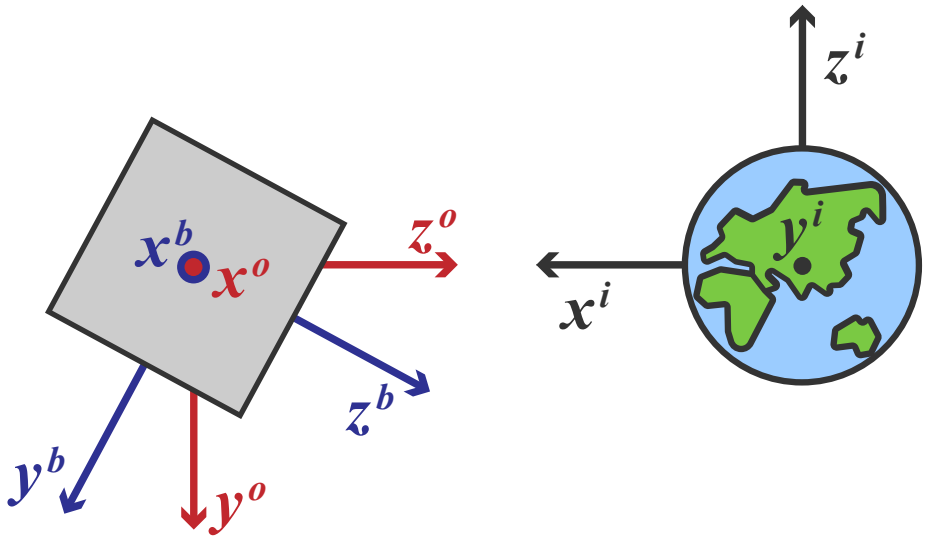

Figure 2.1: Figure depicting the inertial (black) and orbital (red) frames and the body (blue) frame in some arbitrary orientation. $\boldsymbol{x}^b$, $\boldsymbol{x}^o$ and $\boldsymbol{y}^i$ are pointing out of the paper.

2.3 Orbital dynamics

As this thesis is focused on single, agile attitude slews, only a circular equatorial orbit is considered. We also assume that the satellite's mass is negligible with respect to that of the Earth. Then, by Kepler's third law, the choice of orbit fixes all orbital parameters except the orbit height, h_o. For the entirety of this thesis, the orbital height will be fixed at $h_o = 600\text{km}$. This is a common orbit height for EO satellites [34].

Again by Kepler's third law, we may derive an expression for the angular orbital velocity, ω_o, for a satellite in a circular orbit

$$\omega_o = \sqrt{\frac{\mu}{\|\boldsymbol{p}^i\|^3}} \tag{2.4}$$

where μ is the standard gravitational parameter of the Earth. The choice of orbit gives that $\|\boldsymbol{p}^i\|$ is constant and equal to $R_\oplus + h_o$, where $R_\oplus$ is the radius of the Earth. For $h_o = 600\text{km}$, Eq. (2.4) evaluates to $\omega_o \approx 0.001\text{rad/s}$. By the definition of the orbital frame, we have

$$\boldsymbol{\omega}_{oi}^o = -\boldsymbol{\omega}_{io}^o = \begin{bmatrix} 0 \\ -\omega_o \\ 0 \end{bmatrix} \tag{2.5}$$

One effect experienced by orbiting satellites that will be modeled as a disturbance in this thesis is the gravity gradient torque. As was explained in [1], the gravity gradient torque arises from the fact that gravitational attraction is inversely proportional to the distance from Earth. Therefore, the different point masses comprising an orbiting body experience varying gravitational attraction. For non-symmetrical bodies, this effect adds up to the gravity gradient torque.

An expression for the gravity gradient torque, $\boldsymbol{\tau}_{gg}$, assuming a spherically symmetric gravity field is derived in [35]:

$$\boldsymbol{\tau}_{gg}^{b} = 3\frac{\mu}{\|\boldsymbol{p}^{i}\|^{3}}\boldsymbol{z}_{o}^{i} \times \left(\mathbf{J}\,\boldsymbol{z}_{o}^{i}\right) \tag{2.6}$$

The expression assumes a rigid satellite with inertia $\mathbf{J}$.

2.4 Rotations and quaternions

By the definition of the 3D rotation group, SO(3), a matrix must satisfy certain properties for it to encode a rotation [36]:

$$\mathrm{SO}(3) = \left\{\mathbf{R} | \mathbf{R} \in \mathbb{R}^{3\times 3}, \mathbf{R}^{\top}\mathbf{R} = \mathbf{I}_3, \det(\mathbf{R}) = 1\right\} \tag{2.7}$$

By Eq. (2.7), several other useful properties of rotation matrices emerge:

$$\mathbf{R}_{b}^{a} = \left(\mathbf{R}_{a}^{b}\right)^{\top} = \left(\mathbf{R}_{a}^{b}\right)^{-1} \tag{2.8a}$$

$$\mathbf{R}_{c}^{a} = \mathbf{R}_{b}^{a}\mathbf{R}_{c}^{b} \tag{2.8b}$$

$$\dot{\mathbf{R}}_{b}^{a} = (\boldsymbol{\omega}_{ab}^{a})^{\times}\mathbf{R}_{b}^{a} \tag{2.8c}$$

The skew-symmetric operator, $(\cdot)^{\times}$, transforms a vector to a skew-symmetric matrix:

$$\boldsymbol{s} = \begin{bmatrix} s_1 & s_2 & s_3 \end{bmatrix}^{\top} \quad \rightarrow \quad \boldsymbol{s}^{\times} = \begin{bmatrix} 0 & -s_3 & s_2 \\ s_3 & 0 & -s_1 \\ -s_2 & s_1 & 0 \end{bmatrix} \tag{2.9}$$

Due to the properties in Eq. (2.7), all 9 elements of a rotation matrix are not needed to define a rotation uniquely. We may instead describe rotations by a more compact *parametrization*. One such parametrization is the 4-parameter quaternion

$$\mathbf{q} = \begin{bmatrix} \mathrm{q}_1 \\ \mathbf{q}_{2:4} \end{bmatrix} \tag{2.10}$$

consisting of a scalar part, q_1, and a vector part, $\mathbf{q}_{2:4}$. The quaternions considered in this thesis are unit quaternions, constrained by $\mathbf{q}^{\top}\mathbf{q} = 1$. $\mathbf{q}_{ob}$ describes a rotation from body to orbit frame. Being the only quaternion considered in this thesis, we will denote it as $\mathbf{q}$. We may reconstruct the rotation matrix $\mathbf{R}_{b}^{o}$ from quaternions using

$$\mathbf{R}_{b}^{o} = \mathbf{I}_3 + 2\mathrm{q}_1\mathbf{q}_{2:4}^{\times} + 2\mathbf{q}_{2:4}^{\times}\mathbf{q}_{2:4}^{\times} \tag{2.11}$$

from [37]. Kinematic equations will also be needed for numerical simulation of the satellite attitude. These are given in [35] as

$$\dot{\mathbf{q}} = \frac{1}{2}\boldsymbol{\Xi}(\mathbf{q})\boldsymbol{\omega}_{ob}^{b}, \quad \boldsymbol{\Xi}(\mathbf{q}) = \begin{bmatrix} -\mathbf{q}_{2:4}^{\top} \\ \mathrm{q}_1\mathbf{I}_3 + \mathbf{q}_{2:4}^{\times} \end{bmatrix} \tag{2.12}$$

Unit quaternions avoid singularities by covering the space of rotations twice. Therefore, subtraction is generally not appropriate to represent differences in quaternions. The e error $\mathbf{q}_e$ is instead introduced:

$$\mathbf{q}_e = \bar{\mathbf{q}}^{-1} \odot \mathbf{q} \tag{2.13}$$

where

$$\mathbf{q}^{-1} = \begin{bmatrix} q_1 \\ -\mathbf{q}_{2:4} \end{bmatrix}, \quad \bar{\mathbf{q}} \odot \mathbf{q} = \begin{bmatrix} \bar{q}_1 q_1 - \bar{\mathbf{q}}_{2:4}^{\top} \mathbf{q}_{2:4} \\ q_1 \bar{\mathbf{q}}_{2:4} + \bar{q}_1 \mathbf{q}_{2:4} + \bar{\mathbf{q}}_{2:4}^{\times} \mathbf{q}_{2:4} \end{bmatrix} \tag{2.14}$$

with notation is consistent with that of [35]. The attitude error is considered zero when $\mathbf{q}_e$ has reached the *zero quaternion*:

$$\mathbf{q}_e = \begin{bmatrix} \pm 1 & \mathbf{0} \end{bmatrix}^{\top} \tag{2.15}$$

We will also introduce another measure of attitude error to aid analysis, namely the Line-Of-Sight (LOS) error. The sensing equipment of the satellite is placed with LOS along the $\boldsymbol{z}^b$ axis. If we assume that the desired orientation for observation is the orientation of the body frame, an approximate measure of the LOS error, e_{LOS}, may be stated as

$$\boldsymbol{z}_b^o = \begin{bmatrix} z_1 \\ z_2 \\ z_3 \end{bmatrix}, \quad e_{LOS} = h_o \sqrt{(z_1/z_3)^2 + (z_2/z_3)^2} \tag{2.16}$$

The measure does not account for the curvature of the Earth and is therefore not accurate for large e_{LOS}. But since the measure only will be used in comparing performance towards the end of maneuvers, it is sufficient for the purposes of this thesis.

2.5 Satellite configuration and model approach

This section sets the stage for the derivation of satellite dynamics by defining the satellite configuration in terms of its structure and actuators and discussing the necessary assumptions/limitations. Terms and concepts relevant to the remaining sections are introduced.

2.5.1 Orbital effects and perturbations

In the following sections, the orbital frame is assumed to be inertial. This limitation is justifiable for a set of reasons. One is the relative magnitude of the orbital velocity, Eq. (2.4), with respect to the body velocity for agile slew maneuvers. Furthermore, the orbital frequency is much lower than the resonant frequencies of the flexible dynamics [38], which will be made clear in Section 5.1. Considering the orbital frame as inertial eases the derivation of the flexible dynamics, as the translational velocity, $\boldsymbol{v}^i$, does not need to be considered. Though flexible modes may cause translational motion [38], the choice of actuators in this thesis does not allow for translational control authority. The neglection of orbital effects is common in literature [39–41], but certainly also a

limitation of this thesis. For an example of a model that includes orbital and translational effects, the reader is referred to [42].

Orbital disturbances that, in large part, affect the satellite attitude over longer time horizons, such as solar radiation pressure, aerodynamic drag, and magnetic disturbances, will not be included in the model. The exception is the gravity gradient torque from Eq. (2.6), included for its relative magnitude in LEO.

2.5.2 Rigid structure and actuators

The satellite's body is the structure to which all other components, such as flexible appendages and actuators, are attached. The body is assumed to be a perfectly rigid structure with moment of inertia $\mathbf{J}_b$. By Newton's second law, the angular momentum of the rigid body may be stated in the body frame as

$$\mathbf{h}_b^b = \mathbf{J}_b \boldsymbol{\omega}_{ob}^b \tag{2.17}$$

The dynamics of $\boldsymbol{\omega}_{ob}^b$ will be modeled jointly with the flexible appendages in Section 2.6.

Attached to the rigid body are n_w Reaction Wheels (RWs) to be utilized for active attitude control. RWs provide torque by *momentum exchange*, a principle rooted in Euler's second law. Put simply, an angular acceleration of an RW in one direction will cause the satellite to spin in the opposite direction. The angular momentum of the total system will remain constant in the absence of external torques. As in [33], the model of the RWs will not include electrical dynamics, friction, and the time constant associated with tracking a torque command. For a single RW in some inertial frame, we therefore have

$$\mathrm{h}_w = \mathrm{J}_w \omega_w \tag{2.18a}$$

$$\dot{\mathrm{h}}_w = \tau_w \tag{2.18b}$$

where h_w is the momentum of the wheel, J_w its moment inertia about the spin axis, ω_w its angular velocity and τ_w is the torque applied to the wheel.

For reaction wheels fixed within a rotating rigid body, gyroscopic coupling between $\boldsymbol{\omega}_{ob}^b$ and the wheel velocities must also be accounted for. This effect is derived, independently of the flexible dynamics, in Section 2.7.1. Furthermore, physical RWs have an imperfect mass distribution about their spin axes. The effects of this RW *imbalance* will be modeled as external torques according to European Cooperation for Space Standardization (ECSS) standards [43] in Section 2.7.3.

Over longer periods of operation, external disturbances acting on the satellite will be counteracted and accumulated by the RWs as *residual momentum*. Due to physical constraints, all RWs have a maximum realizable ω_w at which point the wheel is *saturated*. Therefore, residual momentum must be removed to avoid reaching saturation and subsequently losing control authority. The removal process is known as *desaturation* and is only possible by applying external torques [33]. One way of applying these external torques is through thrusters, which will be the case in this thesis. The thrusters are modeled as on/off external torques in Section 2.7.4. Disturbances caused by the thrusters or dynamic couplings with other parts of the satellite will not be included in the model.

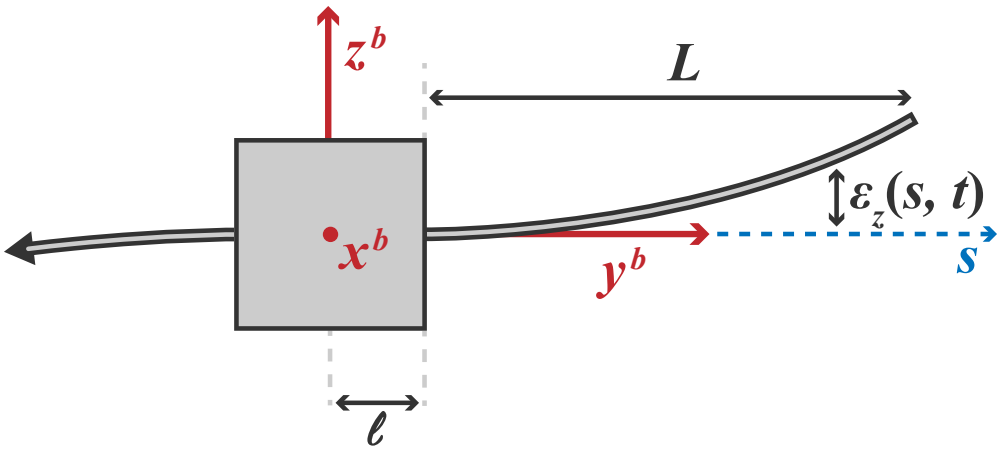

Figure 2.2: A figure displaying the two flexible solar panels and associated parameters. $\boldsymbol{x}^b$ is pointing out of the paper.

2.5.3 Flexible structure

The flexible structure of the satellite is visualized in Fig. 2.2. The two flexible solar panels extend from the rigid body in the $\boldsymbol{y}^b$ direction. The panels are mounted with a distance ℓ from the origin of the body frame and have a length of L. For any distance from the mounting point $s \in (0, L)$, the panel is displaced from its resting position by $\epsilon_z(s,t)$ in the $\boldsymbol{z}^b$ direction. This displacement will capture most of the dynamics associated with the excitation of lower-order flexible modes [38].

Displacement in the $\boldsymbol{x}^b$ direction or effects such as torsion or axial deformation will not be considered in this thesis. The tips of the panels are assumed to be at a constant length L from the rigid body in the $\boldsymbol{y}^b$ direction, meaning that zero elongation is not enforced. The model is, therefore, only valid for small displacements [44]. The reader is referred to [45] for a model in which elongation is not neglected. The displacements of the left and right panels are constrained to be anti-symmetrical, such that the system's center of mass always coincides with the center of the rigid body [39, 46]. Furthermore, as was justified in Section 2.5.1, the displacement of the panels will be assumed decoupled from the linear velocity of the satellite.

The panels will be modeled as Euler-Bernoulli beams with slender, homogenous mass distributions. The corresponding Partial Differential Equation (PDE) is given in [36] as

$$\frac{\partial^2 \epsilon_z}{\partial t^2} + \frac{EI^2}{\rho^2}\frac{\partial^4 \epsilon_z}{\partial s^4} = 0 \tag{2.19}$$

where ρ and EI denote the density and flexural rigidity of the beam, respectively. The following boundary conditions apply to Eq. (2.19):

$$\epsilon_z(0,t) = 0, \quad \frac{\partial}{\partial s}\epsilon_z(s,t)\bigg|_{s=0} = 0, \quad \frac{\partial^2}{\partial s^2}\epsilon_z(s,t)\bigg|_{s=L} = 0, \quad \frac{\partial^3}{\partial s^3}\epsilon_z(s,t)\bigg|_{s=L} = 0 \tag{2.20}$$

Since PDEs are difficult to manage both computationally and analytically, we will approximate the PDE to obtain Ordinary Differential Equations (ODEs) [36]. The Assumed Modes Method (AMM), as described in [39], is applied for approximation. It proposes to approximate the geometric shape of the entire flexible structure by a linear combination of n_m space-dependent *shape functions*, $\phi_k(s)$, multiplied by corresponding time-dependent *amplitude functions*, $\eta_k(t)$:

$$\epsilon_z(s,t) = \sum_{k=1}^{n_m} \phi_k(s)\eta_k(t), \quad k \in (1, n_m) \tag{2.21}$$

The shape functions, also known as admissible functions, must satisfy the boundary conditions of Eq. (2.20). The particular shape functions applied in Section 2.6 are those of [47], in which the kth mode is given by

$$\phi_k(s) = 1 - \cos\left(\frac{k\pi s}{L}\right) + \frac{1}{2}(-1)^{k+1}\left(\frac{k\pi s}{L}\right)^2 \tag{2.22}$$

This particular choice of shape functions is widely used when modeling Euler-Bernoulli beams on rotating structures [44, 48, 49]. The first six $\phi_k(s)$ are plotted in Fig. 2.3 for a panel length, L, of 4m. An analytical model using Lagrange's equations, where the η_k enter as generalized coordinates, is formulated in Section 2.6.

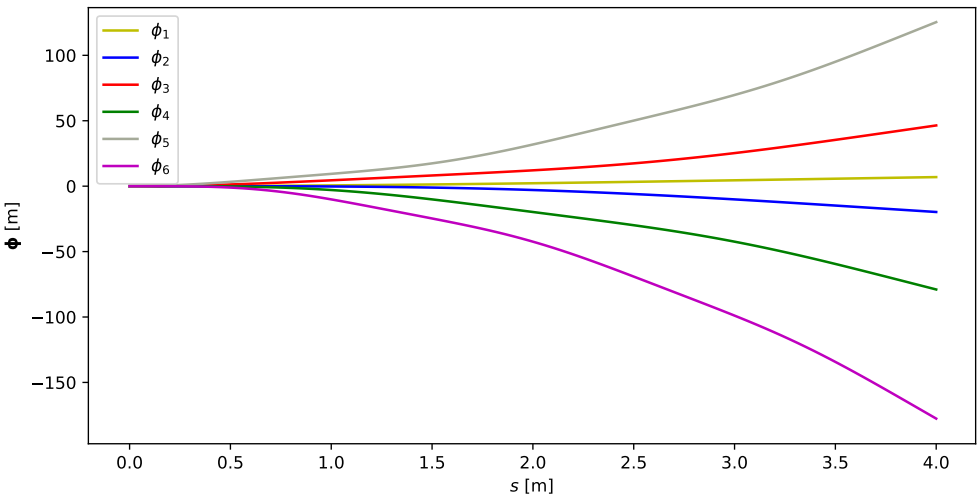

Figure 2.3: First 6 assumed mode shapes with Eq. (2.21), $L = 4$m

2.6 Analytical modelling

This section is largely similar to the corresponding section in the specialization project, [1], with minor adjustments for clarity. The analytical model describing the coupled dynamics of $\boldsymbol{\omega}_{ob}^{b}$ and $\epsilon_z(s,t)$ is developed using Lagrange's equations, given as

$$\frac{d}{dt}\left(\frac{\partial \mathcal{L}}{\partial \dot{\boldsymbol{q}}}\right) - \frac{\partial \mathcal{L}}{\partial \boldsymbol{q}} + \frac{\partial \mathcal{F}}{\partial \dot{\boldsymbol{q}}} = \mathbf{Q}, \quad \mathcal{L} = T - V \tag{2.23}$$

in which:

$\mathcal{L}$:	Lagrangian of the system
T:	Kinetic energy of the system
V:	Potential energy of the system
$\mathcal{F}$:	Dissipation function
$\boldsymbol{q}$:	Vector of generalized coordinates
$\boldsymbol{Q}$:	Vector of generalized forces

Table 2.2: Symbols in Lagrange's equations

The vector of generalized coordinates, $\boldsymbol{q}$, should not be confused with $\mathbf{q}$, the quaternion. It will become apparent in the following sections that

$$\boldsymbol{q} = \begin{bmatrix} \boldsymbol{\theta} \\ \boldsymbol{\eta} \end{bmatrix}, \quad \dot{\boldsymbol{q}} = \begin{bmatrix} \boldsymbol{\omega}_{ob}^{b} \\ \dot{\boldsymbol{\eta}} \end{bmatrix}, \quad \boldsymbol{\eta} = \begin{bmatrix} \eta_1 & \cdots & \eta_{n_m} \end{bmatrix}^{\top} \tag{2.24}$$

is a natural choice of generalized coordinates, $\boldsymbol{q}$. We note that $\boldsymbol{\theta}$, defined by $\dot{\boldsymbol{\theta}} = \boldsymbol{\omega}_{ob}$, is somewhat an abuse of notation. But since the term will not appear explicitly in our equations of motion, we do not bother with its exact definition. The three following subsections will develop expressions for the for T, V and $\mathcal{F}$ on the form:

$$\mathrm{T} = \frac{1}{2}\sum_{i=1}^{N}\sum_{j=1}^{N} m_{ij}\dot{q}_i\dot{q}_j = \dot{\boldsymbol{q}}^{\top}\mathbf{M}\dot{\boldsymbol{q}} \tag{2.25}$$

$$\mathrm{V} = \frac{1}{2}\sum_{i=1}^{N}\sum_{j=1}^{N} k_{ij}q_iq_j = \boldsymbol{q}^{\top}\mathbf{K}\boldsymbol{q} \tag{2.26}$$

$$\mathcal{F} = \frac{1}{2}\sum_{i=1}^{N}\sum_{j=1}^{N} c_{ij}q_iq_j = \dot{\boldsymbol{q}}^{\top}\mathbf{C}\dot{\boldsymbol{q}} \tag{2.27}$$

which will be incorporated in Eq. (2.23) in Section 2.6.4, yielding a set of ODEs describing the coupled structural dynamics.

2.6.1 Kinetic energy

Based on the description of the flexible structure in Section 2.5.3, we may express the position of any infinitesimal mass, dm, on the panel as

$$\mathbf{r}_p = \begin{bmatrix} 0 & s+\ell & \epsilon_z \end{bmatrix}^\top \tag{2.28}$$

By the transport theorem, we may express the velocity of any dm in the orbital frame as

$$\mathbf{v}_p = \boldsymbol{\omega}_{ob}^b \times \mathbf{r}_p + \dot{\boldsymbol{\epsilon}}, \quad \dot{\boldsymbol{\epsilon}} = \begin{bmatrix} 0 & 0 & \dot{\epsilon}_z \end{bmatrix}^\top \tag{2.29}$$

Since only anti-symmetric deformations are considered, as explained in Section 2.5.3, we may formulate the kinetic energy of the system in the orbital frame as the sum of that of the rigid body and the two beams:

$$\mathrm{T} = \mathrm{T}_{rigid} + 2 \cdot \mathrm{T}_{beam} = \frac{1}{2} \boldsymbol{\omega}_{ob}^{b\,\top} \mathbf{J}_b \boldsymbol{\omega}_{ob}^b + 2 \cdot \frac{1}{2} \int_{beam} \mathbf{v}_p^\top \mathbf{v}_p \, dm \tag{2.30}$$

By the assumption that the beam is slender and homogeneous, we may rewrite the integral in Eq. (2.30) as

$$\int_{beam} \mathbf{v}_p^\top \mathbf{v}_p \, dm = \rho \int_0^L \mathbf{v}_p^\top \mathbf{v}_p \, ds \tag{2.31}$$

wherein ρ denotes the density of the beam per length. Exploiting the properties of the cross product and skew-symmetric matrices, we reformulate expressions for $\boldsymbol{v}_p$ and $\boldsymbol{v}_p^\top$

$$\mathbf{v}_p = -\mathbf{r}_p^\times \boldsymbol{\omega}_{ob}^b + \dot{\boldsymbol{\epsilon}}, \quad \mathbf{v}_p^\top = \boldsymbol{\omega}_{ob}^{b\,\top} \mathbf{r}_p^\times + \dot{\boldsymbol{\epsilon}}^\top \tag{2.32}$$

and expand the right side of Eq. (2.29) by insertion of Eq. (2.32), giving

$$\rho \int_0^L \mathbf{v}_p^\top \mathbf{v}_p \, ds = \rho \left(- \int_0^L \boldsymbol{\omega}_{ob}^{b\,\top} \mathbf{r}_p^\times \mathbf{r}_p^\times \boldsymbol{\omega}_{ob}^b \, ds + \int_0^L \boldsymbol{\omega}_{ob}^{b\,\top} \mathbf{r}_p^\times \dot{\boldsymbol{\epsilon}} \, ds - \int_0^L \dot{\boldsymbol{\epsilon}}^\top \mathbf{r}_p^\times \boldsymbol{\omega}_{ob}^b \, ds + \int_0^L \dot{\boldsymbol{\epsilon}}^\top \dot{\boldsymbol{\epsilon}} \, ds \right) \tag{2.33}$$

We now define the matrix

$$\boldsymbol{\Phi} = \begin{bmatrix} 0 & \cdots & 0 \\ 0 & \cdots & 0 \\ \phi_1 & \cdots & \phi_N \end{bmatrix} \tag{2.34}$$

such that we may approximate $\dot{\boldsymbol{u}}$ as $\boldsymbol{\Phi}\dot{\boldsymbol{\eta}}$ by the assumed modes method. Substituting $\dot{\boldsymbol{u}}$ with $\boldsymbol{\Phi}\dot{\boldsymbol{\eta}}$ and moving the terms not dependent on s outside the integrals, we may further expand Eq. (2.33):

$$\boldsymbol{\omega}_{ob}^{b\,\top} \rho \int_0^L -\mathbf{r}^\times \mathbf{r}^\times \, ds \, \boldsymbol{\omega}_{ob}^b + \boldsymbol{\omega}_{ob}^{b\,\top} \rho \int_0^L \mathbf{r}^\times \boldsymbol{\Phi} \, ds \, \dot{\boldsymbol{\eta}} - \dot{\boldsymbol{\eta}}^\top \rho \int_0^L \boldsymbol{\Phi}^\top \mathbf{r}^\times \, ds \, \boldsymbol{\omega}_{ob}^b + \dot{\boldsymbol{\eta}}^\top \rho \int_0^L \boldsymbol{\Phi}^\top \boldsymbol{\Phi} \, ds \, \dot{\boldsymbol{\eta}} \tag{2.35}$$

For the choice of generalized derivatives suggested in Section 2.6, $\dot{\boldsymbol{q}} = \begin{bmatrix} \boldsymbol{\omega}_{ob}^{b} & \dot{\boldsymbol{\eta}} \end{bmatrix}^{\top}$, we may now construct the "mass matrix" $\mathbf{M}(\boldsymbol{q})$:

$$\mathbf{M}(\boldsymbol{q}) = \left[\begin{array}{c:c} \mathbf{J}_b + 2\rho \int_0^L -\mathbf{r}_p^{\times}\mathbf{r}_p^{\times}\, ds & 2\rho \int_0^L \mathbf{r}_p^{\times}\boldsymbol{\Phi}\, ds \\ \hdashline 2\rho \int_0^L \boldsymbol{\Phi}^{\top}\mathbf{r}_p^{\times}\, ds & 2\rho \int_0^L \boldsymbol{\Phi}^{\top}\boldsymbol{\Phi}\, ds \end{array}\right] \tag{2.36}$$

such that the expression for the kinetic energy, Eq. (2.30), can be stated on the form of Eq. (2.25):

$$\mathrm{T} = \frac{1}{2}\begin{bmatrix} \boldsymbol{\omega}_{ob}^{b} \\ \dot{\boldsymbol{\eta}} \end{bmatrix}^{\top} \mathbf{M}(\boldsymbol{q}) \begin{bmatrix} \boldsymbol{\omega}_{ob}^{b} \\ \dot{\boldsymbol{\eta}} \end{bmatrix} \tag{2.37}$$

To highlight the structure of $\mathbf{M}(\boldsymbol{q})$ and the terms causing the dependence on $\boldsymbol{q}$, we will expand Eq. (2.36) once more. Defining

$$\mathbf{M}(\boldsymbol{q}) = \left[\begin{array}{c:c} \mathbf{M}_{11}(\boldsymbol{q}) & \mathbf{M}_{12} \\ \hdashline \mathbf{M}_{21} & \mathbf{M}_{22} \end{array}\right] \tag{2.38}$$

we get the following expression for the matrix relating the angular velocity terms, $\mathbf{M}_{11}(\boldsymbol{q})$:

$$\mathbf{M}_{11}(\boldsymbol{q}) = \mathbf{J}_b + \begin{bmatrix} 2\rho \int_0^L \epsilon_z^2 + (s+\ell)^2\, ds & 0 & 0 \\ 0 & 2\rho \int_0^L \epsilon_z^2\, ds & -2\rho \int_0^L (s+\ell)\epsilon_z\, ds \\ 0 & -2\rho \int_0^L (s+\ell)\epsilon_z\, ds & 2\rho \int_0^L (s+\ell)^2\, ds \end{bmatrix} \tag{2.39}$$

in which the terms

$$\begin{aligned} \int_0^L \epsilon_z^2 &= \int_0^L \left(\sum_{k=1}^{n_m} \phi_k \eta_k\right)^2 ds \\ &= \eta_1^2 \int_0^L \phi_1^2\, ds + 2\eta_1\eta_2\rho \int_0^L \phi_1\phi_2\, ds + \cdots + \eta_{n_m}^2 \rho \int_0^L \phi_{n_m}^2\, ds \end{aligned} \tag{2.40}$$

and

$$\int_0^L (s+\ell)\epsilon_z\, dm = \int_0^L (s+\ell) \sum_{k=1}^{n_m} \phi_k \eta_k\, ds = \sum_{k=1}^{n_m} \eta_k \int_0^L (s+\ell)\phi_k\, ds \tag{2.41}$$

cause the dependence of $\mathbf{M}$ on the time-dependent functions $\boldsymbol{\eta}$ and subsequently on $\boldsymbol{q}$. Furthermore, matrices that describe the interaction between the $\boldsymbol{\eta}$ and $\boldsymbol{\omega}_{ob}^{b}$, $\mathbf{M}_{12}$ and

$\mathbf{M}_{21}$, are stated as

$$\mathbf{M}_{21}^{\top} = \mathbf{M}_{12} = \begin{bmatrix} 2\rho\int_0^L (s+\ell)\phi_1\,ds & 2\rho\int_0^L (s+\ell)\phi_2\,ds & \cdots & 2\rho\int_0^L (s+\ell)\phi_N\,ds \\ 0 & 0 & \cdots & 0 \\ 0 & 0 & \cdots & 0 \end{bmatrix} \tag{2.42}$$

Lastly, we have the matrix describing the interaction between the different assumed modes:

$$\mathbf{M}_{22} = \begin{bmatrix} \rho\int_0^L \phi_1^2\,ds & \rho\int_0^L \phi_1\phi_2\,ds & \cdots & \rho\int_0^L \phi_1\phi_{n_m}\,ds \\ \rho\int_0^L \phi_2\phi_1\,ds & \rho\int_0^L \phi_2^2\,ds & \cdots & \rho\int_0^L \phi_2\phi_{n_m}\,ds \\ \vdots & \vdots & \ddots & \vdots \\ \rho\int_0^L \phi_{n_m}\phi_1\,ds & \rho\int_0^L \phi_{n_m}\phi_2\,ds & \cdots & \rho\int_0^L \phi_{n_m}^2\,ds \end{bmatrix} \tag{2.43}$$

2.6.2 Potential energy

The potential energy of the satellite structure in the orbit frame is simply that of the two beams:

$$V = 2 \cdot V_{beam} \tag{2.44}$$

By applying the expression for the potential energy of an Euler-Bernoulli beam given in [36] we obtain:

$$\begin{aligned} V &= 2 \cdot \frac{1}{2}\int_0^L EI\left(\frac{\partial^2 \epsilon_z}{\partial^2 s}\right)^2 ds = \int_0^L EI\left(\frac{\partial^2 \sum_{k=0}^{n_m}\phi_k\eta_k}{\partial^2 s}\right)^2 ds \\ &= \int_0^L EI\left(\frac{\partial^2\phi_1\eta_1}{\partial^2 s} + \cdots + \frac{\partial^2\phi_{n_m}\eta_{n_m}}{\partial^2 s}\right)^2 ds \end{aligned} \tag{2.45}$$

For the same choice of generalized coordinates as in Section 2.6.1, this expression may be expressed in matrix form as

$$\mathrm{V} = \frac{1}{2}\boldsymbol{q}^{\top}\mathbf{K}\boldsymbol{q} \tag{2.46}$$

by defining the "stiffness matrix", **K**, as

$$\mathbf{K} = \begin{bmatrix} \mathbf{0}_{3\times3} & \mathbf{0}_{3\times1} & \mathbf{0}_{3\times1} & \cdots & \mathbf{0}_{3\times1} \\ \mathbf{0}_{1\times3} & 2EI\int_0^L(\frac{\partial^2\phi_1}{\partial^2 s})^2 ds & 2EI\int_0^L \frac{\partial^2\phi_1}{\partial^2 s}\frac{\partial^2\phi_2}{\partial^2 s} ds & \cdots & 2EI\int_0^L \frac{\partial^2\phi_1}{\partial^2 s}\frac{\partial^2\phi_{n_m}}{\partial^2 s} ds \\ \mathbf{0}_{1\times3} & 2EI\int_0^L \frac{\partial^2\phi_2}{\partial^2 s}\frac{\partial^2\phi_1}{\partial^2 s} ds & 2EI\int_0^L(\frac{\partial^2\phi_2}{\partial^2 s})^2 ds & \cdots & 2EI\int_0^L \frac{\partial^2\phi_2}{\partial^2 s}\frac{\partial^2\phi_{n_m}}{\partial^2 s} ds \\ \vdots & \vdots & \vdots & \ddots & \vdots \\ \mathbf{0}_{1\times3} & 2EI\int_0^L \frac{\partial^2\phi_{n_m}}{\partial^2 s}\frac{\partial^2\phi_1}{\partial^2 s} ds & 2EI\int_0^L \frac{\partial^2\phi_{n_m}}{\partial^2 s}\frac{\partial^2\phi_2}{\partial^2 s} ds & \cdots & 2EI\int_0^L(\frac{\partial^2\phi_{n_m}}{\partial^2 s})^2 ds \end{bmatrix} \tag{2.47}$$

2.6.3 Dissipation

The dissipation forces, the most important of which is viscous damping, are approximated by the Rayleigh dissipation function:

$$\mathcal{F}_{beam} = \frac{1}{2}\int_0^L k_d \left(\frac{\partial^2 \dot{\epsilon}_z}{\partial^2 s}\right)^2 ds \tag{2.48}$$

in which k_d are damping coefficients [40]. We may express the

$$\mathcal{F} = \frac{1}{2}\dot{\boldsymbol{q}}^\top \mathbf{C}\dot{\boldsymbol{q}} \tag{2.49}$$

by defining **C**, the "dissipation matrix":

$$\mathbf{C} = \begin{bmatrix} \mathbf{0}_{3\times3} & \mathbf{0}_{3\times1} & \mathbf{0}_{3\times1} & \cdots & \mathbf{0}_{3\times1} \\ \mathbf{0}_{1\times3} & 2k_d\int_0^L(\frac{\partial^2\phi_1}{\partial^2 s})^2 ds & 2k_d\int_0^L \frac{\partial^2\phi_1}{\partial^2 s}\frac{\partial^2\phi_2}{\partial^2 s} ds & \cdots & 2k_d\int_0^L \frac{\partial^2\phi_1}{\partial^2 s}\frac{\partial^2\phi_{n_m}}{\partial^2 s} ds \\ \mathbf{0}_{1\times3} & 2k_d\int_0^L \frac{\partial^2\phi_2}{\partial^2 s}\frac{\partial^2\phi_1}{\partial^2 s} ds & 2k_d\int_0^L(\frac{\partial^2\phi_2}{\partial^2 s})^2 ds & \cdots & 2k_d\int_0^L \frac{\partial^2\phi_2}{\partial^2 s}\frac{\partial^2\phi_{n_m}}{\partial^2 s} ds \\ \vdots & \vdots & \vdots & \ddots & \vdots \\ \mathbf{0}_{1\times3} & 2k_d\int_0^L \frac{\partial^2\phi_{n_m}}{\partial^2 s}\frac{\partial^2\phi_1}{\partial^2 s} ds & 2k_d\int_0^L \frac{\partial^2\phi_{n_m}}{\partial^2 s}\frac{\partial^2\phi_2}{\partial^2 s} ds & \cdots & 2k_d\int_0^L(\frac{\partial^2\phi_{n_m}}{\partial^2 s})^2 ds \end{bmatrix} \tag{2.50}$$

2.6.4 Developing Lagrange's equations

Having found suitable expressions for T, V, and $\mathcal{F}$, we may further develop Lagrange's equations to obtain the particularized ODEs. By substituting Eqs. (2.37, 2.46, 2.49) into Eq. (2.23) and applying the derivatives, we obtain

$$\mathbf{M}(\boldsymbol{q})\ddot{\boldsymbol{q}} + \dot{\mathbf{M}}(\boldsymbol{q},\dot{\boldsymbol{q}})\dot{\boldsymbol{q}} - \frac{1}{2}\dot{\boldsymbol{q}}^{\top}\frac{\partial \mathbf{M}(\boldsymbol{q})}{\partial \boldsymbol{q}}\dot{\boldsymbol{q}} + \mathbf{C}\dot{\boldsymbol{q}} + \mathbf{K}\boldsymbol{q} = \mathbf{Q}(\boldsymbol{q}) \tag{2.51}$$

The matrix $\dot{\mathbf{M}}(\boldsymbol{q},\dot{\boldsymbol{q}})$ is given by

$$\dot{\mathbf{M}}(\boldsymbol{q},\dot{\boldsymbol{q}}) = \begin{bmatrix} \dot{\mathbf{M}}_{11}(\boldsymbol{q},\dot{\boldsymbol{q}}) & \mathbf{0}_{3\times n_m} \\ \mathbf{0}_{n_m\times 3} & \mathbf{0}_{n_m\times n_m} \end{bmatrix} \tag{2.52}$$

where

$$\dot{\mathbf{M}}_{11}(\boldsymbol{q},\dot{\boldsymbol{q}}) = \begin{bmatrix} 2\frac{d}{dt}\left(\rho\int_0^L {\epsilon_z}^2\, ds\right) & 0 & 0 \\ 0 & 2\frac{d}{dt}\left(\rho\int_0^L {\epsilon_z}^2\, ds\right) & -2\frac{d}{dt}\left(\rho\int_0^L (s+\ell)\epsilon_z\, ds\right) \\ 0 & -2\frac{d}{dt}\left(\rho\int_0^L (s+\ell)\epsilon_z\, ds\right) & 0 \end{bmatrix} \tag{2.53}$$

The dependence on both $\boldsymbol{q}$ and $\dot{\boldsymbol{q}}$ is clear from the chain rule applied to Eq. (2.40).

The $(n_m \times n_m \times n_m)$ matrix $\partial\mathbf{M}(\boldsymbol{q})/\partial\boldsymbol{q}$ was left to be computed by the inbuilt `jtimes` function in CasADi. Because $\mathbf{M}_{12}$, $\mathbf{M}_{21}$ and $\mathbf{M}_{22}$ do not depend on $\boldsymbol{q}$, only the three first rows of $\frac{1}{2}\dot{\boldsymbol{q}}^{\top}(\partial\mathbf{M}(\boldsymbol{q})/\partial\boldsymbol{q})\dot{\boldsymbol{q}}$ are nonzero. Therefore, we will, for the sake of compact notation, define

$$\mathbf{M}_{\partial}(\boldsymbol{q},\dot{\boldsymbol{q}}) := \frac{1}{2}\dot{\boldsymbol{q}}^{\top}\frac{\partial \mathbf{M}(\boldsymbol{q})}{\partial \boldsymbol{q}}\dot{\boldsymbol{q}}[:3] \tag{2.54}$$

in which the notation $[:3]$ is used to represent the three first rows of the expression.

The vector of generalized forces may be stated as

$$\mathbf{Q}(\boldsymbol{q}) = \begin{bmatrix} \boldsymbol{\tau} + \left(\mathbf{M}_{11}(\boldsymbol{q})\,\boldsymbol{\omega}_{ob}^{b}\right)^{\times}\boldsymbol{\omega}_{ob}^{b} \\ \mathbf{0}_{n_m\times 1} \end{bmatrix} \tag{2.55}$$

in which $\boldsymbol{\tau}$ represents torques on the rigid body, and the term $\left(\mathbf{M}_{11}(\boldsymbol{q})\,\boldsymbol{\omega}_{ob}^{b}\right)^{\times}\boldsymbol{\omega}_{ob}^{b}$ accounts for the rotating nature of the system [50]. The effects of the actuators are added in Section 2.7 through $\boldsymbol{\tau}$. In Section 2.8, the complete model is stated explicitly in $\boldsymbol{\omega}_{ob}^{b}$ and $\boldsymbol{\eta}$.

2.7 Modelling actuators

This section covers modeling aspects related to the addition of actuators - RW dynamics, configuration, and imbalance, as well as a note on the use of thrusters for desaturation. We again note that the orbital frame is assumed to be inertial to maintain consistency with Section 2.6.

2.7.1 Reaction Wheel dynamics

The angular momentum of a rigid satellite actuated by RWs relative to the orbit frame is stated in [51, 52] as

$$\mathbf{h}_{tot}^{b} = \mathbf{J}_b \boldsymbol{\omega}_{ob}^{b} + \mathbf{h}_{w}^{b} \tag{2.56}$$

The equation resembles Eq. (2.17) but with the addition of $\mathbf{h}_w^b$, the angular momentum of the RW array in the body frame. By applying the transport theorem, we may obtain an expression for $\mathbf{h}_{tot}^b$ in the orbital frame:

$$\left.\frac{d}{dt}\mathbf{h}_{tot}\right|_o = \mathbf{J}_b \left.\frac{d}{dt}\boldsymbol{\omega}_{ob}^{b}\right|_b + \left.\frac{d}{dt}\mathbf{h}_{w}^{b}\right|_b + \boldsymbol{\omega}_{ob}^{b} \times \left(\mathbf{J}_b \boldsymbol{\omega}_{ob}^{b} + \mathbf{h}_{w}^{b}\right) \tag{2.57}$$

giving

$$\mathbf{J}_b \dot{\boldsymbol{\omega}}_{ob}^{b} + \left(\boldsymbol{\omega}_{ob}^{b}\right)^{\times} \left(\mathbf{J}_b \boldsymbol{\omega}_{ob}^{b}\right) = -\dot{\mathbf{h}}_{w}^{b} + \left(\mathbf{h}_{w}^{b}\right)^{\times} \boldsymbol{\omega}_{ob}^{b} = -\mathbf{L}_{w}^{b} \mathbf{J}_w \dot{\boldsymbol{\omega}}_{bw}^{w} + \left(\mathbf{L}_{w}^{b} \mathbf{J}_w \boldsymbol{\omega}_{bw}^{w}\right)^{\times} \boldsymbol{\omega}_{ob}^{b} \tag{2.58}$$

in which $\mathbf{L}_w^b$ is the torque distribution matrix as defined in Section 2.2.4, $\mathbf{J}_w$ is a $(n_w \times n_w)$ diagonal matrix of wheel inertia about respective spin axes, and $\boldsymbol{\omega}_{bw}^{w}$ is an $(n_w \times 1)$ vector of wheel velocities. The right-hand side of Eq. (2.58), describing RW torque and gyroscopic coupling, is included the dynamics of $\boldsymbol{\omega}_{ob}^{b}$ through $\boldsymbol{\tau}$ of Eq. (2.55). To develop the dynamics of $\dot{\boldsymbol{\omega}}_{bw}^{w}$, we first state the angular momentum of the RW, given in [52], as

$$\mathbf{h}_{w}^{w} = \mathbf{J}_w \mathbf{L}_{w}^{b^{\top}} \boldsymbol{\omega}_{ob}^{b} + \mathbf{J}_w \boldsymbol{\omega}_{bw}^{w} \tag{2.59}$$

and apply the transport theorem

$$\left.\frac{d}{dt}\mathbf{h}_{w}^{w}\right|_o = \mathbf{J}_w \mathbf{L}_{w}^{b^{\top}} \dot{\boldsymbol{\omega}}_{ob}^{b} + \mathbf{J}_w \dot{\boldsymbol{\omega}}_{bw}^{w} + (\mathbf{L}_{w}^{b^{\top}} \boldsymbol{\omega}_{ob}^{b} + \boldsymbol{\omega}_{ow}^{w})^{\times} (\mathbf{J}_w \mathbf{L}_{w}^{b^{\top}} \boldsymbol{\omega}_{ob}^{b} + \mathbf{J}_w \boldsymbol{\omega}_{ow}^{w}) \tag{2.60}$$

We now assume identical inertia for all RWs such that $\mathbf{J}_w = J_w \mathrm{I}_{nw}$. Thus, the skew-symmetric term in Eq. (2.60) is equal to 0 by the property of the cross product s that $\boldsymbol{s} \times \boldsymbol{s} = 0$ for any $\boldsymbol{s}$. We may now state the dynamics of $\dot{\boldsymbol{\omega}}_{bw}^{w}$ as

$$\mathbf{J}_w \mathbf{L}_{w}^{b^{\top}} \dot{\boldsymbol{\omega}}_{ob}^{b} + \mathbf{J}_w \dot{\boldsymbol{\omega}}_{bw}^{w} = \boldsymbol{\tau}_{w}^{w} \tag{2.61}$$

Section 2.8 states the full model of $\boldsymbol{\omega}_{ob}^{b}$ and $\boldsymbol{\eta}, \dot{\boldsymbol{\eta}}$, in which the effects of Eq. (2.58) and Eq. (2.61) are included.

2.7.2 Reaction Wheel configuration and null motion

The simplest RW configuration that provides three-axis control authority is that of three RWs with spin axes aligned with the body frame axes [33]. The corresponding torque distribution matrix, $\mathbf{L}_w^b$, is simply $\mathbf{I}_3$. One reason to instead choose a configuration with more than three RWs is that of redundancy in case one wheel fails [35]. The other, which is of a larger concern in this thesis, is the possibility of *null motion* within the RW array [51].

Formally, the null space of a linear map $F : V \to W$ between two vector spaces V and W is the space of all $\boldsymbol{v} \in V$ such that $F(\boldsymbol{v}) = \mathbf{0}$. In the case of the linear mapping from torque commands in the wheel frame to the body frame, we have:

$$\boldsymbol{\tau}_w^b = F\left(\boldsymbol{\tau}_w^w\right) = \mathbf{L}_w^b \boldsymbol{\tau}_w^w, \quad \boldsymbol{\tau}_w^b \in W \subset \mathbb{R}^3, \quad \boldsymbol{\tau}_w^w \in V \subset \mathbb{R}^{n_w} \tag{2.62}$$

Thus the null space of F is the set of $\boldsymbol{\tau}_w^w$ that do not produce a torque on the spacecraft. Put differently, by the existence of the null space of F there is no unique choice of $\boldsymbol{\tau}_w^w$ in realizing any $\boldsymbol{\tau}_w^w$ [35]. Therefore, we gain control authority over $\boldsymbol{\omega}_{bw}^w$, in addition to that of the spacecraft attitude, which may be utilized to achieve secondary objectives.

The RW configuration to be used in this thesis is the commonly used pyramid configuration [35]. In this configuration, all four RWs provide torque about two body axes. The configuration is visualized in Fig. 2.4.

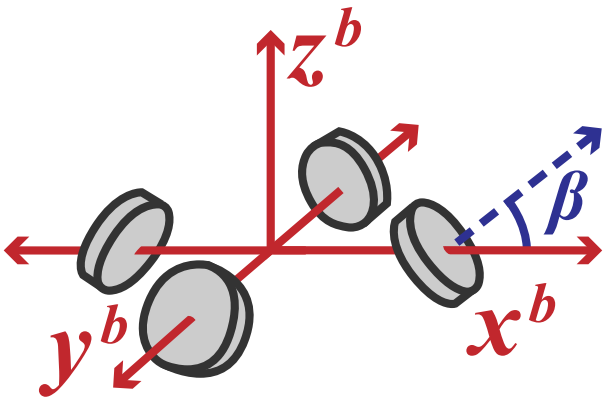

Figure 2.4: An illustration of the specific 4-RW pyramid configuration to be used in this thesis.

The torque distribution matrix for the specific configuration in Fig. 2.4, with β as shown in the figure, is stated as

$$\mathbf{L}_w^b = \begin{bmatrix} \cos\beta & 0 & -\cos\beta & 0 \\ 0 & \cos\beta & 0 & -\cos\beta \\ \sin\beta & \sin\beta & \sin\beta & \sin\beta \end{bmatrix} \tag{2.63}$$

For the $\mathbf{L}_w^b$ in Eq. (2.63), the set of all vectors in null space may be written as

$$\text{null}(\mathbf{L}_w^b) = \left\{ u_{null} \cdot \begin{bmatrix} 1 & -1 & 1 & -1 \end{bmatrix}^\top, \quad u_{null} : \boldsymbol{\tau}_w^w \in V \right\} \tag{2.64}$$

where u_{null} is constrained such that the torque limits of the wheels are respected.

2.7.3 Reaction Wheel imbalance

In many spacecraft, RWs have been found to be the most severe sources of micro-vibrations [43]. The disturbances are due to more significant static and dynamic rotating mass imbalances, and less significant imperfections in the ball bearing or motor [43]. Only static imbalance is of concern in this thesis, which will be modeled as an external torque.

Static imbalance is the offset of the center of mass of the RW from the rotation axis by some distance c_w. An expression for the static imbalance torque in the body frame, $\boldsymbol{\tau}_s^b$, is given in [35]:

$$\boldsymbol{\tau}_s^b = \sum_{i=0}^{n_w} (\boldsymbol{p}_{w_i}^b)^\times \mathbf{F}_{s,i}^b \tag{2.65}$$

in which $\boldsymbol{p}_{w_i}^b$ is the position of wheel center of mass i in the body frame and $\mathbf{F}_{s,i}^b$ is the static imbalance force of wheel i:

$$\mathbf{F}_{s,i}^b = m_w \omega_{w_i}^2 (\boldsymbol{x}_{w_i}^b)^\times \left((\boldsymbol{x}_{w_i}^b)^\times \boldsymbol{c}_{w_i}^b \right) \tag{2.66}$$

m_w is the mass of the wheel, chosen to be equal for all RWs. ω_{w_i} is the angular velocity of the wheel about its spin axis, $\boldsymbol{x}_{w_i}^b$ is a unit vector along the axis of rotation, and $\boldsymbol{c}_{w_i}^b$ is a vector from the nominal center of mass to the actual center of mass. The nominal center of mass is perfectly located on the spin axis. By the definition of the torque distribution matrix, we have:

$$\boldsymbol{x}_{w_i}^b = \mathrm{col}_i \left(\mathbf{L}_w^b \right), \quad (i = 1, \ldots, n_w) \tag{2.67}$$

where col_i denotes the ith column. Since $\boldsymbol{c}_{w_i}^b$ rotates with the speed of ω_{w_i}, we may find its expression by introducing individual right-handed wheel frames, w_i. $\boldsymbol{c}_{w_i}^b$ may then be stated as

$$\boldsymbol{c}_{w_i}^b = \mathbf{R}_{w_i}^b \begin{bmatrix} 0 & c_w \cos(\alpha_{w_i}) & c_w \sin(\alpha_{w_i}) \end{bmatrix}^\top \tag{2.68}$$

where $\mathbf{R}_{w_i}^b$ is the rotation matrix between wheel frame w_i and the body frame, and α_{w_i} is the angle between the center of mass vector and its implicitly defined zero-position along the $\boldsymbol{y}_{w_i}$ axis.

For the pyramid array, Eq. (2.63), we define the matrix $\mathbf{Y}_w$:

$$\mathbf{Y}_w = \begin{bmatrix} 0 & -1 & 0 & 1 \\ 1 & 0 & -1 & 0 \\ 0 & 0 & 0 & 0 \end{bmatrix} \tag{2.69}$$

such that

$$\boldsymbol{y}_{w_i}^b = \mathrm{col}_i \left(\mathbf{Y}_w \right), \quad (i = 1, \ldots, n_w) \tag{2.70}$$

gives the $\boldsymbol{y}_{w_i}$ axis in the body frame when $\alpha_{w_i} = 0$. We may now construct $\mathbf{R}_{w_i}^b$ as

$$\mathbf{R}_{w_i}^b = \begin{bmatrix} \boldsymbol{x}_{w_i}^b & \boldsymbol{y}_{w_i}^b & (\boldsymbol{x}_{w_i}^b)^\times \boldsymbol{y}_{w_i}^b \end{bmatrix} \tag{2.71}$$

to be applied in Eq. (2.68). Similarly, we define a matrix

$$\mathbf{P}_w = \begin{bmatrix} r_w & 0 & -r_w & 0 \\ 0 & r_w & 0 & -r_w \\ 0 & 0 & 0 & 0 \end{bmatrix} \tag{2.72}$$

in which the wheels are assumed to be at an equal distance, r_w, from the origin of the body frame. We may now state the position of the center of mass of wheel i in the body frame as

$$\boldsymbol{p}_{w_i}^b = \mathrm{col}_i\left(\mathbf{P}_w\right) + \boldsymbol{c}_{w_i}^b, \quad (i = 1, \ldots, n_w) \tag{2.73}$$

Eq. (2.65) may now be applied to compute $\boldsymbol{\tau}_s^b$. A consequence of including static imbalance in the satellite's model is that the vector of n_w wheel angles, $\boldsymbol{\alpha}_{w_i}$, must be included in numerical simulation.

2.7.4 Thrusters for Reaction Wheel desaturation

As was explained in Section 2.5.2, thrusters will be utilized for desaturation of the RW array. "On/off" thrusters are considered, meaning that the thrusters may only produce a constant force, f_t, when switched on. To realize some torque in the body frame, $\boldsymbol{\tau}_t^b$, the Pulse Width Modulator (PWM) in [33] may be utilized to find suitable thruster on/off switching times. However, the NMPC desaturation scheme described in Section 4.3 requires $\boldsymbol{\tau}_t^b$ to be determined ahead of the maneuver. Thus, we will model thrusters only by their equivalent torque in the body frame, $\boldsymbol{\tau}_t^b$.

2.8 Complete satellite model

This section gives the completed satellite model. We define the set of states, $\boldsymbol{x}$, and the set of inputs, $\boldsymbol{u}$, as

$$\boldsymbol{x} = \begin{bmatrix} \mathbf{q} & \boldsymbol{\alpha}_w^w & \boldsymbol{\eta} & \boldsymbol{\omega}_{ob}^b & \boldsymbol{\eta}_d & \boldsymbol{\omega}_{bw}^w \end{bmatrix}^\top, \quad \boldsymbol{u} = \boldsymbol{\tau}_w^w \tag{2.74}$$

where $\boldsymbol{\eta}_d = \dot{\boldsymbol{\eta}}$ is defined for notational clarity. We may now state the dynamics as a nonlinear ODE by combining Eq. (2.6), Eq. (2.12), Eq. (2.51), Eq. (2.58) and Eq. (2.61):

$$\dot{\mathbf{q}} = \frac{1}{2}\boldsymbol{\Xi}(\mathbf{q})\boldsymbol{\omega}_{ob}^b \tag{2.75a}$$

$$\dot{\boldsymbol{\alpha}}_w^w = \boldsymbol{\omega}_{bw}^w \tag{2.75b}$$

$$\dot{\boldsymbol{\eta}} = \boldsymbol{\eta}_d \tag{2.75c}$$

$$\begin{bmatrix} \mathbf{M}_{11}(\boldsymbol{\eta}) & \mathbf{M}_{12} & \mathbf{L}_w^b\mathbf{J}_w \\ \mathbf{M}_{21} & \mathbf{M}_{22} & 0 \\ \mathbf{J}_w^\top\mathbf{L}_w^{b\top} & 0 & \mathbf{J}_w \end{bmatrix} \begin{bmatrix} \dot{\boldsymbol{\omega}}_{ob}^b \\ \dot{\boldsymbol{\eta}}_d \\ \dot{\boldsymbol{\omega}}_{bw}^w \end{bmatrix} = \tag{2.75d}$$

$$\begin{bmatrix} \left(\mathbf{M}_{11}(\boldsymbol{\eta})\boldsymbol{\omega}_{ob}^b + \mathbf{L}_w^b\mathbf{J}_w\boldsymbol{\omega}_{bw}^b\right)^\times \boldsymbol{\omega}_{ob}^b - \dot{\mathbf{M}}_{11}(\boldsymbol{\eta},\boldsymbol{\eta}_d)\boldsymbol{\omega}_{ob}^b + \mathbf{M}_\partial(\boldsymbol{\omega}_{ob}^b,\boldsymbol{\eta},\boldsymbol{\eta}_d) + \boldsymbol{\tau}_{gg}^b + \boldsymbol{\tau}_t^b + \boldsymbol{\tau}_s^b \\ -\mathbf{C}_{22}\boldsymbol{\eta}_d - \mathbf{K}_{22}\boldsymbol{\eta} \\ \boldsymbol{\tau}_w^w \end{bmatrix}$$

By inverting the leftmost in matrix in Eq. (2.75d), we obtain an ODE on the form $\dot{\boldsymbol{x}} = f(\boldsymbol{x},\boldsymbol{u})$. For four RWs and six assumed flexible modes, $\boldsymbol{x}$ contains 27 states.

$\mathbf{q}$	Quaternion, $(\cdot)^b$to $(\cdot)^o$	$\boldsymbol{\omega}_{ob}^b$	Angular velocity, $(\cdot)^b$to $(\cdot)^o$
$\boldsymbol{\Xi}(\mathbf{q})$	Defined by Eq. (2.12)	$\boldsymbol{\eta}$	Modal amplitudes, Eq. (2.21)
$\boldsymbol{\alpha}_w^w$	Vector of wheel angles	$\boldsymbol{\eta}_d$	Time-derivative of $\boldsymbol{\eta}$
$\boldsymbol{\omega}_{bw}^w$	Vector of wheel velocities	$\mathbf{M}_{11}(\boldsymbol{\eta})$	Defined by Eq. (2.39)
$\mathbf{J}_w$	Matrix of wheel inertias	$\mathbf{M}_{12} = \mathbf{M}_{21}^\top$	Defined by Eq. (2.42)
$\mathbf{L}_w^b$	Distribution matrix, Eq. (2.63)	$\mathbf{M}_{22}$	Defined by Eq. (2.43)
$\boldsymbol{\tau}_{gg}^b$	Gravity gradient, Eq. (2.6)	$\dot{\mathbf{M}}_{11}(\boldsymbol{\eta},\boldsymbol{\eta}_d)$	Defined by Eq. (2.53)
$\boldsymbol{\tau}_t^b$	Thruster torque	$\mathbf{M}_\partial(\boldsymbol{\omega}_{ob}^b,\boldsymbol{\eta},\boldsymbol{\eta}_d)$	Defined by Eq. (2.54)
$\boldsymbol{\tau}_s^b$	Static imbalance, Eq. (2.65)	$\mathbf{C}_{22}$	Nonzero part of $\mathbf{C}$, Eq. (2.50)
$\boldsymbol{\tau}_w^w$	Wheel torques	$\mathbf{K}_{22}$	Nonzero part of $\mathbf{K}$, Eq. (2.47)

Table 2.3: A summary of the notation relevant to Eq. (2.75)

Chapter 3

Control scheme, theory

This section provides brief theoretical introductions to the two main components of the proposed control scheme: Nonlinear Model Predictive Control (NMPC) and the Extended Kalman Filter (EKF). Section 3.1.1 and Section 3.1.2 are largely similar to the corresponding sections in [1], with minor modifications for clarity.

3.1 Nonlinear Model Predictive Control (NMPC)

3.1.1 Fundamentals

Model Predictive Control (MPC) is a control scheme that produces control inputs, $\boldsymbol{u}$, by minimizing some *penalty function*, $\boldsymbol{L}$, with respect to the dynamics of a *prediction model*. The problem may be formulated as an Optimal Control Problem (OCP), here with a prediction model on ODE form:

$$\begin{aligned} \min \quad & \boldsymbol{L}(\boldsymbol{x}(\cdot), \boldsymbol{u}(\cdot), \boldsymbol{p}) \\ \text{s.t.} \quad & \dot{\boldsymbol{x}}(t) = \boldsymbol{F}(\boldsymbol{x}(t), \boldsymbol{u}(t), \boldsymbol{p}) \\ & \boldsymbol{h}(\boldsymbol{x}(t), \boldsymbol{u}(t), \boldsymbol{p}) \leq 0 \\ & \boldsymbol{x}(t_0) = \boldsymbol{x}_{init} \end{aligned} \tag{3.1}$$

$\boldsymbol{x}$, $\boldsymbol{F}$, and $\boldsymbol{h}$ are the states, dynamics, and constraints of the system, respectively. $\boldsymbol{p}$ is a vector of parameters that could be used in the definition of $\boldsymbol{L}$, $\boldsymbol{F}$, and $\boldsymbol{h}$. Nonlinear Model Predictive Control (NMPC) is a special case of MPC with nonlinear $\boldsymbol{F}$. Since Eq. (3.1) must be solved in real-time, only a *prediction horizon* up to $t = T$ is considered. Furthermore, the inputs are discretized over some time grid $t_0, \ldots, t_N$, where N is the number of discrete inputs to be applied within the horizon. As in [53], the approach may roughly be broken down into four steps:

1. Initialize the *prediction model* with a state vector $\boldsymbol{x}_{init}$.
2. Minimize $\boldsymbol{L}$ by predicting system dynamics and optimizing over the N inputs.
3. Implement the first control input, $\boldsymbol{u}_0$, at the real system.
4. Move the prediction horizon one step forward and repeat.

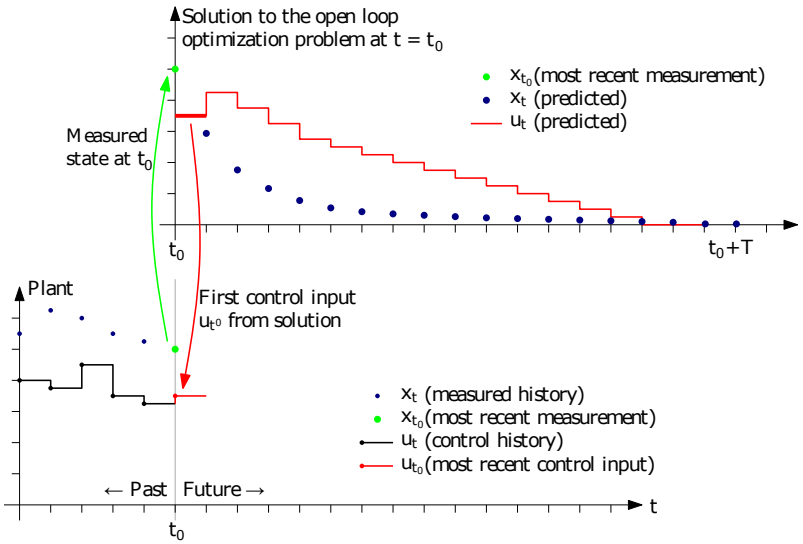

Figure 3.1: The working principle of MPC: $\boldsymbol{u}_0$ from the solution of the OCP (above) is applied to the real system (below). Figure adapted from [54].

The scheme is visualized in Fig. 3.1, in which the lower graph represents the real system and the upper graph represents the solution of Eq. (3.1) at time t_0.

3.1.2 Discretizing the Optimal Control Problem (OCP)

We may address the OCP in Eq. (3.1) by transforming it into a Nonlinear Program (NLP), which is then solved by utilizing a dedicated optimization solver [55]. A NLP may be stated as

$$\begin{aligned} \min_{\boldsymbol{w}} \quad & \boldsymbol{\Phi}(\boldsymbol{w},\boldsymbol{p}) \\ \text{s.t.} \quad & \boldsymbol{g}(\boldsymbol{w},\boldsymbol{p}) = 0 \\ & \boldsymbol{h}(\boldsymbol{w},\boldsymbol{p}) \leq 0 \end{aligned} \tag{3.2}$$

$\boldsymbol{\Phi}$ is the penalty function, $\boldsymbol{g}$ are equality constraints, $\boldsymbol{h}$ are inequality constraints, $\boldsymbol{p}$ are parameters, and $\boldsymbol{w}$ is a set of discrete decision variables. To obtain a finite-dimensional NLP from the continuous-time OCP we must discretize the system dynamics. The discretization schemes used in this context are known as *shooting methods*.

One such shooting method is that of direct single shooting. In single shooting, we define the set of inputs

$$\boldsymbol{w} = \{\boldsymbol{u}_0, \cdots, \boldsymbol{u}_{N-1}\} \tag{3.3}$$

and regard the system dynamics as a function of $\boldsymbol{w}$, $\boldsymbol{p}$, $\boldsymbol{x}_{init}$ and time:

$$\boldsymbol{x}_i = \boldsymbol{f}(\boldsymbol{w},\boldsymbol{p},\boldsymbol{x}_{init},t_i) \tag{3.4}$$

The function $\boldsymbol{f}$ is obtained through forward integration, such as with Runge-Kutta methods, of the dynamics from $\boldsymbol{x}_{init}$. Evaluating the path constraints at the same time grid defined for the inputs, we obtain the following NLP:

$$\begin{aligned} \min_{\boldsymbol{w}} \quad & \boldsymbol{\Phi}(\boldsymbol{f}(\boldsymbol{w},\boldsymbol{p},\boldsymbol{x}_{init},\cdot),\boldsymbol{w}) \\ \text{s.t.} \quad & \boldsymbol{h}(\boldsymbol{f}(\boldsymbol{w},\boldsymbol{p},\boldsymbol{x}_{init},t_i),\boldsymbol{w}_i,t_i) \leq 0, \quad i=0,\ldots,N-1 \end{aligned} \tag{3.5}$$

If the underlying system dynamics, $\boldsymbol{F}$, are nonlinear or unstable, the function $\boldsymbol{f}$ may become highly nonlinear as the length of the horizon, T, increases. Consequently, the trajectory's accuracy may depend heavily on the initial state, $\boldsymbol{x}_{init}$. Since the NMPC scheme utilizes an imperfect prediction model, $\boldsymbol{f}$ may fail to sufficiently capture the dynamics of the real system well as t progresses. The issue is known as nonlinearity propagation [53].

To reduce nonlinearity propagation, the direct multiple shooting method may be utilized [53]. To avoid long integration of dynamics, multiple shooting integrates the dynamics in a piece-wise fashion. The integration is typically performed on the same time grid chosen for the $\boldsymbol{u}_i$. The resulting piece-wise state trajectories are "stitched" together through constraints in the NLP.

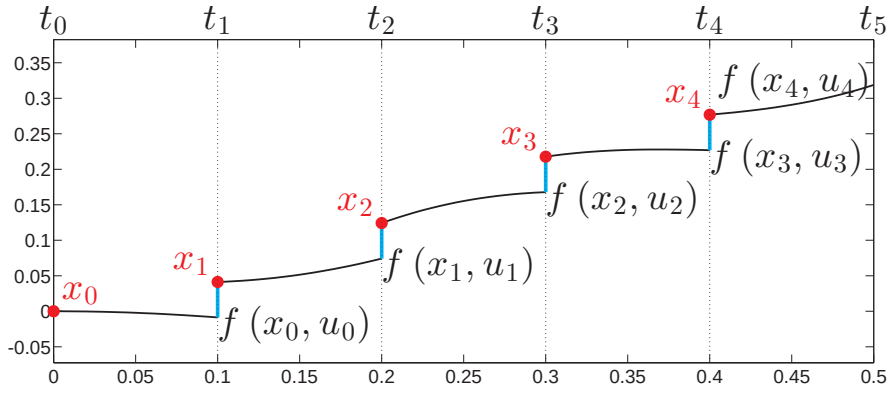

Figure 3.2: An illustration of the direct multiple shooting approach. Decision variables are shown in red, and integrated trajectories are shown in black. The differences between the two, shooting gaps, are shown in blue. Figure adapted from [56].

In multiple shooting, $\boldsymbol{f}$ only integrates the system from time-step t_i to t_{i+1}. As in Fig. 3.2, we denote the value of this function at t_{i+1} as $\boldsymbol{f}(\boldsymbol{x}_i,\boldsymbol{u}_i,\boldsymbol{p})$. Furthermore, we define the $N+1$ decision variables $\boldsymbol{x}_i$, which act as initial states for each piece-wise trajectory. The difference between some $\boldsymbol{x}_{i+1}$ and $\boldsymbol{f}(\boldsymbol{x}_i,\boldsymbol{u}_i,\boldsymbol{p})$, in blue in Fig. 3.2, are referred to as shooting gaps. We obtain the following NLP by constraining the shooting gaps to zero:

$$\begin{aligned} \min_{\boldsymbol{w}} \quad & \boldsymbol{\Phi}(\boldsymbol{w},\boldsymbol{p}) \\ \text{s.t.} \quad & \boldsymbol{f}(\boldsymbol{x}_i,\boldsymbol{u}_i,\boldsymbol{p}) - \boldsymbol{x}_{i+1} = 0, \quad i = 0,\dots,N-1 \\ & \boldsymbol{h}(\boldsymbol{x}_i,\boldsymbol{u}_i,\boldsymbol{p}) \leq 0, \quad i = 0,\dots,N \\ & \boldsymbol{x}_0 = \boldsymbol{x}_{init} \end{aligned} \tag{3.6}$$

in which

$$\boldsymbol{w} = \{\boldsymbol{x}_0, \boldsymbol{u}_0, \dots, \boldsymbol{x}_{N-1}, \boldsymbol{u}_{N-1}, \boldsymbol{x}_N\} \tag{3.7}$$

The control scheme proposed in this thesis will utilize the multiple shooting method.

3.1.3 Solving Nonlinear Programs (NLPs)

The two main approaches to solving NLPs are Sequential Quadratic Programming (SQP) methods and Interior Point (IP) methods [53]. This thesis will use utilize an IP method, specifically IPOPT [57]. To grasp the fundamentals of IP methods, we will briefly introduce the Karush–Kuhn–Tucker (KKT) conditions and how IP methods attempt to handle their non-smoothness. The purpose of this section is not to give a comprehensive overview of the field of numerical optimization. For that, we refer to [55].

Both SQP and IP methods aim to find a $\boldsymbol{w}$ that satisfies the necessary conditions for a local optimum: the KKT conditions. We note that all KKT points are not local optima. Rather, if $\boldsymbol{\Phi}$, $\boldsymbol{g}$ and $\boldsymbol{h}$ are continuously differentiable, all regular local optima are KKT points. For more on regularity and sufficient conditions for optima, we refer the reader to [55]. The KKT conditions may be stated as

$$\text{Dual Feasibility:} \quad \nabla_{\boldsymbol{w}} \mathcal{L}(\boldsymbol{w},\boldsymbol{\mu},\boldsymbol{\lambda},\boldsymbol{p}) = 0, \quad \boldsymbol{\mu} \geq 0, \tag{3.8a}$$

$$\text{Primal Feasibility:} \quad \boldsymbol{g}(\boldsymbol{w},\boldsymbol{p}) = 0, \quad \boldsymbol{h}(\boldsymbol{w},\boldsymbol{p}) \leq 0, \tag{3.8b}$$

$$\text{Complementarity slackness:} \quad \boldsymbol{\mu}_i \boldsymbol{h}_i(\boldsymbol{w},\boldsymbol{p}) = 0, \forall\, i \tag{3.8c}$$

where

$$\mathcal{L} = \Phi(\boldsymbol{w},\boldsymbol{p}) + \boldsymbol{\lambda}^\top \boldsymbol{g}(\boldsymbol{w},\boldsymbol{p}) + \boldsymbol{\mu}^\top \boldsymbol{h}(\boldsymbol{w},\boldsymbol{p}) \tag{3.9}$$

and $\nabla_{\boldsymbol{w}} \mathcal{L}$ is the gradient of $\mathcal{L}$ with respect to $\boldsymbol{w}$. λ and μ are *Lagrange multipliers* for the equality and inequality constraints, respectively. We will limit our focus to μ, the Lagrange multipliers for the inequality constraints. The complementarity slackness condition, Eq. (3.8c), implies that μ must equal zero if a constraint function, $\boldsymbol{h}_i$, is nonzero. When $\boldsymbol{h}_i$ is zero and actively enforced in the sense that it directly limits an improvement in $\boldsymbol{w}$, μ must be positive by definition [55]. The takeaway is that the complementarity slackness condition is non-smooth. This limits the use of root-finding algorithms, such as Newton's method, in search of a $\boldsymbol{w}$ that satisfies the KKT conditions [53].

IP methods allow for the use of Newton's method in search of an optimal $\boldsymbol{w}$ by replacing the KKT conditions with a smooth approximation:

$$\begin{aligned} \text{Dual Feasibility:} \quad & \nabla_{\boldsymbol{w}} \mathcal{L}(\boldsymbol{w}, \boldsymbol{\mu}, \boldsymbol{\lambda}, \boldsymbol{p}) = 0, \quad \boldsymbol{\mu} \geq 0, && \text{(3.10a)} \\ \text{Primal Feasibility:} \quad & \boldsymbol{g}(\boldsymbol{w}, \boldsymbol{p}) = 0, \quad \boldsymbol{h}(\boldsymbol{w}, \boldsymbol{p}) \leq 0, && \text{(3.10b)} \\ \text{Complementarity slackness:} \quad & \boldsymbol{\mu}_i \boldsymbol{h}_i(\boldsymbol{w}, \boldsymbol{p}) + \tau = 0, \forall\, i && \text{(3.10c)} \end{aligned}$$

where $\tau > 0$ is a smoothing constant. For increasingly small τ, Eq. (3.10) more closely approximates Eq. (3.8). Typical for IP methods is to start the search for an optimal $\boldsymbol{w}$ with a large τ, and gradually decrease τ when approaching a solution [53]. However, if we initialize an IP solver with an optimal $\boldsymbol{w}$, the solver must still perform iterations to find a τ that is smaller than some predefined tolerance [58].

The approach of initializing a solver with a "good guess" of $\boldsymbol{w}$ is known as warm-starting and may be computationally beneficial when solving a series of related NLPs in real-time [53]. Because of the nature of the smoothing constant, warm-started IP methods may not be as efficient as warm-started SQP methods [53]. Nonetheless, IPOPT was used as a solver in this thesis because of its satisfactory performance, ease of use, and compatibility with CasADi.

3.2 Extended Kalman Filter

A state estimator may be utilized to estimate the state of a dynamic system in the presence of noisy measurements and disturbances. The Kalman Filter is one common choice for such an estimator. The Kalman Filter produces a state estimate by combining external real-time measurements with an internal prediction based on prior knowledge. The Kalman Filter produces the minimum mean square error estimate with linear system dynamics and under the assumption of Gaussian additive noises in measurements and disturbances [59]. The Extended Kalman Filter (EKF) is an extension of the Kalman Filter for nonlinear dynamics. Although it does not guarantee a minimum mean square error estimate, it is still commonly used in control applications [59].

The discrete-time EKF assumes the true state at time k, $\boldsymbol{x}_k$, and measurement, $\boldsymbol{z}_k$, to be given by

$$\begin{aligned} \boldsymbol{x}_k &= f(\boldsymbol{x}_{k-1}, \boldsymbol{u}_k) + \boldsymbol{w}_k \quad , \quad \boldsymbol{w}_k \sim \mathcal{N}\left(\boldsymbol{0}, \tilde{\mathbf{Q}}_k\right) \\ \boldsymbol{z}_k &= h(\boldsymbol{x}_k) + \boldsymbol{v}_k \quad , \quad \boldsymbol{v}_k \sim \mathcal{N}\left(\boldsymbol{0}, \tilde{\mathbf{R}}_k\right) \end{aligned} \tag{3.11}$$

f and h are differentiable and possibly nonlinear functions. $\boldsymbol{w}_k$ and $\boldsymbol{v}_k$ are process and observation noises assumed to be zero mean multivariate Gaussian noises with covariance $\tilde{\mathbf{Q}}_k$ and $\tilde{\mathbf{R}}_k$. In practice, the true system's f and h are not perfectly known. Instead, an approximate model is used.

The EKF algorithm consists of two distinct steps, named the prediction and update steps. We may state the corresponding equations as in [59]:

$$\textbf{Predict} \quad \begin{cases} \text{Predicted state estimate} & \hat{\boldsymbol{x}}_{k|k-1} = f(\hat{\boldsymbol{x}}_{k-1|k-1}, \boldsymbol{u}_k) \\ \text{Predicted covariance estimate} & \mathbf{P}_{k|k-1} = \mathbf{F}_k \mathbf{P}_{k-1|k-1} \mathbf{F}_k^\top + \tilde{\mathbf{Q}}_k \end{cases} \tag{3.12}$$

$$\textbf{Update} \quad \begin{cases} \text{Innovation residual} & \boldsymbol{y}_k = \boldsymbol{z}_k - h(\hat{\boldsymbol{x}}_{k|k-1}) \\ \text{Innovation covariance} & \mathbf{S}_k = \mathbf{H}_k \mathbf{P}_{k|k-1} \mathbf{H}_k^\top + \tilde{\mathbf{R}}_k \\ \text{Kalman gain} & \mathbf{K}_k = \mathbf{P}_{k|k-1} \mathbf{H}_k^\top \mathbf{S}_k^{-1} \\ \text{Updated state estimate} & \hat{\boldsymbol{x}}_{k|k} = \hat{\boldsymbol{x}}_{k|k-1} + \mathbf{K}_k \boldsymbol{y}_k \\ \text{Updated covariance estimate} & \mathbf{P}_{k|k} = (\mathbf{I} - \mathbf{K}_k \mathbf{H}_k) \mathbf{P}_{k|k-1} \end{cases} \tag{3.13}$$

where

$$\mathbf{F}_k = \left. \frac{\partial f}{\partial \boldsymbol{x}} \right|_{\hat{\boldsymbol{x}}_{k-1|k-1}, \boldsymbol{u}_k}, \quad \mathbf{H}_k = \left. \frac{\partial h}{\partial \boldsymbol{x}} \right|_{\hat{\boldsymbol{x}}_{k|k-1}} \tag{3.14}$$

In the prediction step, Eq. (3.12), f is used to predict the state estimate $\hat{\boldsymbol{x}}_{k|k-1}$ ($\hat{\boldsymbol{x}}$ at time k given its estimate at time $k-1$). Likewise, the covariance of $\hat{\boldsymbol{x}}$, denoted $\mathbf{P}$, is predicted by computing the jacobian of f at the current state such that the corresponding linear Kalman Filter equation may be applied.

The update step, Eq. (3.13), incorporates the measurement $\boldsymbol{z}_k$. The innovation, $\boldsymbol{y}_k$, is computed as the difference between the measurement and the observation function at the predicted state, $h(\hat{\boldsymbol{x}}_{k|k-1})$. Similarly to the prediction step, the jacobian of h at the predicted state estimate is used to compute the innovation covariance. The Kalman gain, $\mathbf{K}$, is used to weigh the relative importance of the measurement to the predicted state estimate in the updated state estimate, $\hat{\boldsymbol{x}}_{k|k}$. $\mathbf{P}$ is also updated, such that it may be used in the next prediction step.

Chapter 4

Controller design

In this section, we utilize the theory presented in Chapter 3 to design the NMPC+EKF control scheme for the specific model presented in Chapter 2.

4.1 Prediction model design

A crucial step in designing a NMPC scheme is that of choosing a suitable prediction model. For comparison, we will again state the part of the complete satellite dynamics most relevant to this section, Eq. (2.75d). See Table 2.3 for notation.

$$\begin{aligned}\mathbf{M}_{11}(\boldsymbol{\eta})\dot{\boldsymbol{\omega}}_{ob}^{b} &= -\mathbf{M}_{12}\ddot{\boldsymbol{\eta}} - \mathbf{L}_{w}^{b}\mathbf{J}_{w}\dot{\boldsymbol{\omega}}_{bw}^{w} + \left(\mathbf{M}_{11}(\boldsymbol{\eta})\boldsymbol{\omega}_{ob}^{b} + \mathbf{L}_{w}^{b}\mathbf{J}_{w}\boldsymbol{\omega}_{bw}^{b}\right)^{\times}\boldsymbol{\omega}_{ob}^{b} \\ &\quad - \dot{\mathbf{M}}_{11}(\boldsymbol{\eta},\dot{\boldsymbol{\eta}})\,\boldsymbol{\omega}_{ob}^{b} + \mathbf{M}_{\partial}(\boldsymbol{\omega}_{ob}^{b},\boldsymbol{\eta},\dot{\boldsymbol{\eta}}) + \boldsymbol{\tau}_{gg}^{b} + \boldsymbol{\tau}_{t}^{b} + \boldsymbol{\tau}_{s}^{b} \qquad (4.1a)\\ \mathbf{M}_{22}\ddot{\boldsymbol{\eta}} &= -\mathbf{M}_{21}\dot{\boldsymbol{\omega}}_{ob}^{b} - \mathbf{C}_{22}\dot{\boldsymbol{\eta}} - \mathbf{K}_{22}\boldsymbol{\eta} \qquad (4.1b)\\ \mathbf{J}_{w}\dot{\boldsymbol{\omega}}_{bw}^{w} &= -\mathbf{J}_{w}^{\top}\mathbf{L}_{w}^{b\top}\dot{\boldsymbol{\omega}}_{ob}^{b} + \boldsymbol{\tau}_{w}^{w} \qquad (4.1c)\end{aligned}$$

Utilizing Eq. (4.1) as a prediction immediately presents two issues. One is that the high nonlinearity of the system presents a substantial computational cost, as shown in [1]. Furthermore, with the prediction model equal to the simulation model, we are not subjecting the control scheme to modeling errors that would be present in a physical system. Some mismatch between the simulation model and NMPC prediction model is therefore desirable. For this reason, the gravity gradient, $\boldsymbol{\tau}_{gg}^{b}$, and the static imbalance, $\boldsymbol{\tau}_{s}^{b}$ are to be regarded as disturbances in this thesis, and will not be eligible for use in the prediction model.

[1] proposed to simplify Eq. (4.1) by neglecting nonlinearities in $\boldsymbol{\eta}$ and $\boldsymbol{\eta}_{d}$, and reducing the number of assumed modes, n_{m}. Though the model in [1] was somewhat less comprehensive, the equivalent for Eq. (4.1) would be:

$$\begin{aligned}\bar{\mathbf{M}}_{11}\dot{\boldsymbol{\omega}}_{ob}^{b} &= -\mathbf{M}_{12}\ddot{\boldsymbol{\eta}} - \mathbf{L}_{w}^{b}\mathbf{J}_{w}\dot{\boldsymbol{\omega}}_{bw}^{w} + \left(\bar{\mathbf{M}}_{11}\boldsymbol{\omega}_{ob}^{b} + \mathbf{L}_{w}^{b}\mathbf{J}_{w}\boldsymbol{\omega}_{bw}^{b}\right)^{\times}\boldsymbol{\omega}_{ob}^{b} + \boldsymbol{\tau}_{t}^{b} \qquad (4.2a)\\ \mathbf{M}_{21}\dot{\boldsymbol{\omega}}_{ob}^{b} &= -\mathbf{M}_{22}\ddot{\boldsymbol{\eta}} - \mathbf{C}_{22}\dot{\boldsymbol{\eta}} - \mathbf{K}_{22}\boldsymbol{\eta} \qquad (4.2b)\\ \mathbf{J}_{w}\dot{\boldsymbol{\omega}}_{bw}^{w} &= -\mathbf{J}_{w}^{\top}\mathbf{L}_{w}^{b\top}\dot{\boldsymbol{\omega}}_{ob}^{b} + \boldsymbol{\tau}_{w}^{w} \qquad (4.2c)\end{aligned}$$

in which $\bar{\mathbf{M}}_{11} = \mathbf{M}_{11}(\mathbf{0})$. In [1], an NMPC scheme with a prediction model similar to Eq. (4.2) was shown to be much less computationally demanding than that of the full nonlinear model, without significant loss in performance.

However, Eq. (4.2) may not be successfully deployed as a prediction model for a physical system. That is because of the lack of directly available measurement of assumed modal amplitudes, $\boldsymbol{\eta}$, as they have little physical meaning [60]. We instead propose to use a prediction model where flexible displacement is represented by driven harmonic oscillators.

$$\textbf{PM1} \quad \begin{cases} \bar{\mathbf{J}}\dot{\boldsymbol{\omega}}_{ob}^{b} & = -\mathbf{B}\ddot{\boldsymbol{\sigma}} - \mathbf{L}_w^b \mathbf{J}_w \dot{\boldsymbol{\omega}}_{bw}^{b} + \left(\bar{\mathbf{J}}\boldsymbol{\omega}_{ob}^{b} + \mathbf{L}_w^b \mathbf{J}_w \boldsymbol{\omega}_{bw}^{b}\right)^{\times} \boldsymbol{\omega}_{ob}^{b} + \boldsymbol{\tau}_t^b \\ \ddot{\boldsymbol{\sigma}} & = -\mathbf{B}^{\top}\dot{\boldsymbol{\omega}}_{ob}^{b} - 2\boldsymbol{\xi}\boldsymbol{\Omega}\dot{\boldsymbol{\sigma}} - \boldsymbol{\Omega}^2\boldsymbol{\sigma} \\ \mathbf{J}_w\dot{\boldsymbol{\omega}}_{bw}^{w} & = -\mathbf{J}_w^{\top}\mathbf{L}_w^{b\top}\dot{\boldsymbol{\omega}}_{ob}^{b} + \boldsymbol{\tau}_w^w \\ \dot{\mathbf{q}} & = \tfrac{1}{2}\boldsymbol{\Xi}(\mathbf{q})\boldsymbol{\omega}_{ob}^{b} \end{cases} \tag{4.3}$$

For easy reference, we will refer to this specific prediction model as **PM1** . The dynamics of $\dot{\mathbf{q}}$ are included for completeness. The oscillator displacement, $\boldsymbol{\sigma}$, is regarded as a virtual, nonphysical state. $\mathbf{B}$ represents the "effect" of $\boldsymbol{\sigma}$ on the satellite, $\boldsymbol{\xi}$ is the oscillator's damping ratio, and $\boldsymbol{\Omega}$ is the oscillator's natural frequency. $\bar{\mathbf{J}}$ is the altered inertia matrix that includes the constant part of $\mathbf{M}_{11}$ as in Eq. (2.39):

$$\bar{\mathbf{J}} = \mathbf{J}_b + \begin{bmatrix} 2\rho\int_0^L (s+\ell)^2\,ds & 0 & 0 \\ 0 & 0 & 0 \\ 0 & 0 & 2\rho\int_0^L (s+\ell)^2\,ds \end{bmatrix} \tag{4.4}$$

For low computational complexity, a single oscillator is desirable. For multiple oscillators, $\boldsymbol{\xi}$ and $\boldsymbol{\Omega}$ are diagonal matrices.

$\mathbf{B}$, $\boldsymbol{\xi}$ and $\boldsymbol{\Omega}$ are parameters to be selected in the control design. How the three parameters shape the response of the oscillator is perhaps best explained through the Bode plots in Fig. 4.1.

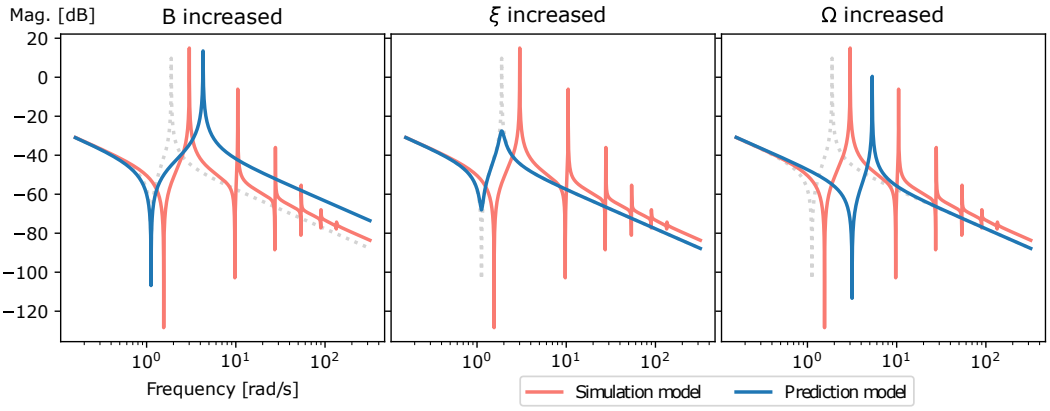

Figure 4.1: Bode plots from the first RW to ω about $\boldsymbol{x}^b$. The grey dotted line serves as a baseline from which $\mathbf{B}$ is increased (left), $\boldsymbol{\xi}$ is decreased (middle), $\boldsymbol{\Omega}$ is increased (right).

In Fig. 4.1, the frequency response of a simulation model with six assumed modes, resulting in six distinct resonant peaks, is shown in orange. The specific parameters of the simulation model are not important in this context. The grey dotted line is the frequency response of a single oscillator for some choice of $\mathbf{B}$, $\boldsymbol{\xi}$, and $\boldsymbol{\Omega}$. The blue lines show how the frequency response changes for each oscillator parameter. Increasing $\mathbf{B}$ gives a resonant peak at a higher frequency and increases the response for higher frequencies. Decreasing $\boldsymbol{\xi}$ gives a reduced response for both anti-resonant and resonant peaks. Increasing $\boldsymbol{\Omega}$ shifts both peaks to a higher frequency.

PM1 still contains fairly complex dynamics, particularly in relation to the RWs. In Section 5.6, we will analyze the potential improvements in performance and computational of simplifying **PM1**. We define **PM2** as the prediction model in which $\dot{\boldsymbol{\omega}}_{bw}^{w}$ is decoupled from $\dot{\boldsymbol{\omega}}_{ob}^{b}$:

$$\textbf{PM2} \quad \begin{cases} \bar{\mathbf{J}}\dot{\boldsymbol{\omega}}_{ob}^{b} & = -\mathbf{B}\ddot{\boldsymbol{\sigma}} - \mathbf{L}_{w}^{b}\boldsymbol{\tau}_{w}^{w} + \left(\bar{\mathbf{J}}\boldsymbol{\omega}_{ob}^{b} + \mathbf{L}_{w}^{b}\mathbf{J}_{w}\boldsymbol{\omega}_{bw}^{b}\right)^{\times}\boldsymbol{\omega}_{ob}^{b} + \boldsymbol{\tau}_{t}^{b} \\ \ddot{\boldsymbol{\sigma}} & = -\mathbf{B}^{\top}\dot{\boldsymbol{\omega}}_{ob}^{b} - 2\boldsymbol{\xi}\boldsymbol{\Omega}\dot{\boldsymbol{\sigma}} - \boldsymbol{\Omega}^{2}\boldsymbol{\sigma} \\ \mathbf{J}_{w}\dot{\boldsymbol{\omega}}_{bw}^{w} & = \boldsymbol{\tau}_{w}^{w} \\ \dot{\mathbf{q}} & = \frac{1}{2}\boldsymbol{\Xi}(\mathbf{q})\boldsymbol{\omega}_{ob}^{b} \end{cases} \tag{4.5}$$

Furthermore, we define **PM3** as a simplification of **PM2** in which the RW gyroscopic effect is neglected:

$$\textbf{PM3} \quad \begin{cases} \bar{\mathbf{J}}\dot{\boldsymbol{\omega}}_{ob}^{b} & = -\mathbf{B}\ddot{\boldsymbol{\sigma}} - \mathbf{L}_{w}^{b}\boldsymbol{\tau}_{w}^{w} + \left(\bar{\mathbf{J}}\boldsymbol{\omega}_{ob}^{b}\right)^{\times}\boldsymbol{\omega}_{ob}^{b} + \boldsymbol{\tau}_{t}^{b} \\ \ddot{\boldsymbol{\sigma}} & = -\mathbf{B}^{\top}\dot{\boldsymbol{\omega}}_{ob}^{b} - 2\boldsymbol{\xi}\boldsymbol{\Omega}\dot{\boldsymbol{\sigma}} - \boldsymbol{\Omega}^{2}\boldsymbol{\sigma} \\ \mathbf{J}_{w}\dot{\boldsymbol{\omega}}_{bw}^{w} & = \boldsymbol{\tau}_{w}^{w} \\ \dot{\mathbf{q}} & = \frac{1}{2}\boldsymbol{\Xi}(\mathbf{q})\boldsymbol{\omega}_{ob}^{b} \end{cases} \tag{4.6}$$

4.2 Initializing $\boldsymbol{\sigma}$ with the Extended Kalman Filter

As was mentioned in Section 4.1, the assumed modal amplitudes, $\boldsymbol{\eta}$, lack physical meaning. We will, therefore, not use measurements of $\boldsymbol{\eta}$ or $\dot{\boldsymbol{\eta}}$ to determine the current state of the flexible panels in this thesis. One could attempt to determine the state of the panels through measurements from piezoelectrics or accelerometers attached to the panels [16]. We instead attempt to extract the torque produced on the spacecraft by the panels from a measurement of $\dot{\boldsymbol{\omega}}_{ob}^{b}$. This quantity is then used to form a measurement from which the Extended Kalman Filter (EKF) may estimate suitable values of $\boldsymbol{\sigma}$ and $\dot{\boldsymbol{\sigma}}$. The resulting $\boldsymbol{\sigma}$ and $\dot{\boldsymbol{\sigma}}$ are to be used as starting conditions in the NMPC scheme. $\mathbf{q}$, $\boldsymbol{\omega}_{ob}^{b}$ and $\boldsymbol{\omega}_{bw}^{w}$ are assumed to be perfectly known and will not be estimated by the EKF.

We now assume that the complete satellite dynamics, Eq. (2.75), are unknown and that **PM1**, Eq. (4.3), is instead our best available model. By rewriting Eq. (4.3), we have

$$\mathbf{B}\ddot{\boldsymbol{\sigma}} = -\bar{\mathbf{J}}\dot{\boldsymbol{\omega}}_{ob}^{b} + \mathbf{L}_{w}^{b}(\mathbf{J}_{w}^{\top}\mathbf{L}_{w}^{b^{\top}}\dot{\boldsymbol{\omega}}_{ob}^{b} - \boldsymbol{\tau}_{w}^{w}) + \left(\bar{\mathbf{J}}\boldsymbol{\omega}_{ob}^{b} + \mathbf{L}_{w}^{b}\mathbf{J}_{w}\boldsymbol{\omega}_{bw}^{b}\right)^{\times}\boldsymbol{\omega}_{ob}^{b} + \boldsymbol{\tau}_{t}^{b} \tag{4.7}$$

$\mathbf{B}\ddot{\boldsymbol{\sigma}}$ represents the virtual torque produced by the oscillator on the satellite. We note that the right-hand side of Eq. (4.7) includes only measurable states. Furthermore, we

premultiply the second equation in Eq. (4.3) by $\mathbf{B}$ to obtain

$$\mathbf{B}\ddot{\boldsymbol{\sigma}} = -\mathbf{B}\mathbf{B}^{\top}\dot{\boldsymbol{\omega}}_{ob}^{b} - \mathbf{B}(2\boldsymbol{\xi}\boldsymbol{\Omega}\dot{\boldsymbol{\sigma}} - \boldsymbol{\Omega}^{2}\boldsymbol{\sigma}) \tag{4.8}$$

We may now combine Eq. (4.7) and Eq. (4.8) to produce $\boldsymbol{z}$, the measurement, and $h(\boldsymbol{x})$, the observation function, as in Eq. (3.11) such that we may apply the EKF equations in Eq. (3.12) and Eq. (3.13).

$$\boldsymbol{z} = (\mathbf{B}\mathbf{B}^{\top} + \mathbf{L}_{w}^{b}\mathbf{J}_{w}^{\top}\mathbf{L}_{w}^{b^{\top}} - \bar{\mathbf{J}})\dot{\boldsymbol{\omega}}_{ob}^{b} - \mathbf{L}_{w}^{b}\boldsymbol{\tau}_{w}^{w} + \left(\bar{\mathbf{J}}\boldsymbol{\omega}_{ob}^{b} + \mathbf{L}_{w}^{b}\mathbf{J}_{w}\boldsymbol{\omega}_{bw}^{b}\right)^{\times}\boldsymbol{\omega}_{ob}^{b} + \boldsymbol{\tau}_{t}^{b} \tag{4.9a}$$

$$h(\boldsymbol{x}) = -\mathbf{B}(2\boldsymbol{\xi}\boldsymbol{\Omega}\dot{\boldsymbol{\sigma}} - \boldsymbol{\Omega}^{2}\boldsymbol{\sigma}) \tag{4.9b}$$

In the EKF, $h(\boldsymbol{x})$ is evaluated on the one-step-ahead state estimate as predicted by $f(\boldsymbol{x}, \boldsymbol{u})$, Eq. (3.11). In our case, $f(\cdot)$ is defined as a one-step forward integration of **PM1** by a RK-4 scheme.

Although $\boldsymbol{z}$ is evaluated on true state measurements, its expression is based on incomplete dynamics. The measurement based on complete knowledge of the model, $\boldsymbol{z}_{true}$, is instead stated as

$$\begin{aligned}\boldsymbol{z}_{true} = &\left(\mathbf{M}_{12}\mathbf{M}_{22}^{-1}\mathbf{M}_{21} + \mathbf{L}_{w}^{b}\mathbf{J}_{w}^{\top}\mathbf{L}_{w}^{b^{\top}} - \mathbf{M}_{11}(\boldsymbol{\eta})\right)\dot{\boldsymbol{\omega}}_{ob}^{b} - \mathbf{L}_{w}^{b}\boldsymbol{\tau}_{w}^{w} \\ &+ \left(\mathbf{M}_{11}(\boldsymbol{\eta})\boldsymbol{\omega}_{ob}^{b} + \mathbf{L}_{w}^{b}\mathbf{J}_{w}\boldsymbol{\omega}_{bw}^{b}\right)^{\times}\boldsymbol{\omega}_{ob}^{b} + \boldsymbol{\tau}_{gg}^{b} + \boldsymbol{\tau}_{t}^{b} + \boldsymbol{\tau}_{s}^{b}\end{aligned} \tag{4.10}$$

Therefore, $\boldsymbol{z}$ is not to be fully trusted. In terms of the EKF: $\tilde{\mathbf{R}}$ is nonzero. We may weigh the relative importance of the internal prediction to the external measurement by the covariance matrices, $\tilde{\mathbf{Q}}$ and $\tilde{\mathbf{R}}$ respectively. This process of tuning the EKF is covered in Section 5.3.

We will define three EKFs that differ in how their respective prediction models are treated:

- **EKF1**, which utilizes **PM1** with one harmonic oscillator. Parameters of the oscillator are found in Section 5.2.
- **EKF2**, which utilizes **PM1** with two harmonic oscillators. The resulting states corresponding to the second oscillator, σ_2 and $\dot{sigma}_2$ are discarded.
- **EKF3**, which utilizes **PM1** with two harmonic oscillators. The resulting σ_2 and $\dot{\sigma}_2$ are added to σ_1 and $\dot{\sigma}_1$ through some weighting factor to be decided in Section 5.3. E.g.: $\sigma_{init} = \sigma_1 + a\sigma_2$, where σ_{init} is the value passed to the NMPC, and a is some constant.

We also introduce notation to denote the specifics of any EKF. For example: **EKF1**($\boldsymbol{z}$, $\tilde{\mathbf{R}} = 2\text{e}4$) denotes **EKF1** using Eq. (4.9a) as measurement, with $\tilde{\mathbf{R}} = 2\text{e}4 \cdot \mathbf{I}_3$.

4.2.1 Notch filters

To be computationally feasible, the NMPC requires relatively low bandwidth, meaning large input discretization. This implies that the controller will not counter high-frequency disturbances efficiently [61]. The complete satellite model, Eq. (2.75), contains two effects that may be regarded as high-frequency disturbances. One is that of the RW static imbalance torque, which has a frequency equal to the wheel speed. The other is the panel vibration caused by higher-order modes, with frequencies dependent on the specific satellite structure. Starting from Section 5.5 we utilize notch filters, specifically on $\boldsymbol{z}$ and $\boldsymbol{\omega}_{ob}^{b}$, to avoid initializing the NMPC with state values containing undesirable high-frequency content.

A notch filter is a filter that attenuates frequencies within a narrow range. The process of combining multiple notch filters is known as convolution. Fig. 4.2 shows three convolved notch filters. Notch filters generally cause less phase lag than low-pass filters in a control loop [62]. The specific notch filter applied in this thesis is the second-order infinite-impulse-response (IIR) digital notch filter provided by SciPy, which is implemented as in [63].

The parameters required by this specific filter are the frequency to be filtered, ω_0, and the quality factor determining the filter's width. In this thesis, we will use a quality factor as in Fig. 4.2, equal to ω_0. The notch filters are applied to an array of the 100 most recent measurements. Whether or not a notch filter is applied, and to what ω_0, is stated clearly in the relevant sections in Chapter 5.

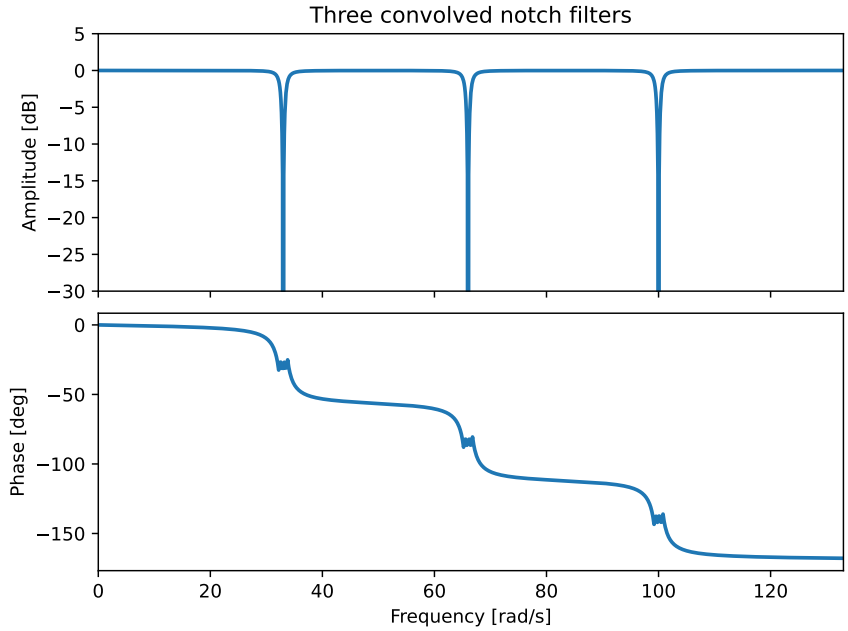

Figure 4.2: The amplitude and phase of three convolved Scipy IIR notch filters with quality factors equal to ω_0.

4.3 NMPC formulation

Unless explicitly stated otherwise, the NMPC formulation to be used throughout this thesis is Eq. (4.11), **NMPC1**.

$$\min_{\boldsymbol{x},\boldsymbol{\tau}_w^w} \quad \frac{1}{2}\|\boldsymbol{x}_N - \boldsymbol{x}_{ref}\|_{\boldsymbol{Q}_f}^2 + \sum_{i=0}^{N-1} \frac{1}{2}\|\boldsymbol{x}_i - \boldsymbol{x}_{ref}\|_{\boldsymbol{Q}}^2 + \frac{1}{2}\|\boldsymbol{\tau}_{w,i}^w\|_{\boldsymbol{R}}^2 \tag{4.11a}$$

NMPC1: s.t.

$$\boldsymbol{x}_0 = \boldsymbol{x}_{init} \tag{4.11b}$$

$$\boldsymbol{x}_{i+1} = \mathbf{PM}(\boldsymbol{x}_i, \boldsymbol{\tau}_{w,i}^w) \tag{4.11c}$$

$$|\boldsymbol{\tau}_{w,i}^w| \leq \boldsymbol{\tau}_{w,\,max}^w, \quad |\boldsymbol{\omega}_{bw,i}^w| \leq \boldsymbol{\omega}_{bw,\,max}^w \tag{4.11d}$$

$\boldsymbol{Q}$, $\boldsymbol{Q}_f$ and $\boldsymbol{R}$ are positive and diagonal weighting matrices. $\boldsymbol{x}_{ref}$ is the desired state vector. Eq. (4.11a) contains an abuse of notation, as the difference in quaternion is instead expressed using $\mathbf{q}$ from Eq. (2.13). **PM** denotes one of the prediction models defined in Section 4.1, and is discretized using multiple shooting as in Eq. (3.6). We utilize RK4 integration with ten subintervals per NMPC input. The two constraints, Eq. (4.11d), represent RW limits in terms of maximum torque and wheel speed.

Tuning of the weighting matrices $\boldsymbol{Q}$, $\boldsymbol{Q}_f$ and $\boldsymbol{R}$ was explored in [1]. In this thesis, we will use weights with diagonal elements given as in Table 4.1.

	$\mathbf{Q}$	$\mathbf{Q}_f$		$\mathbf{R}$
$\mathbf{q}$	1e0	1e2	$\boldsymbol{\tau}_w^w$	5e-4
$\boldsymbol{\omega}_{ob}^b$	5e0	1e1		
$\boldsymbol{\sigma}$	5e-1	1e4		
$\dot{\boldsymbol{\sigma}}$	5e-1	1e4		

Table 4.1: NMPC weights used throughout this thesis

We will warm-start the decision variables of all NMPC schemes throughout this thesis. See Section 3.1.3 for theoretical background. Given the decision variables $\boldsymbol{w}$ for the previous iteration, we discard the previous initial state and input. Furthermore, we replace the predicted state after one iteration with the new initial state as found by the EKF. Lastly, we duplicate the last set of decision variables.

For Section 5.5, we expand on Eq. (4.11) for the purposes of RW management. Namely, we will attempt to avoid convergence of $\boldsymbol{\omega}_{bw}^w$ to certain regions. The purpose is to avoid static imbalance torques that may interact or interfere with the dominant flexible modes. To achieve this, we define a term, Γ, to be appended to the NMPC penalty function.

$$\Gamma(\boldsymbol{x}_i, \boldsymbol{\omega}_\gamma) = \sum_{\gamma=1}^{n_\gamma}\sum_{j=1}^{n_w} a e^{-b(\omega_{j,i}-\omega_\gamma)^2}, \quad \Gamma(\boldsymbol{x}_N, \boldsymbol{\omega}_\gamma) = \sum_{\gamma=1}^{n_\gamma}\sum_{j=1}^{n_w} a_f e^{-b(\omega_{j,N}-\omega_\gamma)^2} \tag{4.12}$$

A similar penalty term is found in [64]. $\omega_{j,i}$ is the velocity of wheel j at time i. $\boldsymbol{\omega}_\gamma$ is a vector of n_γ wheel velocities to avoid. The value of Eq. (4.12) is near zero nearly

everywhere but with a peak centered on ω_γ. a and a_f are constants that determine the magnitude of peak at times i and time N, respectively. b determines the width of the peak. Fig. 4.3 shows Γ with $a =$ 1e-4, $b =$ 5e-2.

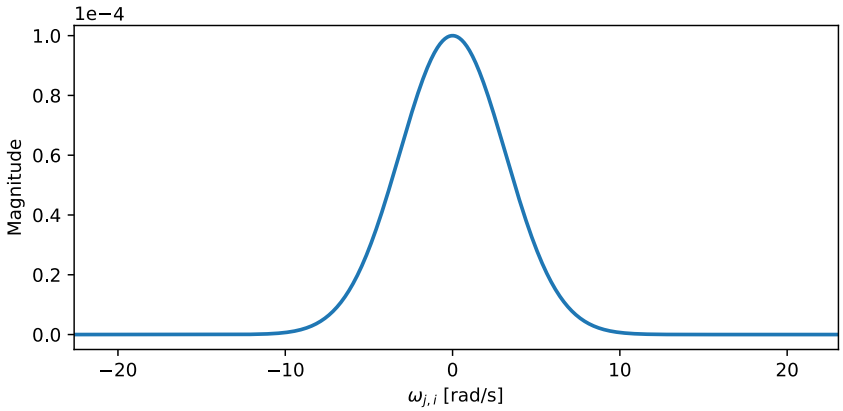

Figure 4.3: The Γ penalty term with $a =$ 1e-4, $b =$ 5e-2, $\omega_\gamma = 0$.

We now define Φ as the penalty function of Eq. (4.11)

$$\Phi(\boldsymbol{x}, \boldsymbol{\tau}_w^w) = \frac{1}{2}\|\boldsymbol{x}_N - \boldsymbol{x}_{ref}\|_{\boldsymbol{Q}_f}^2 + \sum_{i=0}^{N-1} \frac{1}{2}\|\boldsymbol{x}_i - \boldsymbol{x}_{ref}\|_{\boldsymbol{Q}}^2 + \frac{1}{2}\|\boldsymbol{\tau}_{w,i}^w\|_{\boldsymbol{R}}^2 \tag{4.13}$$

and state the RW management NMPC formulation, **NMPC2**, as

$$\min_{\boldsymbol{x}, \boldsymbol{\tau}_w^w} \quad \Phi(\boldsymbol{x}, \boldsymbol{\tau}_w^w) + \boldsymbol{\Gamma}(\boldsymbol{x}_N, \boldsymbol{\omega}_\gamma) + \sum_{i=1}^{N-1} \boldsymbol{\Gamma}(\boldsymbol{x}_i, \boldsymbol{\omega}_\gamma) \tag{4.14a}$$

NMPC2: s.t.

$$\boldsymbol{x}_0 = \boldsymbol{x}_{init} \tag{4.14b}$$

$$\boldsymbol{x}_{i+1} = \mathbf{PM}(\boldsymbol{x}_i, \boldsymbol{\tau}_{w,i}^w) \tag{4.14c}$$

$$|\boldsymbol{\tau}_{w,i}^w| \leq \boldsymbol{\tau}_{w,\,max}^w, \quad |\boldsymbol{\omega}_{bw,i}^w| \leq \boldsymbol{\omega}_{bw,\,max}^w \tag{4.14d}$$

Γ increases the nonlinearity of the NLP, which could potentially increase the difficulty of convergence. In Section 5.5, we will also investigate whether the addition of an explicit null space input component with a reduced penalty could make Γ simpler to navigate. We define the new decision variables, $u_{null,i}$, as in Eq. (2.64). We now state the NMPC with the null space component, **NMPC3**, as

$$\min_{\boldsymbol{x}, \boldsymbol{\tau}_w^w, \boldsymbol{u}_{null}} \quad \Phi(\boldsymbol{x}, \boldsymbol{\tau}_w^w) + \boldsymbol{\Lambda}(\boldsymbol{u}_{null}) + \boldsymbol{\Gamma}(\boldsymbol{x}_N, \boldsymbol{\omega}_\gamma) + \sum_{i=1}^{N-1} \boldsymbol{\Gamma}(\boldsymbol{x}_i, \boldsymbol{\omega}_\gamma) \tag{4.15a}$$

NMPC3: s.t.

$$\boldsymbol{x}_0 = \boldsymbol{x}_{init} \tag{4.15b}$$

$$\boldsymbol{x}_{i+1} = \mathbf{PM}(\boldsymbol{x}_i, \boldsymbol{\tau}_{w,i}^w, \boldsymbol{d} \cdot u_{null,i}) \tag{4.15c}$$

$$|\boldsymbol{\tau}_{w,i}^w + \boldsymbol{d} \cdot u_{null,i}| \leq \boldsymbol{\tau}_{w,\,max}^w, \quad |\boldsymbol{\omega}_{bw,i}^w| \leq \boldsymbol{\omega}_{bw,\,max}^w \tag{4.15d}$$

where $\mathbf{\Lambda}$ is the penalty terms associated with $\boldsymbol{u}_{null}$:

$$\mathbf{\Lambda}(\boldsymbol{u}_{null}) = \sum_{i=0}^{N-1} \frac{1}{2} \|u_{null,i}\|^2_{R_{null}} \tag{4.16}$$

R_{null} weights the penalty of $u_{null,i}$, and is intended to be lower than the elements of $\mathbf{R}$. The null space direction for the RW configuration stated in Section 2.7.2, $\boldsymbol{d}$, is given as

$$\boldsymbol{d} = \begin{bmatrix} 1 & -1 & 1 & -1 \end{bmatrix}^\top \tag{4.17}$$

In section Section 5.7, we will show the desaturation of the RW array by means of thrusters. The desaturation scheme assumes a predefined trajectory of realizable τ_t, which is passed to the NMPC as parameters, $\boldsymbol{p}$ in Eq. (3.6). The NMPC, therefore, has knowledge of the thrusters' effects through the prediction model. Furthermore, since the design of thruster commands is decoupled from the NMPC, we may be certain that the NMPC will not misuse the thrusters for purposes of maneuvering. Thus, no fuel is wasted. We state the NMPC for desaturation, **NMPC4**, as:

$$\min_{\boldsymbol{x}, \boldsymbol{\tau}^w_w} \quad \Phi(\boldsymbol{x}, \boldsymbol{\tau}^w_w) \tag{4.18a}$$

NMPC4:

$$\text{s.t.} \quad \boldsymbol{x}_0 = \boldsymbol{x}_{init} \tag{4.18b}$$

$$\boldsymbol{\tau}_{t,i} = \boldsymbol{p}_i \tag{4.18c}$$

$$\boldsymbol{x}_{i+1} = \mathbf{PM}(\boldsymbol{x}_i, \boldsymbol{\tau}^w_{w,i}, \boldsymbol{\tau}_{t,i}) \tag{4.18d}$$

$$|\boldsymbol{\tau}^w_{w,i}| \leq \boldsymbol{\tau}^w_{w,\,max}, \quad |\boldsymbol{\omega}^w_{bw,i}| \leq \boldsymbol{\omega}^w_{bw,\,max} \tag{4.18e}$$

The parameter vector, $\boldsymbol{p}$, is updated such that it always contains thruster torques for the next N steps.

Chapter 5

Results and discussion

In this chapter, we present the results of the thesis. The results are discussed in the respective sections, such that we may properly motivate succeeding results. First, we present the specific parameters of the simulation model.

5.1 Simulation model parameters

Symbol	Description	Value	Unit	Based on
h_o	Orbital height	600	km	-
(J_{xx}, J_{yy}, J_{zz})	Moments of inertia	100, 150, 110	kgm^2	-
(J_{xy}, J_{yz}, J_{zz})	Products of inertia	-30, 0, 0	kgm^2	-
L	Length of solar panels	4	m	-
ℓ	Length to panel mount	0.5	m	-
w	Panel width	0.8	m	-
ρ	Panel area density	2.5	kg/m^2	[65]
k_d	Panel dissipation coefficient	0.005	kgm^2/s^2	[41]
EI	Panel flexural rigidity	100	Nm^2	[42]
n_m	Number of assumed modes	6	-	-
β	RW configuration parameter	$\pi/4$	rad	-
$\tau_{w,max}$	RW max torque	$\pm$ 1	N m	[66]
$\omega_{w,max}$	RW max velocity	$\pm$ 157.08	$rad\,s^{-1}$	[66]
J_w	RW inertia about spin axis	0.095	kgm^2	[43]
m_w	RW mass	2	kg	[66]
c_w	RW center of mass offset	0.1	mm	[43]
r_w	RW abs. dist. to body origin	1	m	[43]

Table 5.1: Simulation model satellite and actuator parameters

The satellite parameters used for all simulations in this thesis are listed in Table 5.1. CVODES, a stiff and non-stiff ODE solver from SUNDIALS, is used for simulation [67]. A time discretization of 0.01s is used throughout the thesis.

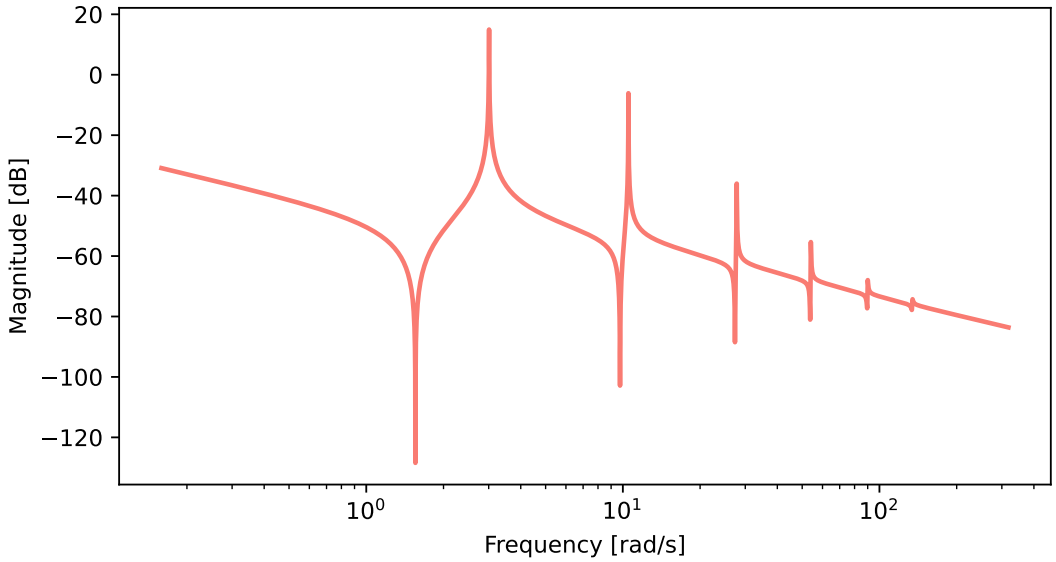

Figure 5.1: Bode plot of the simulation model, Eq. (2.75), linearized about zero position. From the first actuator to ω_x. Parameters as in Table 5.1.

We now aim to gain some insight into the specific simulation model with parameters as in Table 5.1. By linearizing the simulation model about zero position (unit quaternion, remaining states 0), we may create a Bode plot to visualize the frequency response. Fig. 5.1 the bode plot from the first τ_w (nominal torque about the x-axis) to ω_x, the axis most affected by the flexible dynamics. Six distinct resonant peaks are visible. It is apparent from the magnitude of the smaller peaks that using six assumed mode shapes is enough to capture most of the flexible system dynamics. The frequencies and periods of the six flexible modes are listen in Table 5.2.

Mode	1	2	3	4	5	6
Frequency [rad/s]	3.00	10.52	27.78	54.07	90.05	134.66
Period [s]	2.09	0.60	0.23	0.11	0.07	0.01

Table 5.2: Frequency and period of the simulation model resonant modes

As was explained in Chapter 4, the NMPC requires a relatively large input discretization because of its computational complexity. Specifically, input discretizations of $\sim$ 0.2-1.4s are explored. The specific resonant modes in Table 5.2 are therefore particularly challenging, as the most dominant modes occupy roughly the same frequency domain as that of the controller.

For convenience, we have in Appendix A listed certain components of the matrices **M**, **K** and **C** of Eq. (2.75) for structural parameters as in Table 5.1.

5.2 Prediction model parameters: B, ξ, and Ω

The virtual oscillator of the prediction models presented in Section 4.1 is intended to provide the NMPC with knowledge of how the true flexible dynamics respond to control torques. However, a good choice of B, ξ, and Ω is not necessarily that which best predicts the state of the panels. Instead, a suitable choice of oscillator parameters is one that gives a well-behaved controller. We may, therefore, think of B, ξ, and Ω as NMPC tuning parameters, but with a strong physical interpretation.

This section aims for a proper understanding of what values of B, ξ, Ω give a well-behaved NMPC. To characterize the performance of the various tunings in an unbiased fashion, we resort to Monte Carlo (MC) simulation. The MC method involves extensive simulation with the key parameters selected randomly from a predefined probability distribution [68]. We then define criteria of performance to help determine what subspace of parameters gives desired behavior.

We sample B with from a uniform distribution with an upper limit where the dynamics are no longer uniquely defined (augmented "mass matrix" no longer invertible, see Eq. (4.3)). B is chosen such that the oscillator only affects the angular velocity about $\boldsymbol{x}^b$. It, therefore, has only one nonzero element and is denoted as a scalar. ξ and Ω are sampled in the logarithmic space in order to gain improved fidelity in the regions of low resonant frequencies and damping ratios - where the lower flexible modes reside. In order to judge how robust the choice of B, ξ, Ω is to uncertainties in the flexible dynamics, we include uncertainties on EI and ρ (see Table 5.1) in the MC simulation. EI and ρ are assumed normally distributed, with means as defined in Table 5.1 and standard deviations given by the ESA factors for safety and reliability [69]. Table 5.3 shows the specific assumed distributions of all five parameters. $\mathcal{U}$ and $\mathcal{N}$ denote uniform and normal distributions, respectfully.

B	ξ	Ω	EI	ρ
$\mathcal{U}(4, 12.3)$	$10^{\mathcal{U}(-7,1)}$	$10^{\mathcal{U}(-0.5,1.3)}$	$\mathcal{N}(100, 8)$	$\mathcal{N}(2.5, 0.1)$

Table 5.3: Probability distributions for MC simulation, Fig. 5.2 and Fig. 5.3

The maneuver performed in the MC simulations is a 40-second slew to zero position from a random initial orientation. In order to reach the desired orientation, the initial Euler angles (to be converted to an initial quaternion) have an upper limit of 60° for all axes. The initial Euler angles have a lower limit of 5° for all axes to ensure that all maneuvers are sufficiently difficult. The NMPC is set to an input discretization is 0.7s and horizon of 14.7s. Since the EKF is yet to be tuned, we have $\tilde{\mathbf{Q}}$, $\tilde{\mathbf{R}}$ equal to identity, $\mathbf{EKF1}(\boldsymbol{z})$, and all external disturbances set to zero.

Since the choice of initial orientation is such that convergence to desired orientation is feasible, we define two metrics of performance based on the state of the system in the last 10 seconds of the maneuvers. Namely, Mean Squared Error (MSE) of the quaternion

vector and the torque produced by the panels on the rigid body:

$$MSE_{\mathbf{q}} = \frac{1}{n}\sum_{j=0}^{n}\mathbf{q}_{e,j} \tag{5.1a}$$

$$MSE_{\boldsymbol{\tau}_p} = \frac{1}{n}\sum_{j=0}^{n}\boldsymbol{\tau}_p := \frac{1}{n}\sum_{j=0}^{n}\mathbf{M}_{12}\ddot{\boldsymbol{\eta}}_j + \dot{\mathbf{M}}_{11}(\boldsymbol{\eta}_j, \dot{\boldsymbol{\eta}}_j) - \mathbf{M}_{\partial}(\boldsymbol{\omega}^b_{ob,j}, \boldsymbol{\eta}_j, \dot{\boldsymbol{\eta}}_j) \tag{5.1b}$$

See Eq. (2.13) and Eq. (2.75) for relevant definitions. $MSE_{\boldsymbol{\tau}_p}$ was found to generally of greater magnitude than $MSE_{\mathbf{q}}$. However, adding $MSE_{\mathbf{q}}$ to $MSE_{\boldsymbol{\tau}_p}$ proved to be sufficient in separating well-performing B, ξ, Ω from those which achieved low $MSE_{\boldsymbol{\tau}_p}$ by moving relatively slow. Therefore, the results in this section are presented only in terms of $MSE_{\mathbf{q}}$ + $MSE_{\boldsymbol{\tau}_p}$.

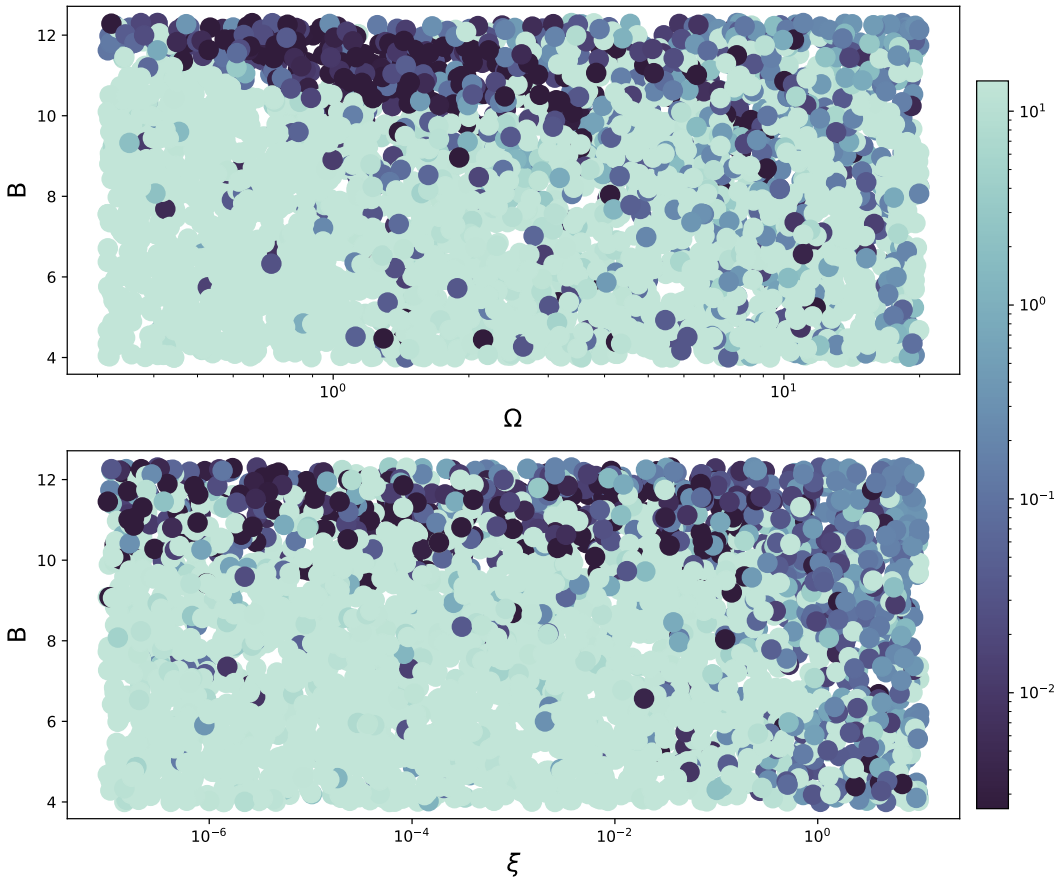

Figure 5.2: All 3423 simulations with parameters as in Table 5.3. The color gradient shows the metric $MSE_{\mathbf{q}} + MSE_{\boldsymbol{\tau}_p}$, Eq. (5.1), on a logarithmic scale. The color gradient is clipped at 2.5e-3 (lower) and at the 50th percentile (upper). The figure shows good performance and robustness for high B (10-12.3) and low Ω (0.5-2.5). Most of the better tunings also have a ξ beneath 10^{-1}.

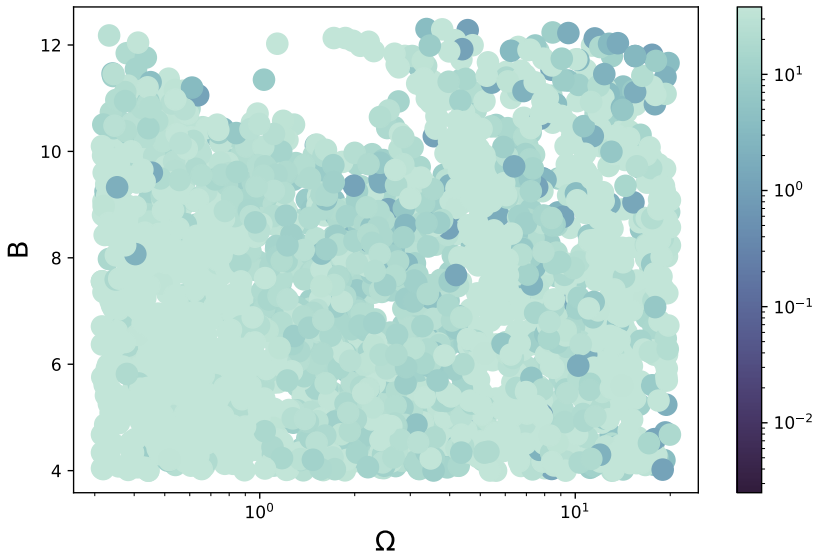

Figure 5.3: The same data as in Fig. 5.2, but without MSE better than 1. We find that the well-performing B, Ω region only contains two instances of severely poor performance, highlighting some robustness in the choice of oscillator parameters.

The results of the MC simulation with parameters as in Table 5.3 are shown in Fig. 5.2. We find that a good oscillator is one with high B (10-12.3) and low Ω (0.5-2.5). Furthermore, most of the good solutions have a ξ beneath 10^{-1}. See Fig. 4.1 for an illustration of how the three parameters shape the frequency response of the oscillator. This result indicates that the NMPC is better when it has a relatively accurate picture of the lower-frequency, most impactful, flexible modes, which is not particularly surprising. Another key takeaway from Fig. 5.2, is the seemingly complete lack of poor performance in the region previously mentioned B, Ω region. To verify whether this is the case, we remove all solutions in Fig. 5.2 with MSE lower than 1 and plot again in Fig. 5.3.

Fig. 5.3 shows that inside of the well-performing B, Ω region, we only have two instances of severely poor performance. Taking a closer look at these two instances, we find that they are large maneuvers (53°+) with ξ at the very ends of the searched space. Thus, they do not reflect a difficulty in terms of choosing appropriate B, Ω.

Now that we have shown the oscillator model to be relatively robust, we attempt to gain a deeper understanding as to what B, ξ, Ω gives superior performance. For that, we neglect the uncertainties in EI and ρ and perform a new MC simulation on a more restricted parameter space. The assumed distributions for the parameters in the second simulation are shown in Table 5.4. All other factors remain unchanged.

B	ξ	Ω
$\mathcal{U}(10, 12.3)$	$10^{\mathcal{U}(-7,-1)}$	$10^{\mathcal{U}(-0.3,0.4)}$

Table 5.4: Probability distributions for MC simulation 2, Fig. 5.4

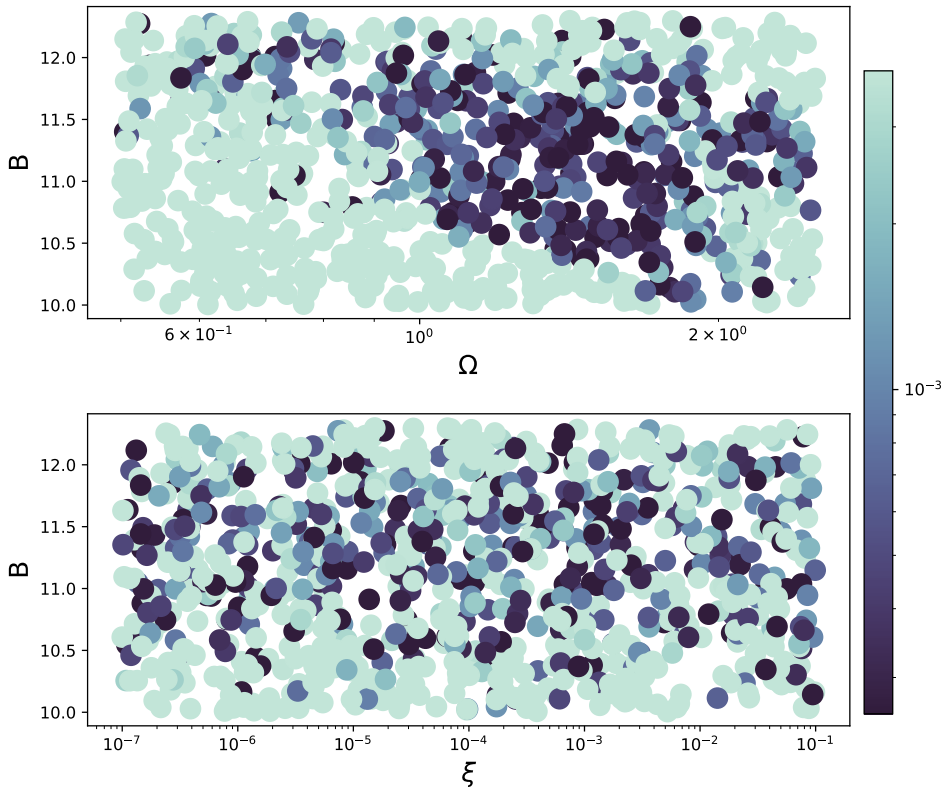

Figure 5.4: All 910 runs using parameters as in Table 5.4. The color gradient shows the metric $MSE_{\mathbf{q}} + MSE_{\tau_p}$, Eq. (5.1), on a logarithmic scale. The color scale is clipped at 2.5e-4 (lower) and at the 50th percentile (upper). No uncertainties were included in EI and ρ, as this simulation only intends to provide a clear picture of what the superior choice of B, ξ, Ω is. The result is perhaps best illustrated in the frequency domain: Fig. 5.5.

The results of the MC simulation with parameters as in Table 5.4 are shown in Fig. 5.4. We note that the color gradient has shifted, and is now much more selective. We create a Bode plot of the top 4% solutions in terms of MSE from Fig. 5.4 and remove outliers by excluding the lower and upper 15% in B, ξ and Ω. The resulting Bode plot is shown in Fig. 5.5, which shows that the best choices of B, ξ, Ω are most often approximations of the first flexible mode. The figure could also show some improvement by slightly increasing B beyond what would correspond to the first mode, to achieve an increased frequency response for higher frequencies. However, this could also be due to the relatively low sample size, and will not be investigated in further detail.

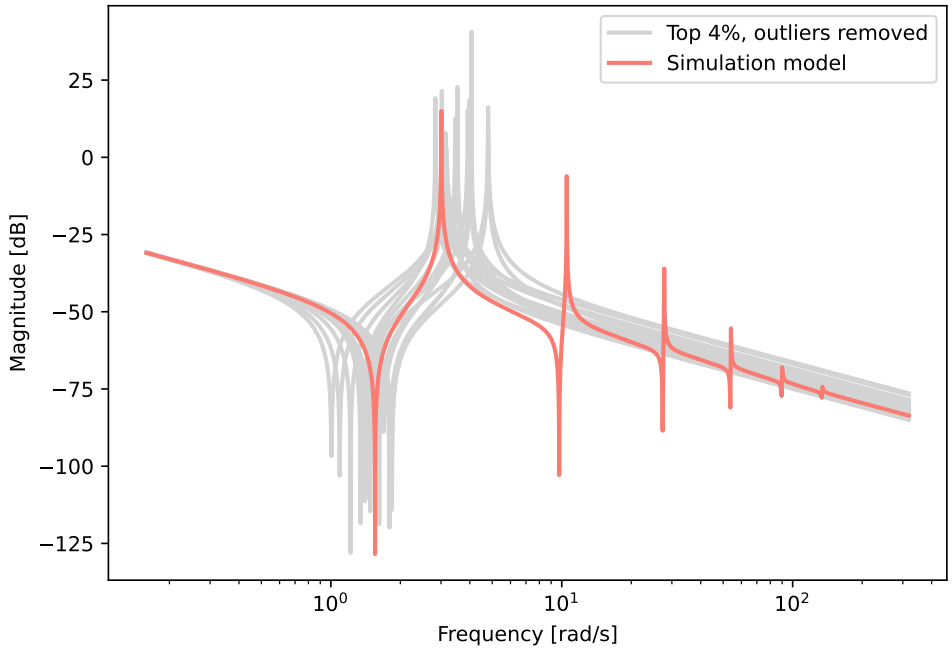

Figure 5.5: Bode plot from the first RW to ω_x, showing the B, ξ, Ω Fig. 5.4 with top 4% MSE. Outliers in terms of B, ξ, Ω are removed. The figure shows that it is desirable to choose the oscillator model, **PM1** , such that it approximates the response of the first flexible mode.

For the remainder of this thesis, we select the oscillator parameters such that its frequency response is close to, but not exactly, equal to that first flexible mode, see Table 5.5. In a physical system, one could use sensor-based modal identification techniques to identify the frequency response of the first flexible mode [70].

B	ξ	Ω
10.65	$6.3e-5$	1.58

Table 5.5: Oscillator parameters used for the remainder of this thesis.

5.3 EKF uncertainties: $\tilde{\mathbf{Q}}$ and $\tilde{\mathbf{R}}$

In Section 5.2, both external disturbances, $\boldsymbol{\tau}_{gg}$ and $\boldsymbol{\tau}_s$, were set to zero. Thus, the EKF measurement, $\boldsymbol{z}$ from Eq. (4.9a), was a close approximation to $\boldsymbol{z}_{true}$, Eq. (4.10), lacking only in "unobtainable" knowledge on the flexible dynamics. Therefore, the specific EKF tunings in terms of the uncertainties in the prediction model, $\tilde{\mathbf{Q}}$, and measurement, $\tilde{\mathbf{R}}$, were therefore not of great importance.

In this section, we examine the performance of the EKF with external disturbances switched on. Both $\boldsymbol{\tau}_{gg}$ and $\boldsymbol{\tau}_s$ affect $\dot{\boldsymbol{\omega}}_{ob}^{b}$, on which $\boldsymbol{z}$ is based. Therefore, if $\tilde{\mathbf{R}}$ is too low, the EKF might determine $\sigma, \dot{\sigma}$ that incorporate the effects of the external disturbances on $\boldsymbol{\omega}_{ob}^{b}$. However, if $\tilde{\mathbf{R}}$ is too high, the oscillator might not capture the state of the panel accurately, as $\sigma, \dot{\sigma}$ are to a larger extent based on an inaccurate prediction model. To demonstrate the importance of an accurate $\tilde{\mathbf{R}}$, we will perform the same maneuver with four different EKF implementations:

A.1 **EKF1**$(\boldsymbol{z}_{true})$, using true measurement
A.2 **EKF1**$(\boldsymbol{z}, \tilde{\mathbf{R}} = \mathbf{I}_3)$
A.3 **EKF1**$(\boldsymbol{z}, \tilde{\mathbf{R}} = 2\text{e}4\mathbf{I}_3)$
A.4 **EKF1**$(\boldsymbol{z}, \tilde{\mathbf{R}} = 2\text{e}6\mathbf{I}_3)$

The maneuver to be completed is a slew from an initial orientation of $(-34, 24, 0)$ in XYZ Euler angles to zero. The initial angular velocities of the RWs are $[-8.5,\ -8.5,\ 8.5,\ 42]$, chosen such that the static imbalance torque about $\boldsymbol{x}^b$, produced by the 2nd and 4th RW, spans both low and high frequencies at the beginning of the slew. All four simulations use an NMPC with input discretization of 0.7s and horizon of 14.7s.

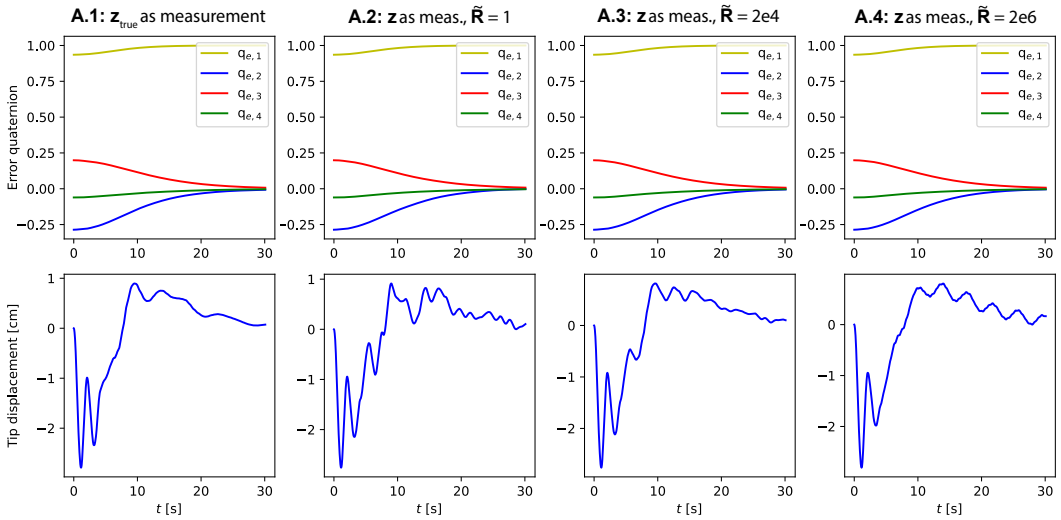

Figure 5.6: The figure shows variations of the EKF: one with "unobtainable" measurement $\boldsymbol{z}_{true}$, and three with using $\boldsymbol{z}$ with increasing values for the measurement uncertainty. As seen from the tip displacements, the four schemes are affected by external disturbances to varying degrees.

Fig. 5.6 shows the the error quaternion, $\mathbf{q}_e$, and panel tip displacements for all four manueuvers. We see that the four simulations roughly reach the desired orientation in about 30 seconds. However, the differences in performance are evident from the plots of the tip displacements. The EKF with $\boldsymbol{z}_{true}$, **A.1**, clearly exhibits the best behavior, as the resulting tip displacement is relatively smooth and does not show oscillations towards the end of the maneuver. The EKF with $\tilde{\mathbf{R}}$=1, **A.2**, shows significantly more excitation in the tip displacement plot, with some oscillations of similar frequency towards the end. The EKF with $\tilde{\mathbf{R}}$=2e4, **A.3**, shows somewhat less of this excitation, indicating a more reasonable choice of $\sigma, \dot{\sigma}$. For $\tilde{\mathbf{R}}$=2e6, **A.4**, the NMPC seems to be exciting the panels in a very regular fashion.

Fig. 5.6 gives insight into the performance of the four schemes but does not provide a complete explanation. Fig. 5.7 shows $\boldsymbol{z}_{true}$, $\boldsymbol{z}$ and the observation function, h from Eq. (4.9b), evaluated on $\hat{\boldsymbol{x}}_{k|k}$ (the post update step estimate of $\boldsymbol{x}$, see Eq. (3.13)). $h(\hat{\boldsymbol{x}}_{k|k})$ is to be interpreted as the "accepted" state estimate. Only the components of the respective quantities corresponding to $\boldsymbol{x}^b$ are plotted. Note that Fig. 5.7 only covers the very beginning of the maneuver, when the system states are most similar.

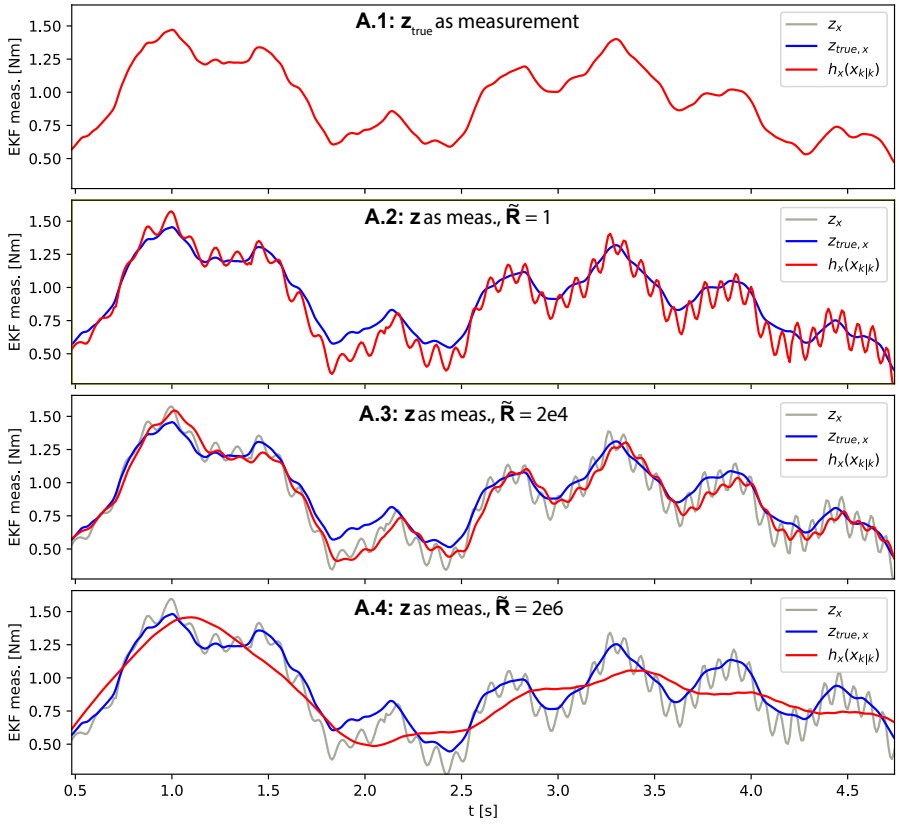

Figure 5.7: The same four cases as in Fig. 5.6. This figure shows how increasing the measurement uncertainty reduces the sensitivity to noise. In case **A.4**, the EKF fails to capture the effects of the second mode (period 0.6s).

For $\tilde{\mathbf{R}}$=1, **A.2**, in Fig. 5.7 we find that the measurement, $\boldsymbol{z}$, is not significantly altered by the EKF internal prediction. Therefore, the resulting h contains the effects of the static imbalance, giving the NMPC a distorted view of the initial state. For $\tilde{\mathbf{R}}$=2e4, **A.3**, the effects of the static imbalance are still noticeable, but much less pronounced. We see, however, that this comes at the cost of some responsiveness, as h is slightly lagged with respect to $\boldsymbol{z}_{true}$. For $\tilde{\mathbf{R}}$=2e6, **A.4**, this lack of responsiveness is very evident. The state produced by the EKF does not sufficiently capture the oscillations with a period of ∼0.6s - the period of the second mode in Table 5.2.

5.3.1 The importance of the second mode

The case of **A.4** is quite interesting. The problem seems from Fig. 5.7 to be a lack of information on the second mode. However, the second mode is not modeled in NMPC and EKF prediction models. Furthermore, it has a period of 0.6s, while the NMPC input discretization used in Fig. 5.6 and Fig. 5.7 was 0.7s. The frequency of the second mode is significantly higher than the Nyquist frequency corresponding to the input discretization. Thus, the NMPC does not "see" the full extent of the second modal vibration. In this section, we will more rigorously test the importance of whether information on the higher modes is reflected in $\sigma, \dot{\sigma}$.

To make the analysis more conclusive, we now set external disturbances to zero and use $\boldsymbol{z}_{true}$ as a measurement. To exclude information on the higher modes from $\sigma, \dot{\sigma}$, we alter the EKF. Instead of an EKF prediction model with one harmonic oscillator, we instead use two oscillators and discard the states associated with the second, σ_2 and $\dot{\sigma}_2$. The second oscillator approximates the second mode with parameters as in Table 5.6.

	B	ξ	Ω
1:	10.65	$6.3e-5$	1.58
2:	2.65	$1.6e-4$	9.55

Table 5.6: Oscillator parameters for EKF with two oscillators.

We attempt the same maneuver as in Section 5.3 with two different EKF schemes.

- **B.1** **EKF1**($\boldsymbol{z}_{true}$), parameters as in Table 5.5: EKF with oscillator approximating the first mode. The same EKF as **A.1**, the difference being that external disturbances are set to zero.
- **B.2** **EKF2**($\boldsymbol{z}_{true}$), parameters as in Table 5.6: EKF with two oscillators approximating the first and second mode. σ_2 and $\dot{\sigma}_2$ are discarded.

Fig. 5.8 shows the inputs and tip displacements of the two schemes. We clearly see that the EKF with two oscillators, **B.2**, shows some of the oscillatory behavior in the tip displacement as **A.4** did in Fig. 5.6.

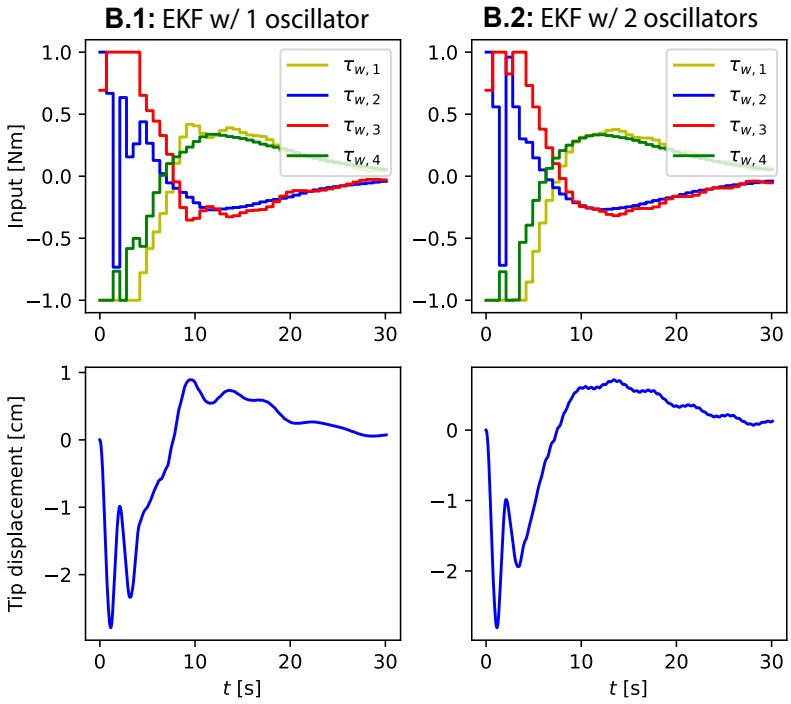

Figure 5.8: The same maneuver as in Fig. 5.6, but without external disturbances. **B.2** is an EKF that aims to neglect information on modes higher than the first. We find that this information should not be filtered out, even though it is of higher frequency than what the NMPC can control with input discretization 0.7s. The plot of inputs is included to visualize to what extent the initialization of the virtual oscillator affects the NLP solution.

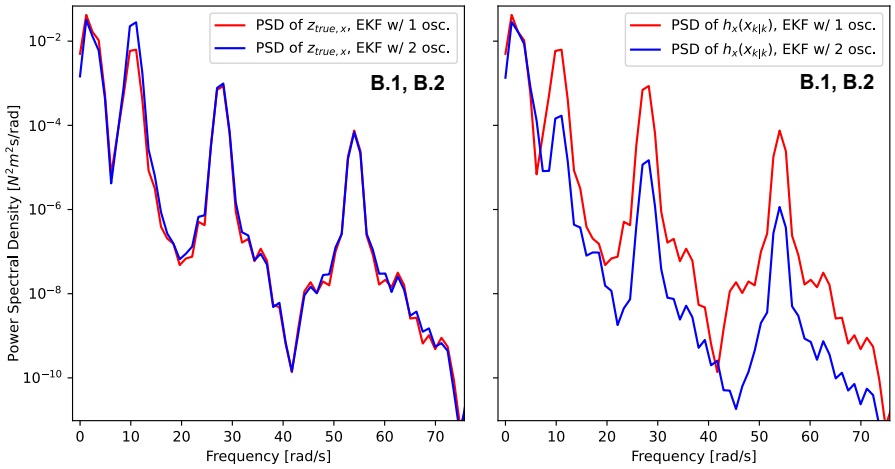

Figure 5.9: Same cases as in Fig. 5.8. The PSD of $\boldsymbol{z}_{true}$ shows to what extent the flexible modes are excited. The PSD of $h(\hat{\boldsymbol{x}}_{k|k})$ shows what part of the frequency spectrum we are actively trying to control through the initialization of the NMPC prediction model. We see that **B.2**, which discards the measurement relating to the higher modes, gives increased excitation of the second mode.

To better visualize what information $\sigma, \dot{\sigma}$ produced by the EKF with two oscillators is lacking, we plot the Power Spectral Density (PSD) of $h(\hat{\boldsymbol{x}}_{k|k})$ in Fig. 5.9. We see that by discarding the σ_2 and $\dot{\sigma}_2$, we discard most of the higher frequency information. The two-oscillator EKF scheme is, in essence, a low-pass filter. Observing now the PSD of $\boldsymbol{z}_{true}$ in Fig. 5.9, we find that the lost information only results in increased excitement of the second mode. The lack of change in the PSDs of the third and fourth modes indicates that neither scheme effectively utilize information on these modes.

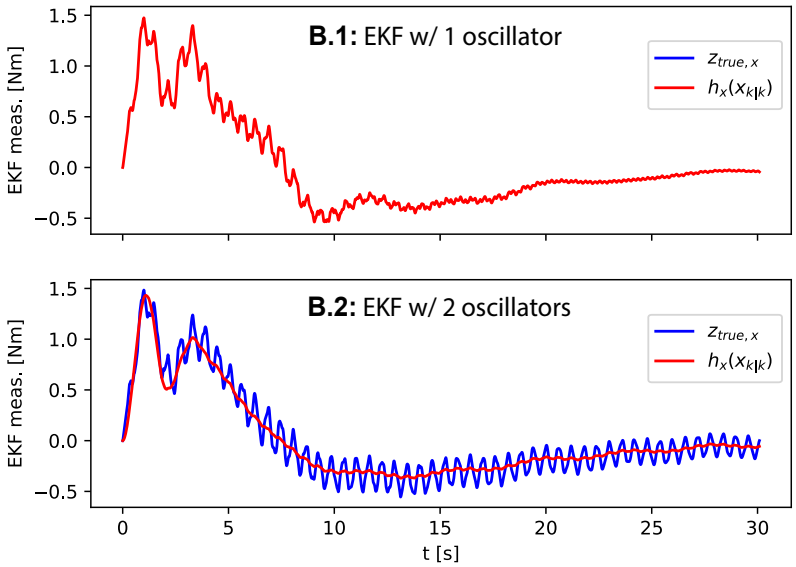

Figure 5.10: Same cases as Fig. 5.8. This figure shows that **B.2** provides a smooth approximation of the panel state. But we also see that this causes excitation of the second mode (period 0.6s).

To verify that the worse performance of the two-oscillator EKF, **B.2**, is not due to, e.g., phase lag, we plot $\boldsymbol{z}_{true}$ and $h(\hat{\boldsymbol{x}}_{k|k})$ for both schemes in Fig. 5.10. We see that the **B.2** EKF scheme produces what it should - a very smooth approximation of $\boldsymbol{z}_{true}$.

It seems from Fig. 5.10 that **B.1** avoids significantly exciting the second mode. That is, even though the NMPC in **B.1** treats the part of $\boldsymbol{z}$ corresponding to the second mode as if it behaves like the first mode (owing to the oscillator parameters, Table 5.5). We reason that the NMPC performs better if it is aware of the *extent* of the vibrations, even though it may not predict their future behavior very accurately. Or put differently, a good response to the excitement of the first mode is also a sufficiently good response to that of the second. Therefore, we conclude that neglecting measurements of the vibrations of the second flexible mode will result in decreased performance.

The fact that information on the second mode is critical in providing the NMPC with suitable $\sigma, \dot{\sigma}$ poses an important question. Namely, whether the NMPC prediction model, **PM1**, should be expanded with another, higher frequency, oscillator. Based on the results of Section 5.2, a suitable choice of parameters, B, ξ, and Ω, could be such that the second oscillator approximates the frequency response of the second flexible mode in Fig. 5.1. For the NMPC to effectively utilize the extended prediction model,

the input discretization would likely have to decrease significantly. The computational burden would therefore increase because the resulting NLP is both more complex and must be solved more often. Even though assessing computational viability is not the main aim of this thesis, we will stick with the prediction model, **PM1**, based on a single oscillator. The reasoning is that, given some bound on the computational complexity, having one significant flexible mode which can not be directly controlled could, in all probability, be an issue if the NMPC controller scheme is to be implemented on a physical system. We will therefore seize the opportunity to provide insight into the issues caused by the not directly controllable, but significant, flexible mode.

5.3.2 EKF with two oscillators

Given that we are now looking to include information on the second mode in the estimates of $\sigma, \dot{\sigma}$, one modification may be made to the EKF. Instead of one oscillator approximating the first mode with $\tilde{\mathbf{R}}$ low enough as not to neglect all effects related to the second mode, we may use two oscillators and incorporate the resulting σ_2, $\dot{\sigma}_2$ into σ_1, $\dot{\sigma}_1$. This approach requires additional knowledge of the flexible dynamics, which allows for an increased $\tilde{\mathbf{R}}$. As proposed in **EKF3** of Section 4.2:

$$\sigma_{init} = \sigma_1 + a\sigma_2, \quad \dot{\sigma}_{init} = \dot{\sigma}_1 + b\dot{\sigma}_2 \tag{5.2}$$

where $\sigma_{init}, \dot{\sigma}_{init}$ are the final product of the filter which is passed as initial conditions to the NMPC. $\sigma_1, \dot{\sigma}_1$ and $\sigma_2, \dot{\sigma}_2$ are the EKF estimates associated with the first and second oscillator, respectively. a and b are scaling constants. We now define two cases for comparison:

- **C.1** Exactly the same as **A.3**: **EKF1**($\boldsymbol{z}$, $\tilde{\mathbf{R}} = 2\text{e}4{\cdot}\mathbf{I}_3$), parameters as in Table 5.5
- **C.2** **EKF3**($\boldsymbol{z}$,$\tilde{\mathbf{R}} = 2\text{e}7{\cdot}\mathbf{I}_3$), parameters as in Table 5.6. Eq. (5.2) is used to combine the two state estimates, with $a, b = 11$.

Cases **C.1** and **C.2** are tested on the same maneuver as **A.3**: Slew from initial orientation of $(-34, 24, 0)$ in XYZ Euler angles to zero, nonzero initial RW angular velocity, and the external disturbances, $\boldsymbol{\tau}_{gg}$ and $\boldsymbol{\tau}_s$, turned on.

To examine whether **C.2** has the desired effect, we plot the PSDs of $\boldsymbol{z}_{true}$ and $h(\hat{\boldsymbol{x}}_{k|k})$ in Fig. 5.11. The choice of scaling constants a, b seems reasonable, as the second mode seems to be captured to a similar extent in $h(\hat{\boldsymbol{x}}_{k|k})$ of both **C.1** and **C.2**. We see that the increased $\tilde{\mathbf{R}}$ of **C.2** allows for increased rejection of higher frequency content not targeted by the EKF. Fig. 5.10 shows the same result: the $h(\hat{\boldsymbol{x}}_{k|k})$ produced by **C.2** is more reactive to oscillations of the second mode, and manages to reject more of the external disturbances from $\boldsymbol{z}$.

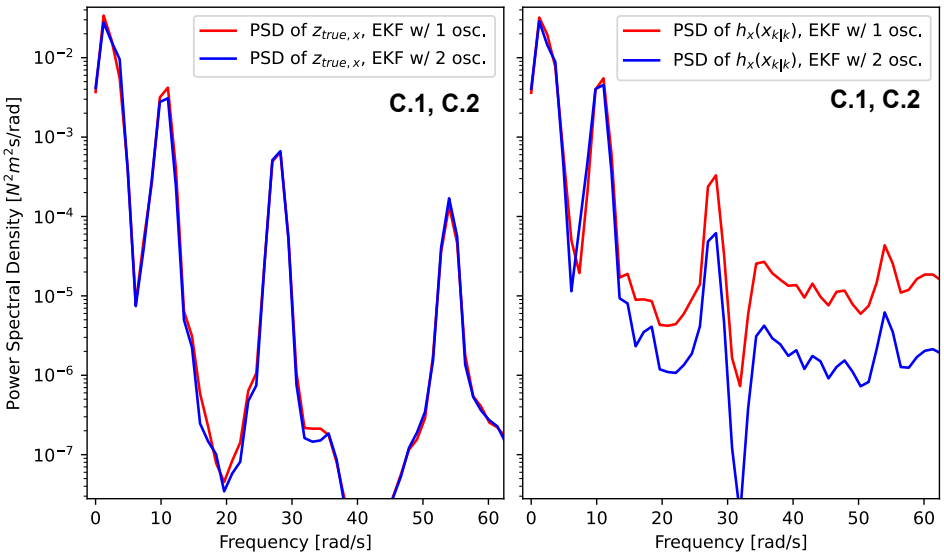

Figure 5.11: PSD of cases **C.1** and **C.2**. External disturbances are turned on. **C.2** uses an additional oscillator in the EKF prediction model, and combines the estimated parameters by Eq. (5.2). **C.2** effectively filters out most of the measurement information with frequencies higher than the second mode from $h(\hat{\boldsymbol{x}}_{k|k})$. The PSD of $\boldsymbol{z}_{true}$ indicates a small reduction in excitation of the first and second flexible modes.

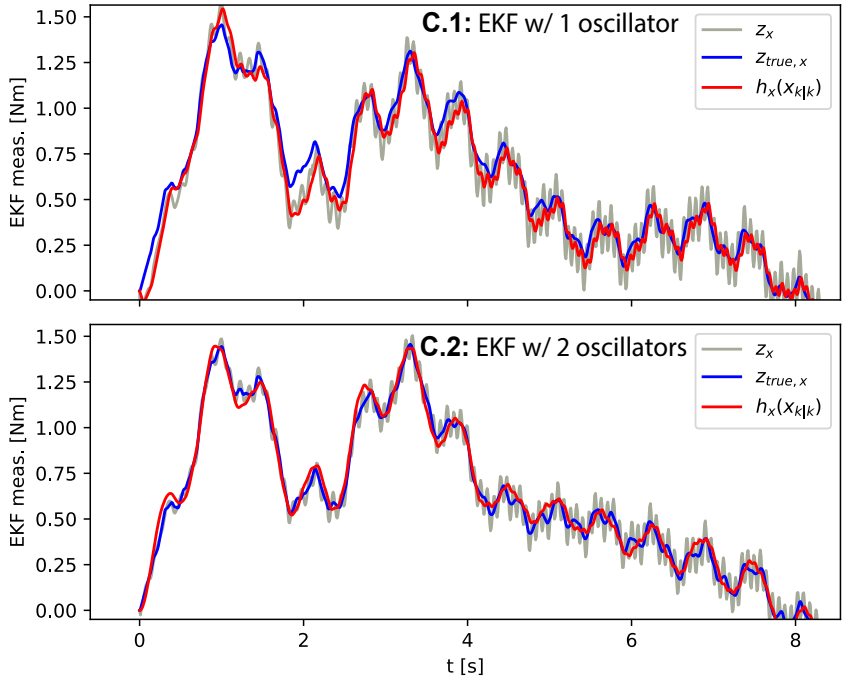

Figure 5.12: Same cases as Fig. 5.11. We see that **C.2** better captures the second mode, as well as reduces the amount of high-frequency disturbance, when compared to **C.1**

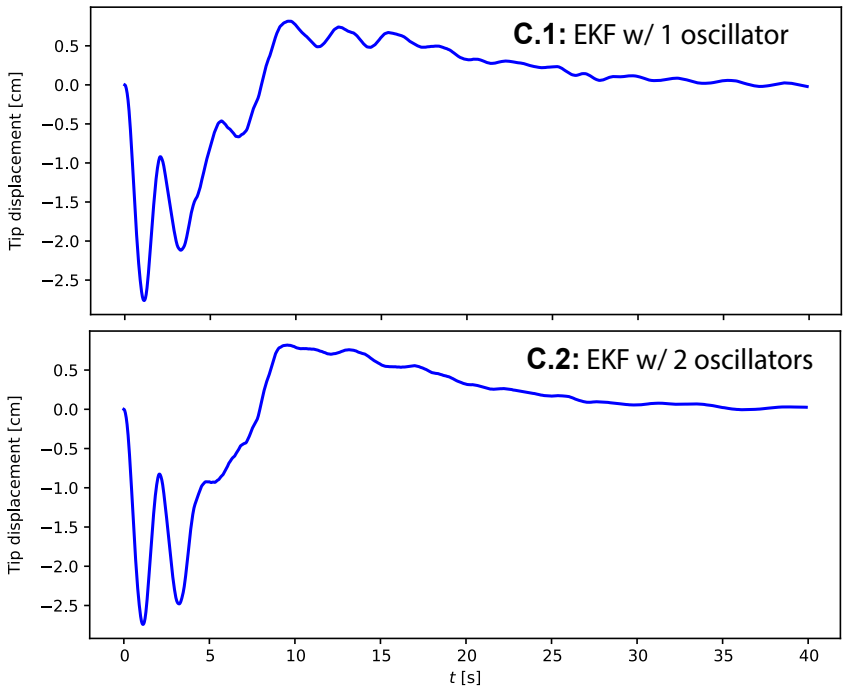

Figure 5.13: Same cases as Fig. 5.11. This figure shows that the flexible displacement with **C.2** shows less high-frequency oscillation than that of **C.1**.

In terms of tip displacement, Fig. 5.13 shows that **C.2** exhibits somewhat improved performance when compared to **C.1**. The difference is, however, not huge. We, therefore, conclude that the two-oscillator EKF, **C.2**, is not essential, but rather a nice-to-have when given sufficient knowledge of the second mode.

5.4 NMPC parameters: dt and N

In Section 5.2 and Section 5.3, the NMPC input discretization, dt, was set to 0.7s. Furthermore, the horizon was set to 14.7s, giving $N = 21$. We will see in this section that this choice, particularly in regard to dt, is by no means trivial. To quantify performance over the space of feasible dt and N, we again resort to a MC-style simulation.

To quantify performance over the space of feasible dt and N, we again resort to a MC-style simulation. In the aim of making the MC simulation as conclusive as possible, we will not include uncertainties on EI or ρ. Furthermore, external disturbances are not present. As prediction model, we use **PM1** with parameters as in Table 5.5. Since external disturbances are not present, we use the same EKF as in Section 5.2. That is, $\mathbf{EKF1}(\boldsymbol{z}, \tilde{\mathbf{R}} = 1)$. We remark that this EKF will produce σ and $\dot{\sigma}$ that reflect whether the second mode is excited.

We use MSE_τ and $MSE_\mathbf{q}$ as metrics to judge performance. In contrast to Section 5.2, the two metrics will be judged separately in this section. That is because, with a constant NMPC tuning, dt and N directly affect the speed of convergence. We define the space of various dt and N to be explored as:

N	dt
$\mathcal{U}(5, 30)$	$\mathcal{U}(0.05, 1.4)$

Table 5.7: Probability distributions for MC simulation 3, Fig. 5.14

In this section, we will consider only a slew from $(-40, 30, 0)$ XYZ Euler angles to zero orientation. Results from a simulation campaign with random initial orientation (5° to 60° for all Euler angles) are included in Appendix B, but are largely the same as that of the set slew in this section.

Fig. 5.14 shows the results of the simulation campaign defined by Table 5.7. We should first note that the $MSE_\mathbf{q}$ plot is, perhaps, a bit misleading. The higher values in the upper-right region of the plot do not necessarily indicate a poor choice of dt and N. For most of these cases, the controllers have simply not yet reached desired orientation because of an insufficient weighting of the error quaternion in the NMPC. We also note that excitation of the 3rd-6th modes is largely not reflected in the MSE metrics in Fig. 5.14. Thus, the observed effects are due to interactions with the first and, mostly, the second mode.

For both MSE_τ and $MSE_\mathbf{q}$ in Fig. 5.14, we find that performance significantly varies with dt. We have been able to find *the* definitive explanation for all of these bands. However, this section will provide some explanation, starting with the conclusion: The issue seems to be that the NMPC is unstable if the second mode is unfortunately sampled. The effects of poor sampling may perhaps be best described as aliasing-like. We should note that this is not aliasing in the traditional sense of signal processing, as the NMPC does not have any memory of the dynamics past $\boldsymbol{x}_{init}$. However, if we are providing $\boldsymbol{x}_{init}$ that does not sufficiently capture variation in the second mode over time, the NMPC is liable to give repeated inputs that further excite the mode.

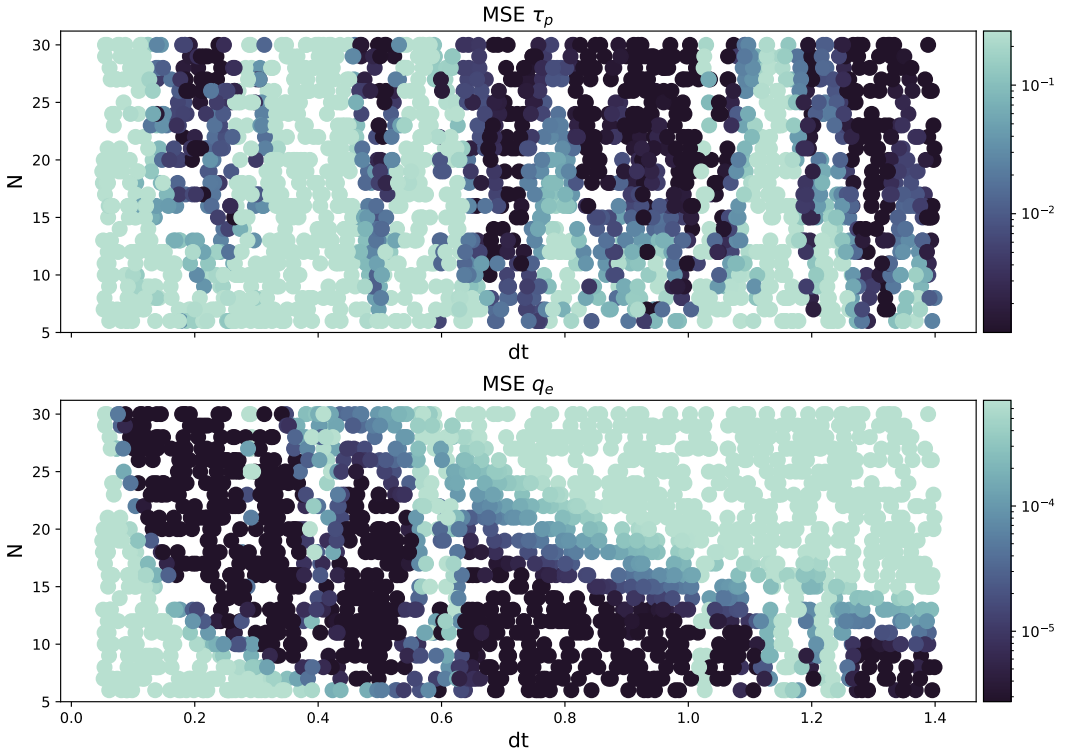

Figure 5.14: All 2362 simulations with parameters as in Table 5.7. The color gradient shows the metrics $MSE_{\mathbf{q}}$ and MSE_{τ_p}, Eq. (5.1), on a logarithmic scale. The color gradient is clipped at the 15th and 30th percentile, respectively, (lower) and at the 65th percentile (upper). We find that performance varies significantly with input discretization, dt, while the prediction horizon, N, does not show significant anomalies.

For a proper explanation of Fig. 5.14, we define four controllers for comparison:

- **D.1** **EKF2**($\boldsymbol{z}$,$\tilde{\mathbf{R}}$=1), parameters as in Table 5.6. As seen in Fig. 5.9, **EKF2** produces a measurement where most of the frequency content above the controller bandwidth is filtered out. $dt = 0.7$s, $N = 20$.
- **D.2** **EKF1**($\boldsymbol{z}$,$\tilde{\mathbf{R}}$=1). As seen in Fig. 5.9,**EKF1** produces σ and $\dot{\sigma}$ that contain information on the excitation of the second mode. $dt = 0.7$s, $N = 20$.
- **D.3** Equal to **D.2**, but with $dt = 0.57$s, $N = 20$.
- **D.4** Equal to **D.2**, but with $dt = 0.4$s, $N = 20$.

To see how the four schemes handle the excitation of the second mode differently, we initialize the second assumed modal amplitude, η_2, to 5e-5. This corresponds to a vibration, mostly of the second mode, that produces about ±0.5Nm of torque on the satellite body. We set both the initial and desired orientation to zero. $\boldsymbol{\tau}_{gg}$ and $\boldsymbol{\tau}_s$ are set to zero.

We will plot the simulated torque produced by the panel on the x-axis of the rigid body, $\tau_{p,x}$. See Eq. (5.1b) for the definition of $\boldsymbol{\tau}_p$. We will also define the non-physical torque that would be produced by the oscillator on the satellite body in **PM1**, τ_{pm} as

$$\boldsymbol{\tau}_{pm} = \mathbf{B}\ddot{\boldsymbol{\sigma}} \tag{5.3}$$

$\boldsymbol{\tau}_p$ is useful for analyzing to what extent vibrations are exited, without having to analyze the individual assumed modes. $\boldsymbol{\tau}_{pm}$ quantifies how much of this vibration the NMPC is made aware of. If we extract the NMPC decision variables corresponding to the next input step, we may plot the predicted $\boldsymbol{\tau}_{pm}$.

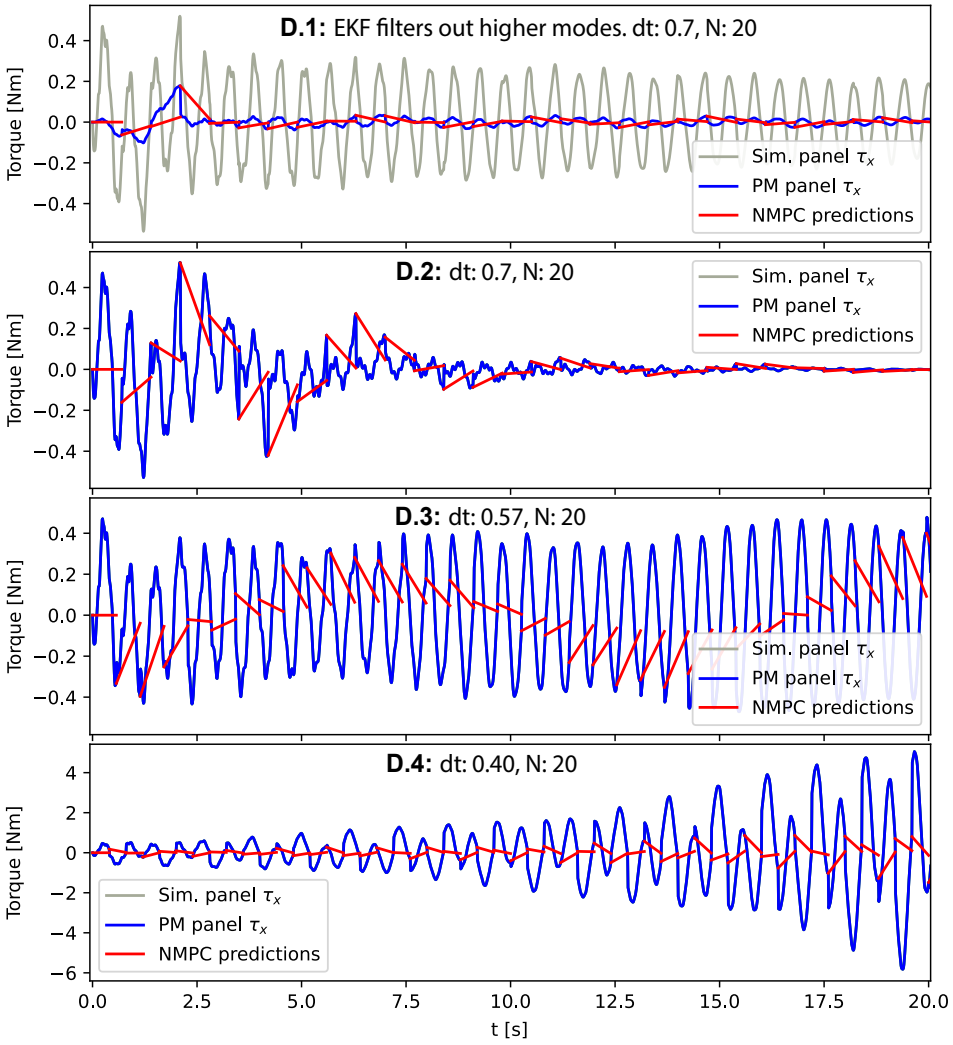

Figure 5.15: Initial orientation at zero, no external disturbances. η_2 is initialized to 5e-5. The figure shows the importance of treating the second mode as $\sigma, \dot{\sigma}$ in the NMPC (**D.1** vs. **D.2**), and the importance of an appropriate input discretization (**D.2** vs. **D.3**/**D.4**).

Fig. 5.15 shows the results of the simulation. **D.1** shows, similarly to **B.2**, that the NMPC is not able to dampen the oscillations of the second mode if the effects of the second mode are filtered out. For **D.2**, which has a dt of 0.7s, we see in Fig. 5.15 that the vibration is sampled at various stages of its cycle. Thus, the NMPC succeeds in dampening the second mode. We can see that the control actions, visualized by the red segments, are relatively different from one step to the next. For **D.3**, the NMPC is exciting vibration in the second mode. The dt of 0.57s is very close to 0.6s - the period of the second mode. Thus, the vibrations are sampled, from one input step to the next, at relatively similar stages in the vibration cycle. This results in a sequence of similar control actions that further excites the second mode. For **D.4**, while there is a pattern emerging in the NMPC predictions, the picture is perhaps a bit less clear. The oscillations grow in magnitude to nonphysical levels. It seems, also, that the panel is significantly excited by every single input.

By plotting the LOS error, e_{LOS} from Eq. (2.16), we gain a better picture of how the three approaches in Fig. 5.15 are affected in terms of attitude. Fig. 5.16 shows that the lack of a proper response in **D.1** gives a relatively small pointing error in terms of magnitude, but significant oscillations. By closer inspection, we find that the oscillations have an amplitude of ∼15m after the 40s. For **D.2**, we see a larger initial deviation from desired LOS followed by convergence without significant oscillations. For **D.3**, we see instability caused by the repeated excitation of the second mode. **D.4** has been left out of Eq. (2.16) as it excites the panels to an extent that conflicts with the underlying assumptions of the dynamic model, Eq. (2.75).

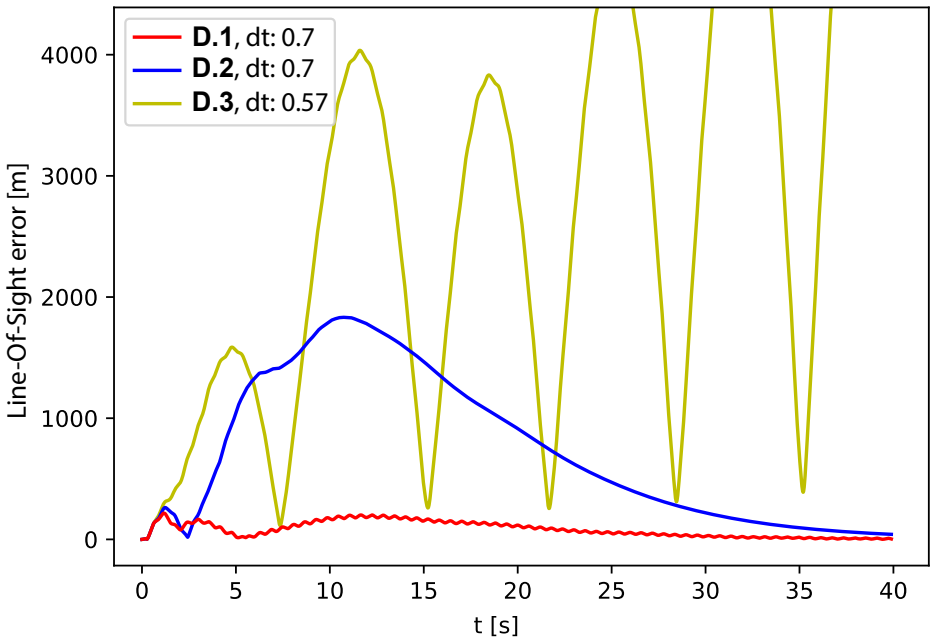

Figure 5.16: LOS errors for three of the cases in Fig. 5.15. **D.2** handles the excitation of the second mode better than **D.1** and **D.3**.

The poor performance in Fig. 5.14 for dt close to the period of the second mode is perhaps the most easily understandable. In the following subsection, we will attempt to improve our understanding of the other dt bands of poor performance in Fig. 5.14.

5.4.1 Experimental frequency response of the NMPC

We now aim to better understand if the NMPC scheme is vulnerable to disturbances at high, specific, frequencies. To approximate the frequency response of the NMPC, we will perform a series of simulations with a disturbance of increasing frequency. We will exploit the static imbalance torque, $\boldsymbol{\tau}_s$, to serve as this disturbance, as it has a frequency equal to the RW spin velocity. Specifically, we set the initial velocity of the first RW, which produces a static imbalance torque about the y- and z-axes in the body frame, to some nonzero value. Initial and desired orientations are both zero. $\boldsymbol{\tau}_{gg}$ is set to zero. The simulations were performed using **EKF1**($\boldsymbol{z}$, $\tilde{\mathbf{R}}$=1), $dt = 0.7$s and $N = 20$.

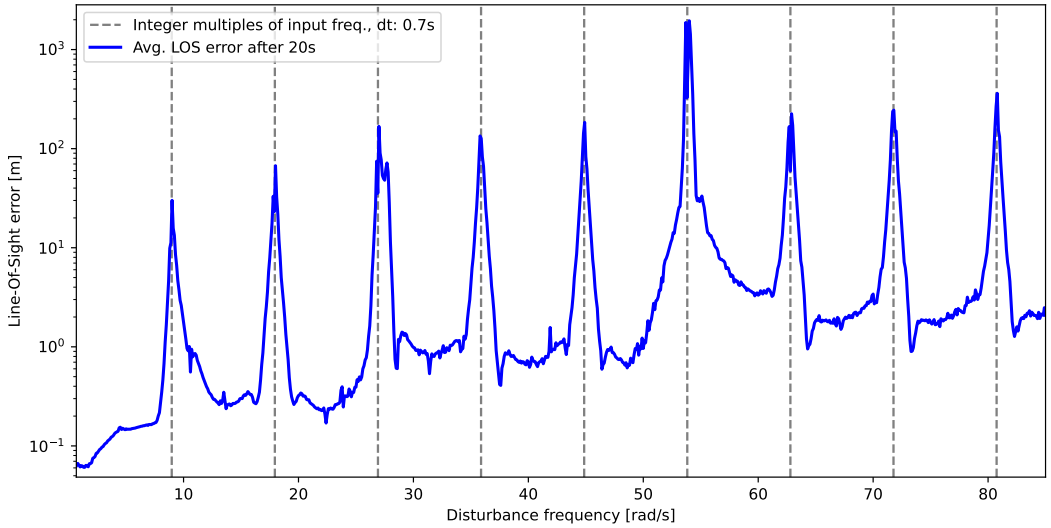

Figure 5.17: The response of the NMPC to $\boldsymbol{\tau}_s$ at different frequencies. Without appropriate filtering, the NMPC does not exhibit desired performance when faced with disturbances at an integer multiple of the controller frequency, ∼9.1 rad/s in this case.

Fig. 5.17 shows the result of 845 simulations, spanning disturbance frequencies of 0.5-85 rad/s. We note that since the magnitude of $\boldsymbol{\tau}_s$ increases with frequency, we have plotted the LOS error on a logarithmic scale. We should also note that the significantly higher peak at 53.8 rad/s in Fig. 5.17 is likely due to the proximity to the frequency of the fourth mode at 54 rad/s.

Fig. 5.17 shows that the aliasing-like effects seen in **D.3** seem to occur at all integer multiples of the controller frequency. This is no issue in terms of robustness for frequencies above that of the second mode as this content is, as seen in Fig. 5.9, not properly utilized by the NMPC. Thus, we apply filters to ensure that this frequency content is not made available to the NMPC. In the case of the second mode, however, filtering is not a viable option, as shown in Fig. 5.10 and Fig. 5.16. We must, therefore, select a NMPC dt

such that the frequency of the second mode is not an integer multiple of the controller frequency. This reasoning would explain the poor performance for $dt \simeq 1.2$ in Fig. 5.14. It does not, however, explain the poor performance of, e.g., **D.4** in Fig. 5.15. We speculate that while Fig. 5.17 shows unfavorable *reactions* to a high-frequency disturbance, we have yet to adequately explain when a poor choice of dt results in unfavorable *interactions* with the second mode.

5.4.2 Robustness in the choice of input discretization

In Section 5.4 and Section 5.4.1, we partly managed to explain how certain choices of input discretization result in poor performance. However, from an engineering perspective, finding a robust choice of input discretization is perhaps of greater importance. Therefore, we now attempt the MC-style simulation in Table 5.7, but with uncertainties in EI and ρ. All other parameters are the same as for Fig. 5.14. Using the same uncertainties for EI and ρ as in Table 5.3, we have:

N	dt	EI	ρ
$\mathcal{U}(5,30)$	$\mathcal{U}(0.05,1.4)$	$\mathcal{N}(100,8)$	$\mathcal{N}(2.5,0.1)$

Table 5.8: Probability distributions for MC simulation 4, Fig. 5.18

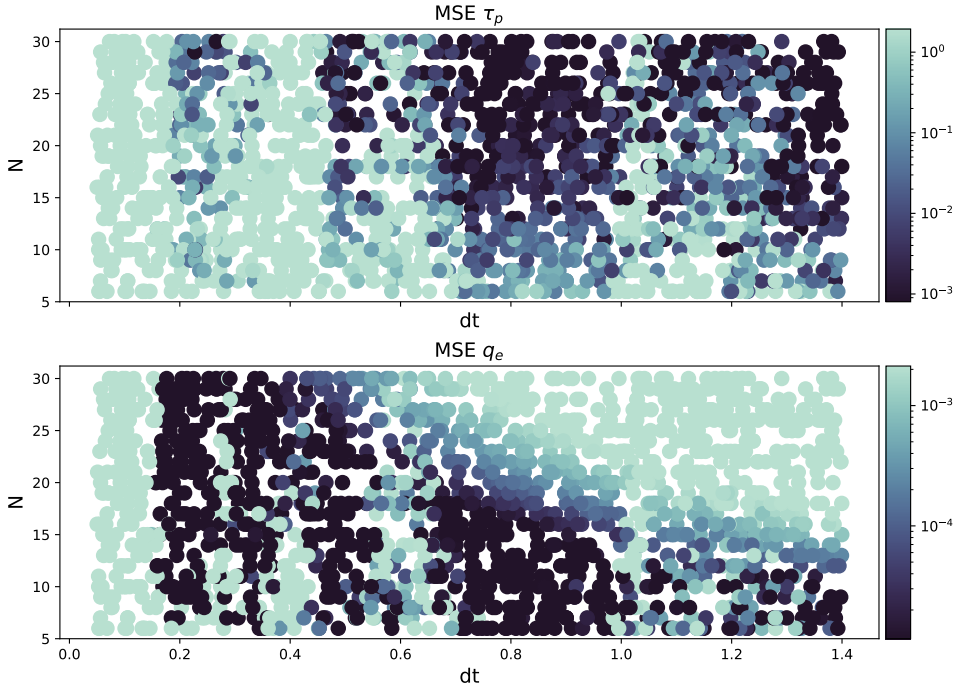

Figure 5.18: All 1992 simulations with parameters as in Table 5.8. The color gradient shows the metrics $MSE_{\mathbf{q}}$ and MSE_{τ_p}, Eq. (5.1), on a logarithmic scale. The color gradient is clipped at the 15th and 30th percentile, respectively, (lower) and at the 65th percentile (upper). The figure shows the same maneuver as in Fig. 5.14, but with uncertainties in the flexible dynamics. We find that an input discretization of ∼0.7-0.9s is the most robust.

Fig. 5.18 shows a region of reliable performance with input discretizations of ∼0.7-0.9s, and a prediction horizon over 15. We should also note that though the physical parameters of the flexible panels may not be perfectly known, they are constant. Thus, finer adjustments of dt after launch are possible.

5.5 Reaction wheel management

We have now established that the NMPC should approximate the first mode (Section 5.2), which should be initialized based on a measurement of both the first and second modes (Section 5.3). In our case, the measurement should include frequency content up to $\sim$ 12 rad/s, as to include the second mode with some margin. Furthermore, we have seen that the NMPC is sensitive to high-frequency vibrations, specifically those of the static imbalance torque (Section 5.4). Static imbalance torques with a frequency above 12 rad/s may be filtered out from the initialization of **PM1** in the NMPC. However, filters targeting disturbances of frequencies lower than 12 rad/s are not desired, as these would interfere with the accuracy in the initialization of σ and $\dot{\sigma}$.

In this section, we will utilize **NMPC2** and **NMPC3** to avoid RW velocity convergence to the $<$ 12 rad/s frequency range, as well as in the regions around ±27.8 rad/s - the frequency of the third mode. To filter out the effects of $\boldsymbol{\tau}_s$ for all RW with $\omega_{bw} > 12$ rad/s, we utilize a set of notch filters as described in Section 4.2.1. The filters are applied to the measurements of $\boldsymbol{z}$ and $\boldsymbol{\omega}_{ob}^{b}$. Notch filters alter the phase of frequency content higher than the targeted frequency, as evidenced by Fig. 4.2. Therefore, we will also apply notch filters to the modal frequencies of the 3rd-6th modes, as listed in Table 5.2. All notch filters are applied after 5s, so the array of past measurements may be initialized. We now define three cases for comparison:

- **E.1** **NMPC1** , **EKF3**($\boldsymbol{z}$, $\tilde{\mathbf{R}} =$ 2e7) with notch filters.
- **E.2** **NMPC2** , $\boldsymbol{\omega}_\gamma = [0, 27.8, -27.8]$. **EKF3**($\boldsymbol{z}$, $\tilde{\mathbf{R}} =$ 2e7) with notch filters. Γ set to zero after 40s.
- **E.3** **NMPC3** , with $\boldsymbol{\omega}_\gamma = [0, 27.8, -27.8]$. $R_{null} =$ 5e-10. **EKF3**($\boldsymbol{z}$, $\tilde{\mathbf{R}} =$ 2e7) with notch filters. Contains the null space input component. Γ set to zero after 40s.

For both **E.2** and **E.3**, we use Γ parameters of $a =$ 1e-4, $a_f =$ 1e-2. $b =$ 5e-2 for $\omega_\gamma = 0$ and $b = 1$ for $\omega_\gamma = \pm 27.8$. See Eq. (4.12) for the structure of the penalty term Γ. Furthermore, we switch off the Γ term when nearing convergence, after 40s for both **E.2** and **E.3**. The reasoning is that Γ is a smooth function, and could interfere with the convergence in $\mathbf{q}$ when is $\mathbf{q}$ small. A more robust criterion than "after 40s" could be formulated but was not deemed necessary for our purposes.

We initialize the satellite orientation at $(-30, -20, 0)$ in XYZ Euler angles, with zero as desired orientation. The RW velocities are initialized at [35, 10.5, -10.5, -20]. The NMPC parameters are $dt = 0.7$s, $N = 20$.

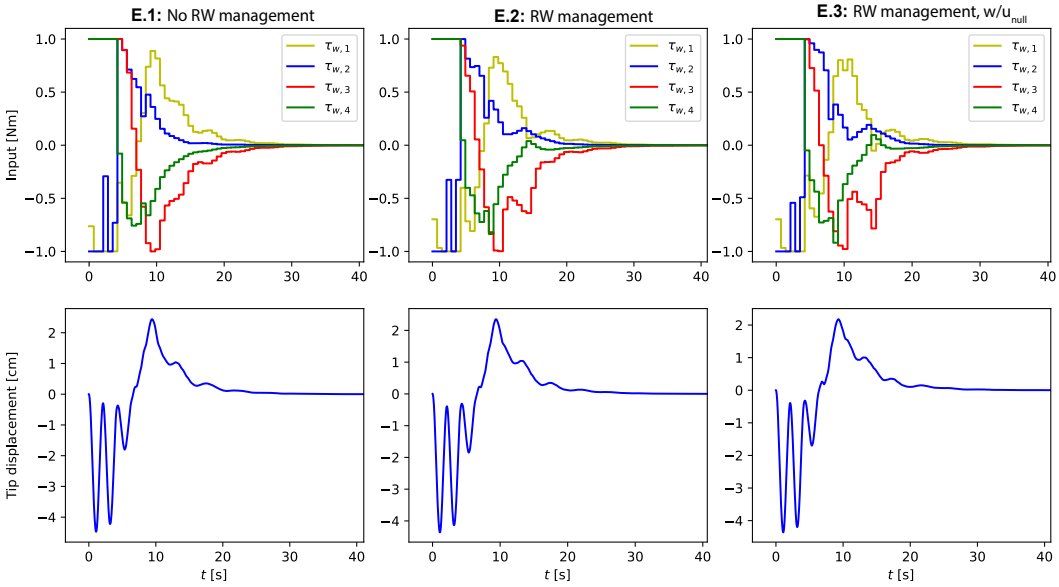

Figure 5.19: Input and tip displacements for **E.1**, **E.2** and **E.3**. **E.2** and **E.3** attempt RW management through the Γ penalty term from Eq. (4.12). **E.3** is an NMPC with a reduced penalty on movement in the RW null space. The tip displacements indicate that RW management does not have a large effect on the state of the panels.

Fig. 5.19 shows inputs and tip displacements for the three cases. All three cases converge at roughly the same time. The input profile of **E.2** and **E.3** are somewhat different than that of **E.1**. The RW velocities after 70s are found in Table 5.9.

E.1:	[28.07, 16.26, -9.63, -24.77]
E.2:	[21.11, 23.24, -16.61, -17.79]
E.3:	[20.69, 23.65, -17.03, -17.36]

Table 5.9: $\boldsymbol{\omega}_{bw}^{w}$ at t = 70s for the three cases. In rad/s.

Table 5.9 shows that **E.2** and **E.3** find roughly the same solution, with $\boldsymbol{\omega}_{bw}^{w}$ sufficiently distant from both ±10.5 and ±27.8 rad/s. **E.1**, however, converges to one wheel velocity just above the third mode (28.07 rad/s) and one just below the second mode (-9.63 rad/s). The notch filter scheme presented earlier in this paragraph does not include -9.63 rad/s, thus the effect of this disturbance will be reflected in the $\sigma, \dot{\sigma}$ passed to the NMPC.

Fig. 5.20 shows $\boldsymbol{z}$, $\boldsymbol{z}_{true}$ and $h(\hat{\boldsymbol{x}}_{k|k})$ for the three cases. Firstly, we find that the notch filters are effective in filtering out external disturbances for all three schemes, evidenced by the difference between $\boldsymbol{z}$ and $h(\hat{\boldsymbol{x}}_{k|k})$. In **E.1**, we find in $\boldsymbol{z}_{true}$ a sustained excitation of the third mode. We also observe small oscillations in $h(\hat{\boldsymbol{x}}_{k|k})$, found on closer inspection to have a frequency of $\sim$ 9.75 rad/s. The larger oscillations in $h(\hat{\boldsymbol{x}}_{k|k})$, with a period of $\sim$ 10s are likely caused by the response of the NMPC.

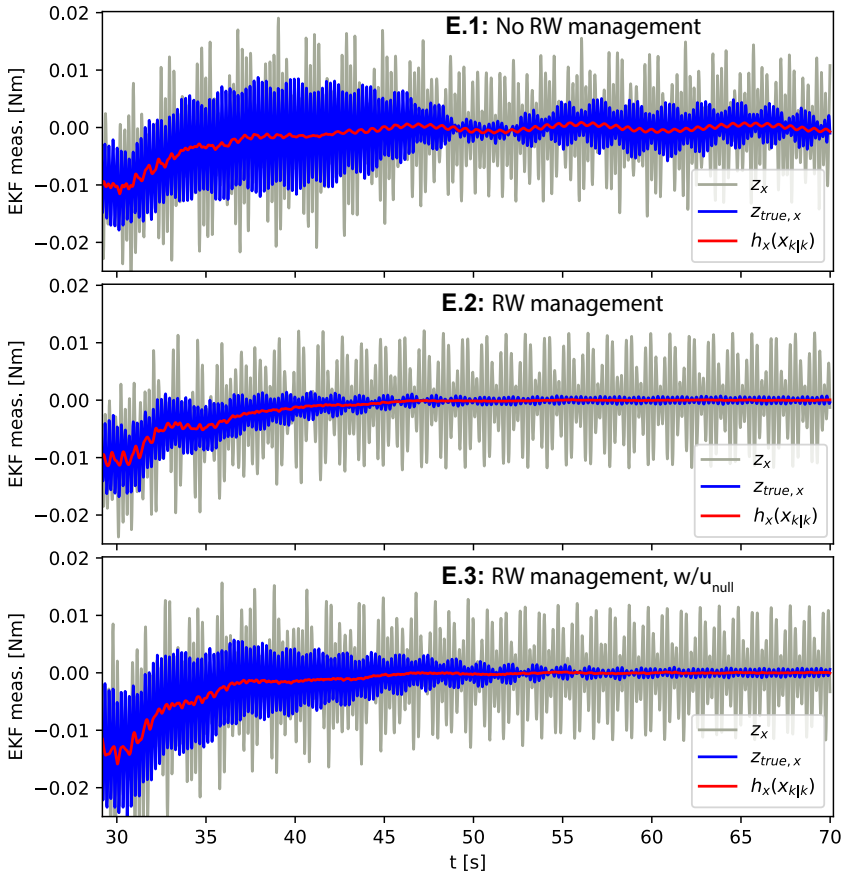

Figure 5.20: Measurement, true measurement and EKF observation function for **E.1**, **E.2** and **E.3**. When comparing $\boldsymbol{z}$ and h, we observe that the notch filters function as intended. **E.1**, which does not converge to desired RW velocities, is visibly more excited.

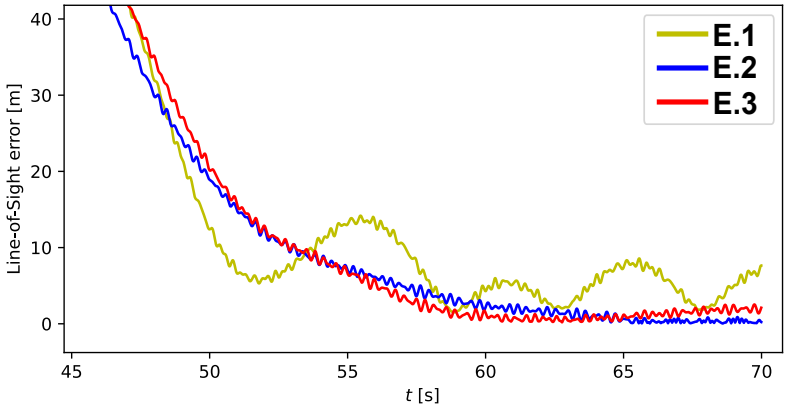

Figure 5.21: LOS as defined in Eq. (2.16) for the three cases of Fig. 5.19. We see the effects of the disturbances in h of **E.1**, as displayed in Fig. 5.20. **E.2** and **E.3** converge with fairly good precision.

Fig. 5.21 shows the LOS error of the three cases after $t = 45$s. The improvement in the performance of **E.2** and **E.3** is clear. This, however, comes at a cost. Fig. 5.22 shows the computation time of each NLP for the three schemes. Including the Γ penalty term results in a threefold increase in the computational time for **E.2** and **E.3** at the beginning of the maneuver - when the solution is the most difficult. Comparing **E.2** and **E.3**, we find no definitive reduction in computational cost by including the null space input component. Furthermore, though not covered by any of the figures, we find that $\boldsymbol{u}_{null}$ is barely used (peak 0.02Nm at $\sim$ 12s). By these two factors, we conclude that including $\boldsymbol{u}_{null}$ in **NMPC3** is unnecessary. We reason that the NMPC input weight, **R**, is likely already sufficiently low in **NMPC2** .

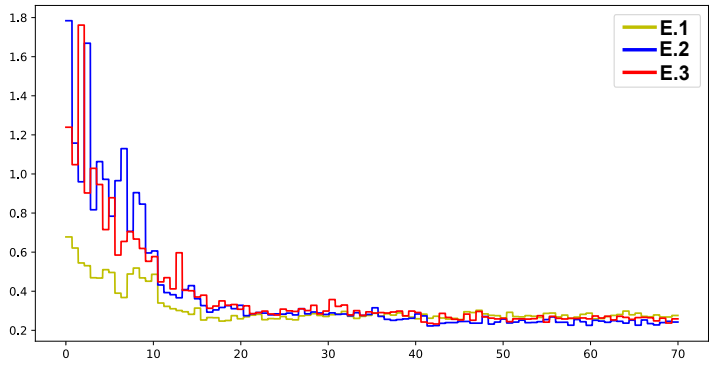

Figure 5.22: NMPC computation times of the three cases in Fig. 5.19. Both controllers with the Γ penalty term, **E.2** and **E.3**, are more computationally complex than **E.1**. Compared to **E.2**, we see no definitive improvement with the null space input component in **E.3**.

5.6 Simplified prediction models

To compensate for increased computational complexity caused by penalty terms such as Γ, certain simplifications may be made to the NMPC prediction model. Specifically, we will compare the three prediction models defined in Chapter 4. We recall that **PM2** is a prediction model in which $\dot{\boldsymbol{\omega}}_{bw}^{w}$ is decoupled from $\dot{\boldsymbol{\omega}}_{ob}^{b}$, and **PM3** is a simplification of **PM2** that neglects the RW gyroscopic effect. We define three cases:

- **F.1** **NMPC1** with **PM1**. **EKF3**($\boldsymbol{z}$, $\tilde{\mathbf{R}} = 2\text{e}7$) with notch filters.
- **F.2** **NMPC1** with **PM2**. **EKF3**($\boldsymbol{z}$, $\tilde{\mathbf{R}} = 2\text{e}7$) with notch filters.
- **F.3** **NMPC1** with **PM3**. **EKF3**($\boldsymbol{z}$, $\tilde{\mathbf{R}} = 2\text{e}7$) with notch filters.

The maneuver to be performed is one from an initial orientation of $(-50, 40, 40)$ in XYZ Euler angles to zero. The initial RW velocities are [110,110,-110,-110] rad/s. The trajectory is designed such that we achieve large $\dot{\boldsymbol{\omega}}_{ob}^{b}$, and saturate multiple RWs.

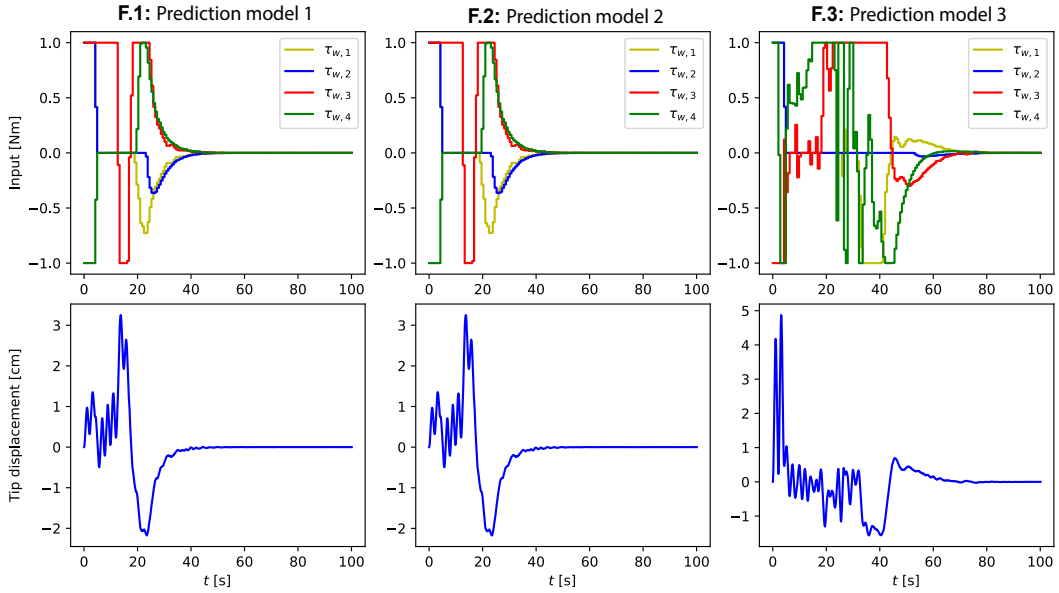

Figure 5.23: Inputs and tip displacements for **F.1**, **F.2** and **F.3**. The neglection of RW gyroscopic effect in **F.3** seemingly makes convergence difficult.

Fig. 5.23 shows the inputs and tip displacement for the three cases. **F.1** and **F.2** converge in about 40s, while **F.3** converges in about 70s. The input profile of **F.3** is less coordinated than that of **F.1** and **F.2**. **F.3** also causes increased tip displacement.

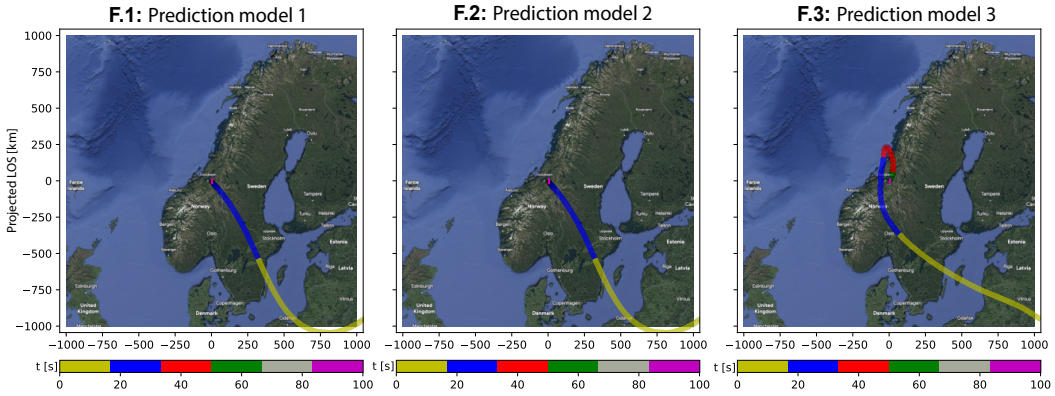

Figure 5.24: Projected line of sight, in kilometers from the target, for the same maneuvers as in Fig. 5.23. The six colors give an indication of time passed. The background from Google Earth is meant to provide intuition but is not exact. **F.3** does not converge as efficiently as **F.1** and **F.2**.

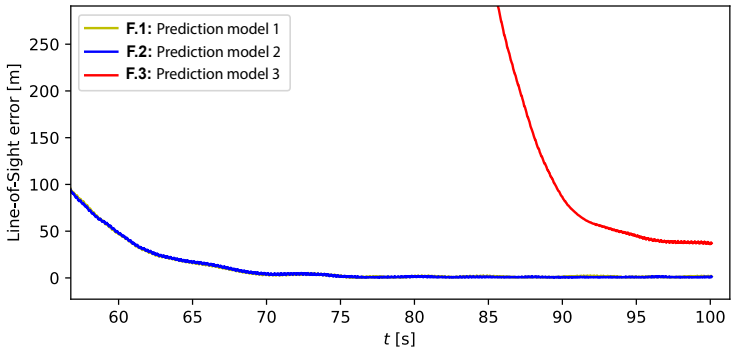

Figure 5.25: LOS errors after t=60s. No significant difference between **F.1** and **F.2**. **F.3** does not reach the target within the 100s.

Fig. 5.24 shows the LOS as projected on Earth. We recall that e_{LOS} does not account for the curvature of the Earth. Thus Fig. 5.24 is not exact. However, we see clearly that **F.3** attempts an approach much different from that of **F.1** and **F.2**. In turn, **F.3** struggles to converge efficiently. Fig. 5.25 shows that convergence without knowledge of the RW gyroscopic effect is difficult even for small $\dot{\boldsymbol{\omega}}_{ob}^{b}$ when $\dot{\boldsymbol{\omega}}_{bw}^{w}$ is large. **F.3** does not manage to fully converge within 100s, in contrast to **F.1** and **F.2**.

Fig. 5.26 shows the NMPC step computation times with the three different prediction models. We find that **F.2** reduces computational complexity by about one-third when compared to **F.1**. **F.3** is naturally the most computationally efficient. But as shown in Fig. 5.24 and Fig. 5.25, the decrease in performance is quite substantial.

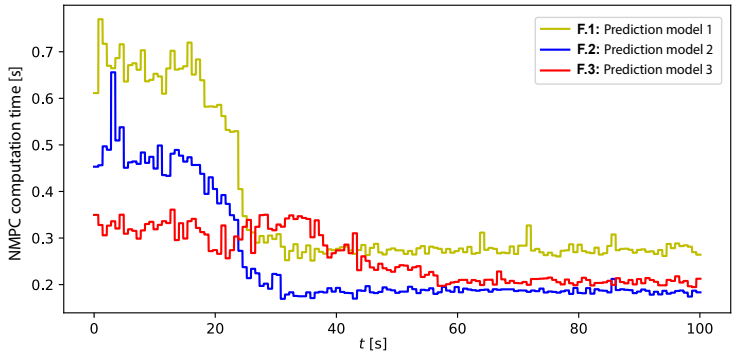

Figure 5.26: Computation times for the same maneuvers as in Fig. 5.23. We find that **F.2** significantly reduces the average computation time when compared to **F.1**. **F.3** also gives a decrease in computational complexity, but the solution is comparatively more difficult for a longer time.

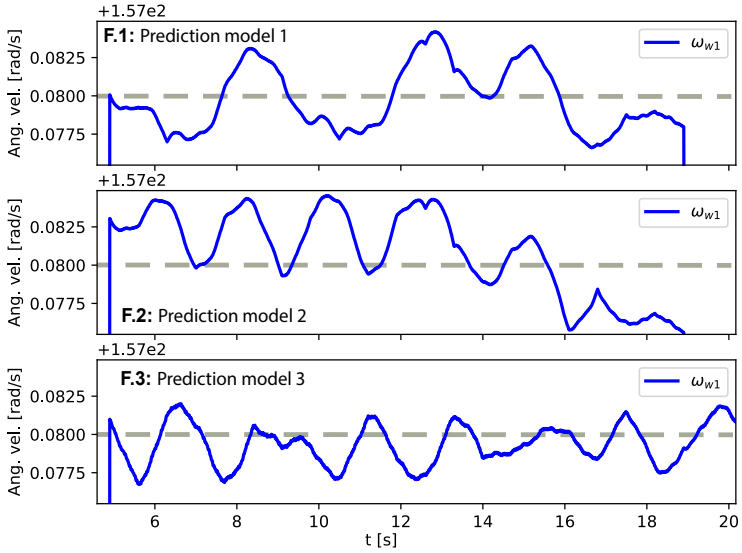

Figure 5.27: Figure shows a section in time of the maneuvers in Fig. 5.23, when all control schemes are at saturation in ω_{w1}. The grey dashed line is the constraint on RW velocity. As **F.2** and **F.3** lack dynamics of $\dot{\boldsymbol{\omega}}^w_{bw}$, the constraint is initially more violated (5.6s).

Since the dynamics of $\dot{\boldsymbol{\omega}}^w_{bw}$ are not as accurate in **F.2** as **F.1**, one potential issue could be that of violating the $\boldsymbol{\omega}^w_{bw,\,max}$ constraint. Fig. 5.27 shows the velocity of RW one, $\omega_{w,1}$, for the duration it is saturated. We see that we have some constraint violation for all three cases since $\dot{\boldsymbol{\omega}}^w_{bw}$ is coupled to $\dot{\boldsymbol{\omega}}^b_{ob}$, which experiences disturbances. Furthermore, we find that both **F.2** and **F.3** cause some violation when the constraint is first approach (5.6s). However, the violations are no larger than those seen in **F.1**. We thus conclude that, for all three prediction models, $\boldsymbol{\omega}^w_{bw,\,max}$ should be set with some small margin.

Evidenced by all figures in this section, **F.2** shows no flaws compared to **F.1**. We, therefore, conclude that the use of **PM2**, as in **F.2**, is as sufficient as **PM1**. **F.3** does provide a decrease in computational complexity but compares unfavorably in performance.

5.7 Desaturation

We will now demonstrate the desaturation scheme of **NMPC4**. We recall that the thruster torques are not decision variables of the NMPC. Instead, we pass knowledge of the equivalent body thruster torques to the NMPC as parameters in $\boldsymbol{p}$. This way, the NMPC may efficiently prepare for and react to τ_t. To demonstrate the saturation scheme, we define four cases. No thrust is applied in **G.1**, such that we may compare how the addition of some τ_t affects the execution of the maneuver.

- **G.1** **NMPC1** with **PM1**. $\tau_{t,x} = 0$Nm, no thrust applied. **EKF3**($\boldsymbol{z}$, $\tilde{\mathbf{R}} = 2e7$) with notch filters.
- **G.2** **NMPC1** with **PM1**. From 2.1s to 9.8s: $\tau_{t,x} = -1$Nm, the NMPC is not aware of the thrust. **EKF3**($\boldsymbol{z}$, $\tilde{\mathbf{R}} = 2e7$) with notch filters.
- **G.3** **NMPC4** with **PM1**. From 2.1s to 9.8s: $\tau_{t,x} = -1$Nm, $\boldsymbol{p}_{i,x} = -1$Nm, the NMPC is perfectly aware of the thrust. **EKF3**($\boldsymbol{z}$, $\tilde{\mathbf{R}} = 2e7$) with notch filters.
- **G.4** **NMPC4** with **PM1**. From 2.1s to 9.8s: $\tau_{t,x} = -1$Nm, $\boldsymbol{p}_{i,x} = -0.9$Nm, the NMPC is imperfectly aware of the thrust. **EKF3**($\boldsymbol{z}$, $\tilde{\mathbf{R}} = 2e7$) with notch filters.

$\boldsymbol{p}_{i,x}$ denotes the parameters corresponding to some input step i about the $\boldsymbol{x}^b$ axis. In **G.4**, the NMPC is given a $\boldsymbol{p}_{i,x}$ that is not exactly equal to $\tau_{t,x}$. The maneuver to be completed is a slew from an initial orientation of $(-30, 30, 0)$ in XYZ Euler angles to zero. The initial RW velocities are [110, 110, -110, -110] rad/s. The τ_t applied is one of -1Nm about $\boldsymbol{x}^b$ from over 14 input steps, from 2.1s to 9.8s. The NMPC pararmeters are $dt = 0.7$s and $N = 20$.

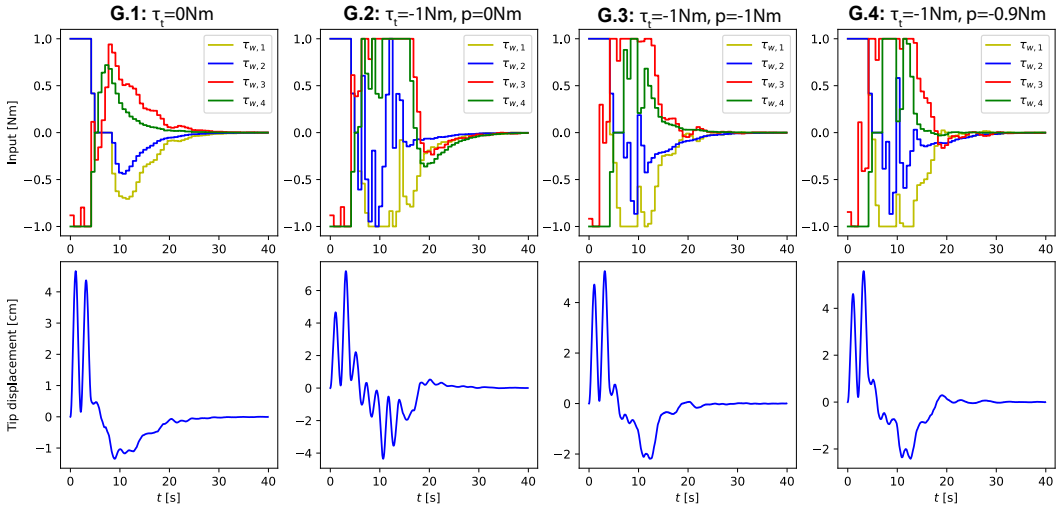

Figure 5.28: Inputs and tip displacements for **G.1**, **G.2**, **G.3** and **G.4**. Passing knowledge of τ_t as NMPC parameters in **G.3** and **G.4** does not significantly impact the execution of the maneuver. In **G.2**, where τ_t is treated as a disturbance, we find significantly more excitation of the flexible dynamics.

Fig. 5.28 shows the inputs and tip displacements for the four cases. **G.1** serves as a comparison to the three other cases. In **G.2**, τ_t is essentially treated as an unmodelled disturbance. The figure shows relatively large flexible displacements, particularly just after τ_t returns to zero. Both **G.3** and **G.4** manage to converge at about the same time as **G.1** without excessive excitation of the panels. We see from the input that both react promptly to the two changes in τ_t. The difference between **G.3** and **G.4**, **G.4** being the case in which the NMPC is aware of only 90% of τ_t, is relatively small.

G.1:	[97.86, 127.38, -92.60, -118.42]
G.2:	[41.27, 134.86, -41.60, -90.02]
G.3:	[58.87, 120.04, -24.17, -108.18]
G.4:	[54.89, 123.51, -28.10, -104.25]

Table 5.10: $\boldsymbol{\omega}_{bw}^{w}$ at t = 40s for the four cases. In rad/s.-30, -30, 0 XYZ Euler ang.

Table 5.10 shows the $\dot{\boldsymbol{\omega}}_{bw}^{w}$ at t=40s for the four cases. As expected, the desaturating torque about $\boldsymbol{x}^b$ results in lower wheel speeds for the first and third wheels.

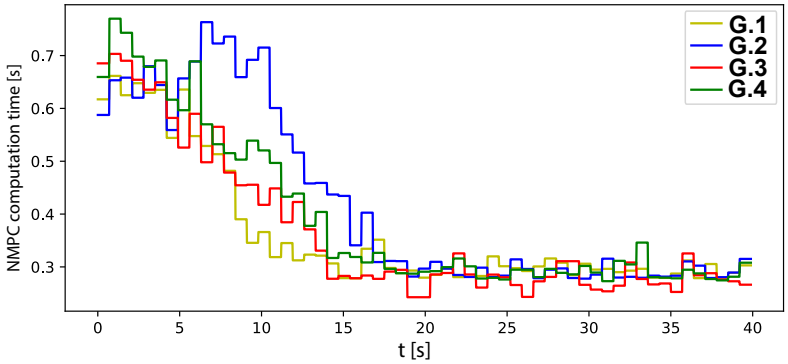

Figure 5.29: Computation times for the maneuvers in Fig. 5.28. We find no significant increase in computational complexity by the introduction of parameters in **G.3** and **G.4** when compared to **G.1**.

From Fig. 5.29, it is clear that the introduction of $\boldsymbol{p}$ comes at no significant computational expense. The lack of $\boldsymbol{p}$ in **G.2** makes convergence more complex, resulting in longer computation times.

5.8 Prospects for future work

The main result of this thesis is that an NMPC with a properly designed prediction model based on a single virtual state harmonic oscillator is sufficient, both in performance and computational complexity, for attitude control of flexible satellites. However, the implication of this result in terms of improved agility is somewhat uncertain because this thesis lacks a proper comparison with an alternative control scheme. Future work should include a comparison with an alternative controller, e.g., $\mathbf{H}_\infty$, designed with the same level of care as the NMPC in this thesis.

We also acknowledge that accurate initialization of the virtual oscillator state, as described in Section 5.3, is vital to the robustness of the NMPC scheme as presented in this thesis. Therefore, how the NMPC reacts to noisy measurements should be investigated further. The approach of estimating the prediction model initial states from a measurement of the satellite's angular acceleration might prove to be too ambitious. In that case, future work should investigate whether alternative measurements, for example through piezoelectrics or accelerometers mounted directly on the panels, are more appropriate.

Furthermore, we acknowledge that the model of the flexible dynamics is based on a fair number of assumptions, see Section 2.5.3. The performance of the NMPC scheme should also be evaluated on a more accurate simulation model such as one based on the Finite Element Method. Furthermore, the parameters of the specific flexible structure in this thesis, as well as their uncertainties, are not based on any one preexisting satellite. Future work should more rigorously define the flexible structure and its associated uncertainties, such that the performance of the NMPC scheme for uncertainties in the flexible dynamics may be extensively evaluated.

Chapter 6

Conclusion

In this thesis, we have designed a Nonlinear Model Predictive Controller for the attitude control of flexible satellites. The controller was tested on a nonlinear model of the flexible dynamics, derived using the Assumed Modes Method and Lagrange's equations. We have shown that a prediction model based on a single virtual oscillator that approximates the first flexible mode gives desired performance. Furthermore, we have shown that we may avoid excitation of the second flexible mode by actively targeting its frequency in the Extended Kalman Filter and choosing an appropriate NMPC input discretization. We have also analyzed the performance and computational complexity of the NMPC for two simplified prediction models. Lastly, we have demonstrated how to integrate RW management and desaturation into the NMPC scheme.

Bibliography

[1] J. Frich, *Specialization project: Nonlinear model predictive control of satellites with flexible appendages*, Norwegian University of Science and Technology, 2022.

[2] EUSPA, *EUSPA EO and GNSS market report*, `https://www.euspa.europa.eu/sites/default/files/uploads/euspa_market_report_2022.pdf`, 2022.

[3] S. Marcuccio, S. Ullo, M. Carminati, and O. Kanoun, "Smaller satellites, larger constellations: Trends and design issues for earth observation systems," *IEEE Aerospace and Electronic Systems Magazine*, vol. 34, no. 10, pp. 50–59, 2019.

[4] M. Marshall and S. Pellegrino, "Slew maneuver constraints for agile flexible spacecraft," in *AIAA SCITECH 2023 Forum*, 2023, p. 1883.

[5] X. C. Méndez Cubillos and L. C. G. de Souza, "Using of h-infinity control method in attitude control system of rigid-flexible satellite," *Mathematical Problems in Engineering*, vol. 2009, 2009.

[6] Ø. Hegrenæs, J. T. Gravdahl, and P. Tøndel, "Spacecraft attitude control using explicit model predictive control," *Automatica*, vol. 41, no. 12, pp. 2107–2114, 2005.

[7] S. Weiland, "H-infinity optimal control and related minimax design problems: A dynamic game approach-tamer bazar and pierre bernhard," *IEEE Transactions on Automatic Control AC*, vol. 41, pp. 1397–1399, 1996.

[8] T. Kida, I. Yamaguchi, Y. Chida, and T. Sekiguchi, "On-orbit robust control experiment of flexible spacecraft ets-vi," *Journal of Guidance, Control, and Dynamics*, vol. 20, no. 5, pp. 865–872, 1997.

[9] V. Preda, J. Cieslak, D. Henry, S. Bennani, and A. Falcoz, "Robust microvibration mitigation and pointing performance analysis for high stability spacecraft," *International Journal of Robust and Nonlinear Control*, vol. 28, no. 18, pp. 5688–5716, 2018.

[10] R. Rodrigues, V. Preda, F. Sanfedino, and D. Alazard, "Modeling, robust control synthesis and worst-case analysis for an on-orbit servicing mission with large flexible spacecraft," *Aerospace Science and Technology*, p. 107 865, 2022.

[11] A. Zulu and S. John, "A review of control algorithms for autonomous quadrotors," *arXiv preprint arXiv:1602.02622*, 2016.

[12] J. Zhang, X. Kong, C. Liu, Q. Deng, and K. Shi, "Agile attitude maneuver with active vibration-suppression for flexible spacecraft," *Journal of the Franklin Institute*, vol. 359, no. 3, pp. 1172–1195, 2022.

[13] J. L. R. Gutiérrez and A. Heidecker, "Nonlinear controller design for a flexible spacecraft," *The Journal of the Astronautical Sciences*, vol. 67, no. 4, pp. 1500–1520, 2020.

[14] X. Cao, C. Yue, and M. Liu, "Flexible satellite attitude maneuver via constrained torque distribution and active vibration suppression," *Aerospace Science and Technology*, vol. 67, pp. 387–397, 2017.

[15] I. M. da Fonseca, D. A. Rade, L. C. Goes, and T. de Paula Sales, "Attitude and vibration control of a satellite containing flexible solar arrays by using reaction wheels, and piezoelectric transducers as sensors and actuators," *Acta Astronautica*, vol. 139, pp. 357–366, 2017.

[16] V. Preda, F. Sanfedino, S. Bennani, F. Boquet, and D. Alazard, "Robust and adaptable dynamic response reshaping of flexible structures," *Journal of Sound and Vibration*, vol. 468, p. 115 086, 2020.

[17] S. Di Cairano and I. V. Kolmanovsky, "Real-time optimization and model predictive control for aerospace and automotive applications," in *2018 annual American control conference (ACC)*, IEEE, 2018, pp. 2392–2409.

[18] J. Ramírez and L. Hewing, "Sequential convex programming for optimal line of sight steering in agile missions," *arXiv preprint arXiv:2206.06061*, 2022.

[19] V. Preda, A. Hyslop, and S. Bennani, "Optimal science-time reorientation policy for the comet interceptor flyby via sequential convex programming," *CEAS Space Journal*, vol. 14, no. 1, pp. 173–186, 2022.

[20] J. T. Wen, S. Seereeram, and D. Bayard, "Nonlinear predictive control applied to spacecraft attitude control," in *Proceedings of the 1997 American Control Conference (Cat. No. 97CH36041)*, IEEE, vol. 3, 1997, pp. 1899–1903.

[21] R. Gupta, U. V. Kalabić, S. Di Cairano, A. M. Bloch, and I. V. Kolmanovsky, "Constrained spacecraft attitude control on so (3) using fast nonlinear model predictive control," in *2015 American Control Conference (ACC)*, IEEE, 2015, pp. 2980–2986.

[22] D. Y. Lee, R. Gupta, U. V. Kalabić, S. Di Cairano, A. M. Bloch, J. W. Cutler, and I. V. Kolmanovsky, "Constrained attitude maneuvering of a spacecraft with reaction wheel assembly by nonlinear model predictive control," in *2016 American Control Conference (ACC)*, IEEE, 2016, pp. 4960–4965.

[23] H.-S. Myung and H. Bang, "Nonlinear predictive attitude control of spacecraft under external disturbances," *Journal of spacecraft and rockets*, vol. 40, no. 5, pp. 696–699, 2003.

[24] J. Sieber, S. Bennani, and M. N. Zeilinger, "A system level approach to tube-based model predictive control," *IEEE Control Systems Letters*, vol. 6, pp. 776–781, 2021.

[25] Y. Ikeda, T. Nakajima, and Y. Chida, "Attitude control of spacecraft by nmpc with consideration of singularity avoidance of cmg," in *2012 IEEE 51st IEEE Conference on Decision and Control (CDC)*, IEEE, 2012, pp. 1733–1739.

[26] H. Park, R. Zappulla, C. Zagaris, J. Virgili-Llop, and M. Romano, "Nonlinear model predictive control for spacecraft rendezvous and docking with a rotating target," in *27th AAS/AIAA Spaceflight Mechanics Meeting*, vol. 2, 2017.

[27] T. Rybus, K. Seweryn, and J. Z. Sasiadek, "Control system for free-floating space manipulator based on nonlinear model predictive control (NMPC)," *Journal of Intelligent & Robotic Systems*, vol. 85, pp. 491–509, 2017.

[28] B. P. Malladi, S. Di Cairano, and A. Weiss, "Nonlinear model predictive control of coupled rotational-translational spacecraft relative motion," in *2019 American control conference (ACC)*, IEEE, 2019, pp. 3581–3586.

[29] A. Murilo, P. J. de Deus Peixoto, L. C. G. de Souza, and R. V. Lopes, "Real-time implementation of a parameterized model predictive control for attitude control systems of rigid-flexible satellite," *Mechanical systems and signal processing*, vol. 149, pp. 107–129, 2021.

[30] P. Iannelli, F. Angeletti, and P. Gasbarri, "A model predictive control for attitude stabilization and spin control of a spacecraft with a flexible rotating payload," *Acta Astronautica*, vol. 199, pp. 401–411, 2022.

[31] Y. Wang, A. Wynn, and R. Palacios, "Model-predictive control of flexible aircraft dynamics using nonlinear reduced-order models," in *57th AIAA/ASCE/AHS/ASC Structures, Structural Dynamics, and Materials conference*, 2016, p. 0711.

[32] M. Artola, A. Wynn, and R. Palacios, "Modal-based nonlinear model predictive control for 3-d very flexible structures," *IEEE Transactions on Automatic Control*, vol. 67, no. 5, pp. 2145–2160, 2021.

[33] M. J. Sidi, *Spacecraft dynamics and control: a practical engineering approach*. Cambridge university press, 1997, vol. 7.

[34] ESA, *Types of orbits*, `https://www.esa.int/Enabling_Support/Space_Transportation/Types_of_orbits`, Accessed: 2023-05-01, 2020.

[35] F. L. Markley and J. L. Crassidis, *Fundamentals of spacecraft attitude determination and control*. New York, NY: Springer, 2014, vol. 1286.

[36] O. Egeland and J. T. Gravdahl, *Modeling and simulation for automatic control*. Trondheim, Norway: Marine Cybernetics, 2002, vol. 76.

[37] T. I. Fossen, *Handbook of marine craft hydrodynamics and motion control*. Hoboken, NJ: John Wiley & Sons, 2011.

[38] L. Liu, D. Cao, and X. Tan, "Studies on global analytical mode for a three-axis attitude stabilized spacecraft by using the rayleigh–ritz method," *Archive of Applied Mechanics*, vol. 86, no. 12, pp. 1927–1946, 2016.

[39] J. L. Junkins, *Introduction to dynamics and control of flexible structures*. Reston, VA: AIAA, 1993.

[40] L. Mazzini, *Flexible Spacecraft Dynamics, Control and Guidance: Technologies by Giovanni Campolo*. Cham, Switzerland: Springer, 2015.

[41] X. Zhao, Z. Wang, and G. Zheng, "Policy optimization for vibration isolator stiffness control during agile attitude maneuvers," *Mechanical Systems and Signal Processing*, vol. 165, p. 108 279, 2022.

[42] J. Gutierrez, "Attitude control of flexible spacecraft," M.S. thesis, TU Delft, 2019.

[43] ECSS-Secretariat, "Spacecraft mechanical loads analysis handbook," *European Cooperation for Space Standardization*, 2013.

[44] Y. Kim, J. Junkins, and A. Kurdila, "On the consequences of certain modeling approximations in dynamics and control of flexible space structures," in *33rd Structures, Structural Dynamics and Materials Conference*, 1992, p. 2206.

[45] Z.-y. Liu, J.-z. Hong, and J.-y. Liu, "Complete geometric nonlinear formulation for rigid-flexible coupling dynamics," *Journal of Central South University of Technology*, vol. 16, no. 1, pp. 119–124, 2009.

[46] F. Karray, A. Grewal, M. Glaum, and V. Modi, "Stiffening control of a class of nonlinear affine systems," *IEEE Transactions on Aerospace and Electronic Systems*, vol. 33, no. 2, pp. 473–484, 1997.

[47] J. Turner and H. Chun, "Optimal distributed control of a flexible spacecraft during a large-angle maneuver," *Journal of Guidance Control and Dynamics*, vol. 7, pp. 257–264, May 1984. DOI: 10.2514/3.19853.

[48] W. Zhu and C. Mote Jr, "Dynamic modeling and optimal control of rotating euler-bernoulli beams," 1997.

[49] T. A. Elgohary and J. D. Turner, "Generalized frequency domain modeling and analysis for a flexible rotating spacecraft," in *AIAA Modeling and Simulation Technologies (MST) Conference*, 2013, p. 4914.

[50] M. Malekzadeh, A. Naghash, and H. A. Talebi, "A robust nonlinear control approach for tip position tracking of flexible spacecraft," *IEEE Transactions on Aerospace and Electronic Systems*, vol. 47, no. 4, pp. 2423–2434, 2011.

[51] F. A. Leve, B. J. Hamilton, and M. A. Peck, *Spacecraft momentum control systems*. Cham, Switzerland: Springer, 2015, vol. 1010.

[52] T. R. Krogstad and J. T. Gravdahl, "6-dof mutual synchronization of formation flying spacecraft," in *Proceedings of the 45th IEEE Conference on Decision and Control*, IEEE, 2006, pp. 5706–5711.

[53] S. Gros, M. Zanon, R. Quirynen, A. Bemporad, and M. Diehl, "From linear to nonlinear mpc: Bridging the gap via the real-time iteration," *International Journal of Control*, vol. 93, no. 1, pp. 62–80, 2020.

[54] B. Foss and A. N. Heirung, *Merging optimization and control*, [PDF document]. Available: https://folk.ntnu.no/bjarnean/Publications/OptimalControl.pdf, 2016.

[55] J. Nocedal and S. J. Wright, *Numerical optimization*. New York, NY: Springer, 1999.

[56] S. Gros, *Numerical optimal control. lecture 4: Shooting methods*, [PDF document], 2022.

[57] A. Wächter and L. T. Biegler, "On the implementation of an interior-point filter line-search algorithm for large-scale nonlinear programming," *Mathematical programming*, vol. 106, no. 1, pp. 25–57, 2006.

[58] S. Gros and M. Diehl, *Numerical optimal control*, [PDF document]. Available: `https://www.syscop.de/files/2020ss/NOC/book-NOCSE.pdf`, 2022.

[59] C. K. Chui and G. Chen, *Kalman filtering*. Berlin, Heidelberg: Springer, 2017.

[60] H. R. E. Siller, "Non-linear modal analysis methods for engineering structures," Ph.D. dissertation, University of London, 2004.

[61] S. Cetinkunt and W. J. Book, "Flexibility effects on the control system performance of large scale robotic manipulators," *Journal of the Astronautical Sciences*, vol. 38, pp. 531–556, 1990.

[62] G. Ellis, *Control system design guide: using your computer to understand and diagnose feedback controllers*. St. Louis: Butterworth-Heinemann, 2012.

[63] S. J. Orfanidis, *Introduction to signal processing*. Upper Saddle River, N.J: Prentice-Hall, 1995.

[64] T. Zhang and P. Ferguson, "Optimal reaction wheel control with stiction and resonance avoidance," in *Space Operations: Beyond Boundaries to Human Endeavours*, Springer, 2022, pp. 687–701.

[65] *Solar arrays: Product information*, STI-DS-03-201809, SpaceTech GmbH.

[66] OCE Technology, *Reaction Wheels: OCE-RW1000*, `https://satsearch.co/products/oce-technology-rw1000-reaction-wheel`, Accessed: 2023-05-01.

[67] D. J. Gardner, D. R. Reynolds, C. S. Woodward, and C. J. Balos, "Enabling new flexibility in the SUNDIALS suite of nonlinear and differential/algebraic equation solvers," *ACM Transactions on Mathematical Software (TOMS)*, 2022.

[68] J. Hanson and B. Beard, *Applying monte carlo simulation to launch vehicle design and requirements analysis*, [PDF document]. Available: `https://ntrs.nasa.gov/api/citations/20100038453/downloads/20100038453.pdf`, 2010.

[69] P. Esnault and M. Klein, "Factors of safety and reliability," in *Spacecraft Structures, Materials and Mechanical Engineering*, vol. 386, 1996, p. 109.

[70] C. Stephan, "Sensor placement for modal identification," *Mechanical Systems and Signal Processing*, vol. 27, pp. 461–470, 2012.

Appendix A

Model-related integrals

The integrals that partly make up **M**, **K**, **C** are listed below for the particular case of $L = 4$, $\ell = 0.5$ and $k = 6$. The evaluations were performed using the Python library SymPy, and are rounded to one decimal point.

$$\int_0^4 (s+0.5)\phi_k \, ds : \begin{bmatrix} 36.3 \\ -82.1 \\ 217.6 \\ -358.5 \\ 585.9 \\ -819.1 \end{bmatrix}, \quad \int_0^4 (s+0.5)^2 \, ds = 30.3 \tag{A.1}$$

$$\int_0^4 \frac{\partial^2 \phi_{k_1}}{\partial^2 s} \frac{\partial^2 \phi_{k_2}}{\partial^2 s} ds : \begin{bmatrix} 2.3 & -6.1 & 13.7 & -24.4 & 38.1 & -54.8 \\ -6.1 & 36.5 & -54.8 & 97.4 & -152.2 & 219.2 \\ 13.7 & -54.8 & 184.9 & -219.2 & 342.5 & -493.1 \\ -24.4 & 97.4 & -219.2 & 584.5 & -608.8 & 876.7 \\ 38.1 & -152.2 & 342.5 & -608.8 & 1426.9 & -1369.8 \\ -54.8 & 219.2 & -493.1 & 876.7 & -1369.8 & 2958.8 \end{bmatrix} \tag{A.2}$$

$$\int_0^4 \phi_{k_1} \phi_{k_2} \, ds : \begin{bmatrix} 46.6 & -110.7 & 281.6 & -470.7 & 762.3 & -1071.8 \\ -110.7 & 273.1 & -675.2 & 1136.2 & -1831.7 & 2582.6 \\ 281.6 & -675.2 & 1710.5 & -2856.8 & 4623.7 & -6502.8 \\ -470.7 & 1136.2 & -2856.8 & 4790.8 & -7738.3 & 10894.2 \\ 762.3 & -1831.7 & 4623.7 & -7738.3 & 12519.1 & -17610.6 \\ -1071.8 & 2582.6 & -6502.8 & 10894.2 & -17610.6 & 24788.7 \end{bmatrix} \tag{A.3}$$

Appendix B

MC simulation of dt and N with random initial orientation

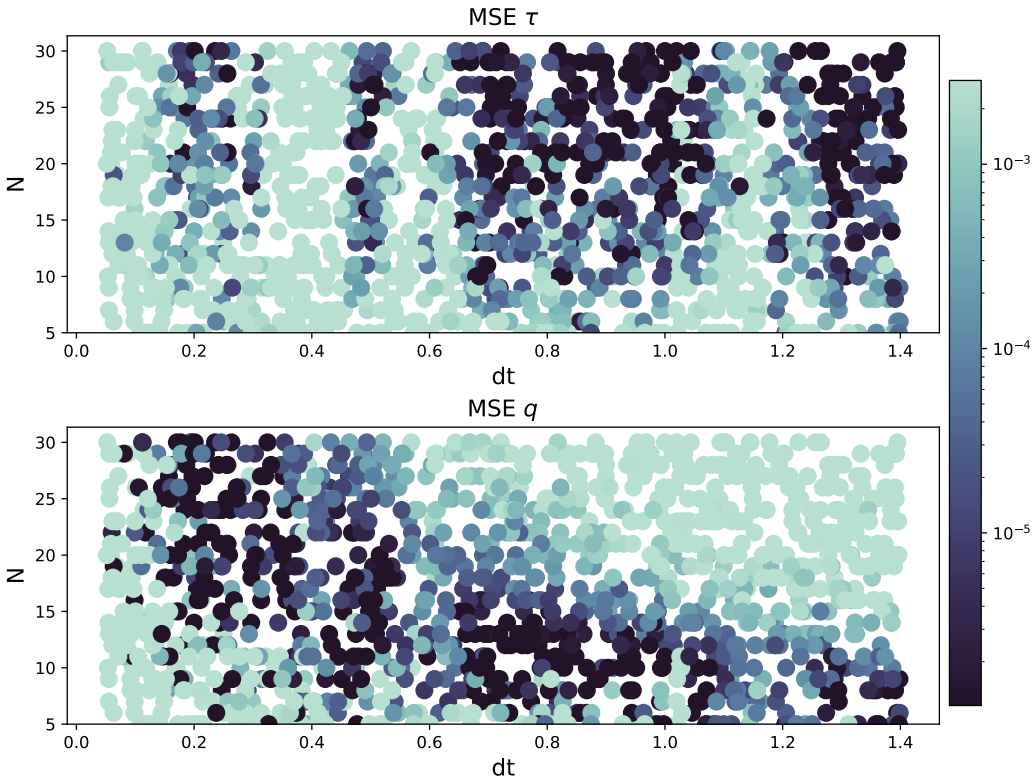

Figure B.1: The figure shows the same result as Fig. 5.14, but for randomly generated initial orientations. 1474 simulations.

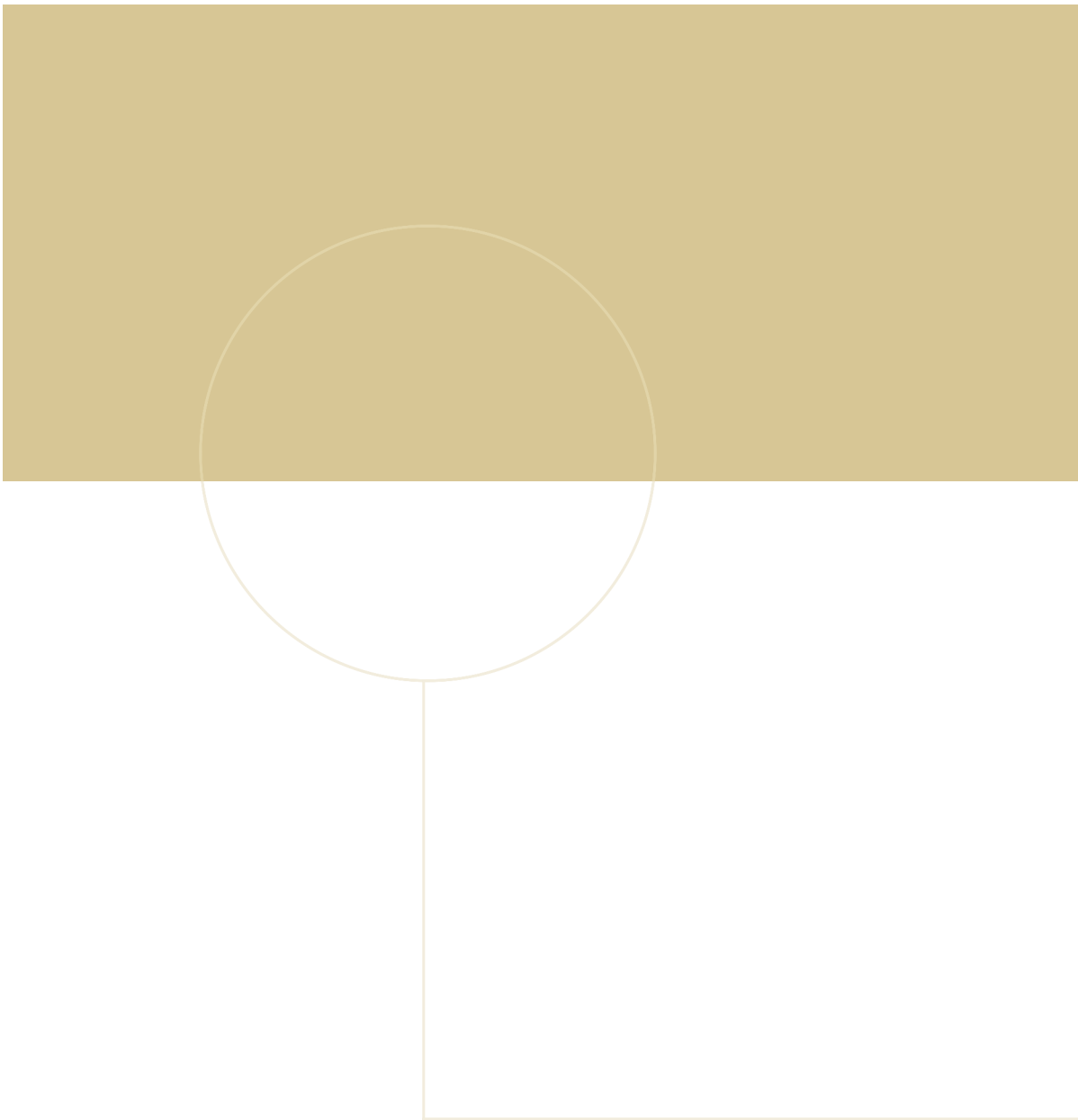

NTNU

Norwegian University of
Science and Technology